University College London

Computational Studies of Bio-Inspired FeS: Bulk, Surfaces and Clusters

Thesis submitted for the degree of Doctor of Philosophy (PhD) by

Saima G. Haider

Supervisor

Prof. Nora H. de Leeuw

Declaration

I, Saima Haider, confirm that the work presented in this thesis is my own. Where information has been derived from other sources, I confirm that this has been properly and fully acknowledged in the thesis.

Abstract

In this thesis we present the results of our simulation studies of iron sulphide minerals, with focus on bulk, surface and cluster chemistry.

DFT+U calculations were employed to study the mineral greigite (Fe_3S_4), which has important implications in Origin of Life theories. Using a combination of DFT and Monte Carlo methods, we were able to explore the probable cation distribution of Ni-doped greigite over the two available lattice sites (tetrahedral and octahedral) at varying concentrations, as well as calculate the enthalpy of mixing and thus deduce at what concentration of Ni this mineral would be most stable. Results showed that within the lattice, site occupation by Ni will be concentration-dependent, whilst violarite, $FeNi_2S_4$, is likely to be the most stable (Fe,Ni)S phase.

The (001), (011), and (111) surfaces of violarite, both naked and in the presence of water, were investigated next, using a combination of DFT-D2+U methods. The (001) was found to be the most stable surface, whilst the (011) the most reactive with respect to water. The adsorption and dissociation of water on the surfaces also revealed a synergistic effect, whereby the adsorption of one water has a conducive effect on the adsorption of the next.

CPMD simulations were then conducted on the following hydrated ions: Fe^{2+}, Fe^{3+} and S^{2-}, and on the following systems, Fe_xS_y (x,$y \leq 4$), to investigate the structural and dynamical properties in water. Calculation of the Gibbs free energies (ΔG_{aq}) revealed that the formation of Fe_xS_y clusters with x,$y \geq 2$ will not only be in competition with the formation of iron hydroxides, but is also temperature-dependent.

Contents

List of Tables

List of Figures

List of Publications

The work described in this thesis has been published in the following papers:

S. Haider, R. Grau-Crespo, A. J. Devey, N. H. de Leeuw, "Cation distribution and mixing thermodynamics in Fe/Ni thiospinels", *Geochimica et Cosmochimica Acta*, **88**, 275-282, 2012.

S. Haider, D. Di Tommaso, N. H. de Leeuw, "Density functional theory simulations of the structure, stability and dynamics of iron sulphide clusters in water", *Physical Chemistry Chemical Physics*, **15**, 4310-4319, 2013.

S. Haider, A. Roldan Martinez, N. H. de Leeuw, "Catalytic dissociation of water on the (001), (011) and (111) surfaces of violarite: A DFT-D2 study", accepted, *The Journal of Physical Chemistry C*.

Acknowledgements

I would like to begin by thanking my supervisor, Professor Nora de Leeuw, for her much appreciated support and guidance over the past few years. Special mention must also be given to Dr. Ricardo Grau-Crespo, Dr. Devis Di Tommaso, and Dr. Alberto Roldan Martinez, for their invaluable advice and encouragement, whenever it was solicited.

Gratitude also goes to the EPSRC for funding, and to my second supervisor, Professor Richard Catlow, for his support. Acknowledgement should also be given to the machines on which this work was undertaken, including the HECToR, HPCx, and Legion supercomputers, and the Huygens cluster.

I would like to thank both past and present members of Nora's group for helping to make my time here so enjoyable, with a quick mention to both Ben and Richard for helping to keep me sane throughout the past year.

A big thank you to my family; my parents, sisters (Uzma and Sana) and brother-in-law (Afzal) for always putting up with me; to my friends, without whom I don't think I would have made it this far (in no particular order: Simran, Kush, Flo, Sona, Rishni, Sara, Tina, Simrath and Ajith); and also to my husband, Mubeen, for giving me more joy than he probably realises. And to God, for all of the above.

Chapter 1

INTRODUCTION

1.1 Iron Sulphide Minerals

Iron is one of the most abundant elements and metals to be found on the Earth, constituting a major part of the Earth's crust and core. Nickel is not as commonly found as iron, yet, as an iron-nickel mixture, it is again believed to form a major component of the Earth's inner core [Stixrude et al., 1997]. Sulphur is one of the most prolific non-metal elements, often located in hot springs and volcanic regions [Leybourne et al., 2012], and plays an important role in many biochemical processes.

Both iron and nickel have a tendency to oxidise upon exposure to the atmosphere, therefore both are rarely found in their native form on the Earth's surface. However, whilst iron oxides are fairly ubiquitous and act as the primary ore and source [Mulvaney, 1987, Schwertmann, 1991], nickel is instead normally found in combination with other elements such as sulphur and iron, and it is these ore deposits that act as the primary source of nickel [Ramdohr, 1980, Richardson and Vaughan, 1989, Tenailleau et al., 2006, Vaughan and Tossell, 1981].

Metallic sulphides are an important group of ore minerals, their value being that of an important source of metals. Transition metal sulphides constitute an important class of compounds, not least because of their various applications in industry, which

include catalysis (such as in the production of "clean" fuels [Copret, 2013]) and corrosion protection [Rohrbach et al., 2003]. Iron sulphides (and iron-nickel sulphides) are of particular interest, as the ability of their cations to exist in a number of different oxidation states has enabled them to form a diverse group of minerals with a range of physical and chemical properties. Additionally, this variability in oxidation state has resulted in their implication in many biological systems, marine systems and "Origin of Life" theories. Table 1.1 gives some basic information regarding various (Fe,Ni)S minerals.

Table 1.1: Members of the (Fe,Ni)S family.

Material	Composition	Abundance
mackinawite	FeS	Widespread mineral found in low-temperature environments.
pyrite	FeS_2	The most abundant iron mineral on the Earth's surface.
pyrrhotite	$Fe_{1-x}S$	Most abundant iron sulphides in the Earth and Solar System; rare in marine systems.
greigite	Fe_3S_4	Fairly widespread mineral particularly associated with fresh water sediments.
pentlandite	$(FeNi)_9S_8$	Widespread, found in most igneous rock intrusions.
violarite	$FeNi_2S$	Widespread, normally found as a secondary mineral in association with pentlandite.
polydymite	Ni_3S_4	Uncommon mineral, found as a secondary mineral in association with pentlandite.

1.1.1 Role of Iron Sulphides in Enzymatic Systems

The acetyl-coenzyme-A (CoA) pathway is a ubiquitous present-day process, which involves the overall conversion of two molecules of carbon dioxide into an acetate group, with water as a by-product [Russell and Martin, 2004] (see Equation 1.1). The two main enzymes involved in the catalysis are carbon monoxide dehydrogenase (CODH) and acetyl-coenzyme A synthetase (ACS) [Ferry, 1995, Huber and Wachtershauser, 1997, Ragsdale, 2009, Russell and Martin, 2004, Volbeda and Fontecilla-

Camps, 2005], both of which contain (Fe,Ni)S centres. ACS and CODH are tightly associated, and often considered to act as a bifunctional enzyme, where the ACS/CODH enzyme is an $\alpha_2\beta_2$ tetramer [Darnault et al., 2003]. Each β unit contains a cubane-type [4Fe-4S] B-cluster, and a mixed [Ni-4Fe-5S] C-cluster (which is also the active site of the CODH enzyme). A single [4Fe-4S] D-cluster bridges the two β sub-units. The B- and D-clusters both provide an electron transfer pathway between the C-cluster and the molecular surface, as well as to the external redox proteins, such as ferredoxin [Darnault et al., 2003, Volbeda and Fontecilla-Camps, 2005]. Each α sub-unit contains a single metal A-cluster, which is the active site in ACS, and contains a catalytic [2Ni-4Fe-4S] centre.

$$4H_2 + 2CO_2 + \mathrm{HSCoA} \rightarrow CH_3COSCoA + 3H_2O \;\; \Delta G = -59\,\mathrm{kJ\,mol^{-1}} \qquad (1.1)$$

(Where HSCoA refers to coenzyme A on its own, and $CH_3COSCoA$ is the coenzyme with a bound acetyl group.)

The mechanism of conversion consists of a series of reducing steps (see schematic in Figure 1.1), the first of which is the reduction of one molecule of CO_2 to CO (carbon monoxide), using electrons sourced from H_2 at the C-cluster of the CODH enzyme [Dobbek et al., 2001, Russell and Martin, 2004]. This CO then diffuses through a hydrophobic tunnel [Darnault et al., 2003] to the A-cluster of the ACS enzyme, where it condenses with a methyl group (formed via reduction of a second CO_2 molecule and transported by a cobalt carrier protein), resulting in a metal-bound acetyl group [Darnault et al., 2003]. Energy is released upon hydrolysis to acetate and subsequent cleavage of the active thioester bond [Darnault et al., 2003, Huber and Wachtershauser, 1997, Russell and Martin, 2004], which is used to drive ATP (adenosine-5$'$-triphosphate, often referred to as the energy currency of living cells)

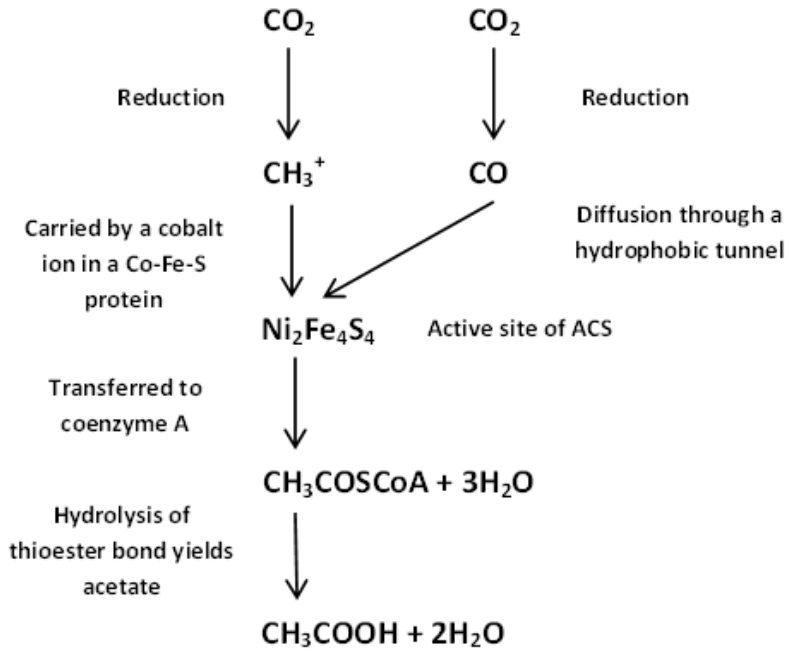

Figure 1.1: The acetyl-CoA pathway [Volbeda and Fontecilla-Camps, 2005].

synthesis and steer further metabolism essential to life, such as protein synthesis. As discussed, the crystal structure of the C-cluster in CODH contains a [Ni-4Fe-5S] cluster [Dobbek et al., 2001], where the Ni cation (responsible for much of the catalytic activity [Ferry, 1995]) is bound by four S atoms and completely integrated into the cluster, allowing for delocalisation of the electrons through the cluster upon reduction.

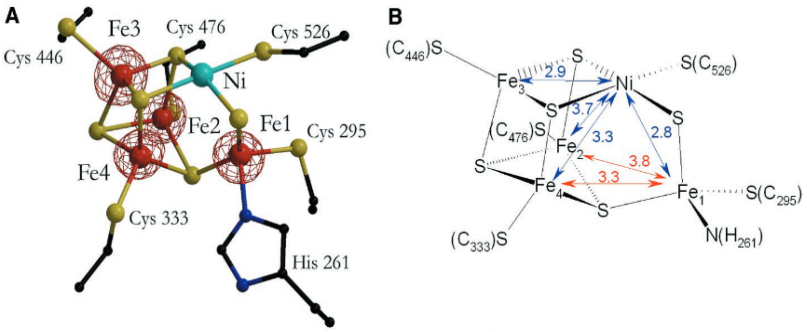

Figure 1.2: Active site (cluster C) of CODH [Dobbek et al., 2001], where (A) shows the protein ligands and (B) is a schematic representation.

This feature, whereby FeS clusters provide an electron transfer pathway to and from the active site, is also exhibited by NiFe hydrogenases [Volbeda and Fontecilla-Camps, 2003, 2005, Volbeda et al., 1995], which catalyse the reversible oxidation of molecular hydrogen into protons and electrons (see equation 1.2).

$$H_2 \leftrightarrow H^+H^- \leftrightarrow 2e^- + 2H^+ \tag{1.2}$$

All NiFe hydrogenases consist of at least two subunits, one containing the binuclear NiFe active site, which is then coupled to another subunit, composed of at least three FeS clusters, allowing for the transport of electrons and thus the oxidation of molecular hydrogen [Ragsdale, 2009, Volbeda and Fontecilla-Camps, 2005].

In addition to these three enzymes, Ni is also found in another, methyl-Coenzyme M reductase [Volbeda and Fontecilla-Camps, 2003]. The inclusion of Ni in all four is attributed to its flexibility in coordination and ability to transfer quickly between either of the oxidation states (I), (II) and (III) [Ragsdale, 2009].

1.1.2 (Fe,Ni) Sulphides and Hydrothermal Vents

Hydrothermal vents located on the Hadean ocean floor are suggested to have played an important role in the origin of life (see section 1.1.3). Some hydrothermal vents have been given the name "black smokers", due to the black appearance given to seawater from its precipitates [Luther et al., 2001]. Super-heated water emitted through these vents is both iron- and sulphur-rich, and upon mixing with the cooler seawater, lead to the deposition of minerals including iron sulphides. These vents also contain a variety of other elements, including Cu, Zn, Cl and Mg [Vondamm, 1990]. It was Elder [1965] who first proposed that such hydrothermal springs existed, as a result of volcanic and tectonic activity. Diving expeditions later verified their existence [Williams et al., 1974].

These vents are not only surrounded by, but support, vast communities of various micro-organisms [Takai et al., 2001]. Aside from the "black" colouring given to seawater, other vents have been shown to emit "milky-bluish" water, again, a sign of suspended particulate or colloidal sulphur, which in the form H_2S can provide energy (via oxidation) for bacterial chemosynthesis and enables the conversion of inorganic molecules into organic molecules, acting as a means of life-support for ecosystems that do not have direct access to natural sunlight [Jannasch and Wirsen, 1979]. That these vents create and support (via equilibration between the vent water and seawater) steep gradients of temperature, pH, oxidation-reduction potentials and various chemicals [Takai et al., 2001], helps to explain how different microhabitats for various microbial communities survive on the ocean floor.

A combination of these non-equilibrium conditions and since such vents contain a variety of elements and mineral compounds, also explains why this environment was deemed potentially conducive for those life-originating reactions.

1.1.3 Iron Sulphides and the Origin of Life

The origin of life would have necessitated the formation of carbon-carbon bonds under primordial conditions [Huber and Wachtershauser, 1997], whereby the available reagents would have included carbon dioxide, hydrogen, transition metals and sulphides. Thus, an autotrophic[1] origin would have seen the synthesis of organic primers via hydrogenation and carboxylation [Russell and Hall, 1997]. Such reactions would be akin to the aforementioned acetyl-coenzyme-A (CoA) pathway.

Surface Metabolism Theory was originally put forward as an explanation for the origin of life by Wächtershäuser [1988] in the late 1980s. His theory differed from previous explanations in that he suggested that the first organism was an autotroph, and that life emerged as a result of the interplay between chemical reactions derived

[1] Autotroph is a term given to an organism capable of synthesising its carbon constituents directly from carbon dioxide.

from reduced crustal/mantle fluids, and catalytic transition metal sulphides [Cody, 2004]. That the acetyl-CoA pathway is linear, exergonic, and does not necessitate any complex intermediates, in addition to these reactions being catalysed by proteins with FeS and (Fe,Ni)S centres, lends further support to the hypothesis that life originated at these hydrothermal vents [Russell and Hall, 1997]. Wächtershäuser stated that the autotrophic reactions implicated in primordial metabolism were confined to a two-dimensional mono-molecular organic layer, on which were located surface metabolists that were anionically bonded to the positively-charged surface. A net positive charge was essential as the products of metabolism contain organic nitrogen bases that are unable to form insoluble salts, eliminating possible binding to negatively-charged mineral surfaces. He further suggested that such organic constituents were likely to bind via their anionic carboxylate (-COO^-), thiocarboxylate (-COS^-) or thiolate (-S^-) groups [Wächtershäuser, 1990], ensuring the retention of the products. This then led him to stipulate that transition metal sulfides such as pyrite (FeS_2) would fit such necessary criteria.

Pyrite is one of the most abundant FeS minerals on the Earth's surface, and consequently is one of the most profiled iron sulfides in nature. It is also the most stable iron mineral under anaerobic conditions [Blöchl et al., 1992], and can act as a reducing agent through which Wächtershäuser postulated primordial metabolism was driven, allowing a linear flow of electrons from hydrogen sulphide to carbon dioxide [Wächtershäuser, 1992]. Pyrite is located wherever sulphur-dependent microorganisms are found [Stetter and Gaag, 1983], including in the chimneys of hydrothermal vents [Wächtershäuser, 1992]. Pyrite formation necessitates two main geochemical conditions [Wächtershäuser, 1992]: (i) contact between FeS deposits and aqueous H_2S, and (ii) quench of an equilibrium fluid containing Fe^{2+} and H_2S in hydrothermal vents. Sedimentary formation occurs via shallow burial, through the reaction between detrital iron minerals and H_2. This then produces a variety of metastable iron monosulphides which are converted to pyrite in early diagenesis.

Pyrite formation not only yields free electrons, (Equation 1.3), but is also exergonic (Equation 1.4), and as such its formation is suggested to act as a primordial source of energy [Wächtershäuser, 1990, 1992].

$$Fe^{2+} + 2H_2S \rightarrow FeS_2 + 4H^+ + 2e^- \tag{1.3}$$

$$FeS + H_2S(aq) \rightarrow FeS_2 + H_2 \quad \Delta G = -41.9\,\mathrm{kJ\,mol^{-1}} \tag{1.4}$$

A study by Drobner et al. [1990] showed that pyrite formation was possible under early geological conditions and did not require the presence of elemental sulphur. However, further investigation by Schoonen et al. [1999] demonstrated that while pyrite formation as a primordial energy source was thermodynamically viable, direct electron transfer from FeS to CO_2 was not, and therefore pyrite-mediated metabolism would not occur.

This shortcoming of the pyrite mineral theory then led to the expansion of the hypothesis into the Iron-Sulphur Membrane Theory [Russell and Hall, 1997], which suggests that life arose from a redox and pH front on the Hadean ocean floor, at the aforementioned hydrothermal vents. This would have been a favourable location, as it would have been far from the harmful oxdising ultraviolet radiation of the Sun [Cairns-Smith et al., 1992]. The Hadean ocean was also mildly acidic, due to a high partial pressure of atmospheric CO_2 [Macleod et al., 1994] and also contained a significant concentration of reduced iron as well as other transition metals. The hydrothermal fluid generated in the oceanic crust was in turn alkaline, and would have contained an abundance of H_2 and bisulphide (HS^-) [Macleod et al., 1994, Russell and Martin, 2004].

The interface between the alkaline hydrothermal front generated in the oceanic crust with the acidic oceanic fluid resulted in an alteration in the pH and temperature of the hydrothermal solution, which would have caused a spontaneous precipitation

of FeS and NiS membranes or "bubbles", formed via reaction of dissolved transition metals from the ocean, such as iron, with the bisulphide contained in the hydrothermal fluid [Russell and Martin, 2004]. These membranes are proposed to have possessed catalytic properties, acting as precursors to those FeS biological enzymes [Macleod et al., 1994], and are then proposed to have undergone a geochemical transformation to form greigite (Fe_3S_4) and violarite ($FeNi_2S_4$) [Cody, 2004]. It is thought that the reducing environment necessary for those life-originating reactions to occur would have been achieved via a switch in valency from ferrous (Fe^{2+}) to ferric (Fe^{3+}) of the mineral's cations, allowing for electron-donation to the reactants [Russell and Martin, 2004]. We can therefore see how such minerals are key to understanding how life may have originated.

This study is primarily concerned with greigite and violarite, and investigating them further in the context of their implication in many of the circulating Origin of Life theories. We have already outlined the importance of (Fe,Ni) sulphides in biological enzymes and in relation to the aforementioned theories. Chapter 2 explores the theory behind the techniques employed to model our systems, namely Density Functional Theory (DFT) and Molecular Dynamics (MD). In each of the results chapters, an overview is first given of the system of interest, which includes structural information, and also results of previous experimental and theoretical work, where appropriate. Chapter 3 deals with greigite, and discusses calculations that focus on the cation distribution and mixing thermodynamics of the Ni-doped mineral, using a combination of DFT and Monte Carlo methods. In Chapter 4 we move onto violarite, with the focus now shifted onto surface chemistry, and possible reaction pathways for the adsorption of water on its surfaces, again using DFT. Chapter 5 concentrates on MD simulations of the ions Fe^{2+}, Fe^{3+} and S^{2-}, as well as clusters of composition Fe_xS_y (x,y=1-4), in water. In addition, the free energies of formation/dissociation have been computed and are presented. Chapter 6 summarises our results from across the study,

and discusses possibilities for further investigation.

Chapter 2

THEORETICAL METHODS

We discuss here the theory behind the simulations and modelling of iron sulphides used in this study. Although different techniques have been employed throughout, all of the main codes utilised are based on *ab initio* electronic structure methods (e.g. density functional theory). Whilst such calculations are unable to deal with large systems (of more than $\sim$200 atoms), they are invaluable in providing information relating to the electronic structure of the system. Thus, as well as an overview of DFT, we also discuss it's implementation in molecular dynamics simulations, as well as examining the rationale involved in solvation modelling.

2.1 Density Functional Theory

2.1.1 Introduction and Background

It is known that electrons possess both wave- and particle-like characteristics, with the consequence that classical methods are incapable of describing them realisitically. Instead, we invoke the use of a wavefunction (Ψ), which contains information about the position ($\mathbf{r}$) and spin (σ) of the electrons, whilst the square of the wavefunction will give the probability of finding the electrons at a certain point. Quantum mechanical laws then state that the time-independent Schrödinger equation enables any given

property of a system to be calculated.

$$\hat{H}\Psi = E\Psi \tag{2.1}$$

Equation 2.1 is the time-independent Schrödinger equation, and describes the system's energy considering the particle-wave duality of the system. E represents the energy of the state, while $\hat{H}$ is the Hamiltonian operator that acts on the wavefunction Ψ, in such a manner that the result is proportional to E. The Hamiltonian can itself be expressed as a combination of different terms, for instance:

$$\hat{H} = \hat{T}_e + \hat{T}_n + \hat{U}_{ee} + \hat{U}_{nn} + \hat{U}_{en} \tag{2.2}$$

where T is the kinetic energy operator of the electrons (e) and the nuclei (n), and U is the potential energy operator of the electrons (ee), the nuclei (nn), and of both (en).

It therefore follows that it is only possible to solve Schrödinger's equation exactly for hydrogen atoms (or other one-electron systems), as for a system which has N electrons, the wavefunction will depend on $3N$ position coordinates, and N spin coordinates. Approximations are therefore enlisted to help simplify the problem.

The Born-Oppenheimer (BO) approximation is a key approximation, and allows the many-body wavefunction to be split into its electronic and nuclear components. The large difference in mass between the electrons and nuclei mean that it is viable to treat the nuclei as being stationary in relation to the moving electrons, and thus consider them to act as an external potential in which the electrons move. This enables us to rewrite the Hamiltonian operator as a combination of three terms:

$$\hat{H} = \hat{T} + \hat{U} + \hat{V} \tag{2.3}$$

where T now corresponds solely to the kinetic energy of the electron, U to the mutual interaction energy of the electrons, and V to the interaction energy between the electrons and the external potential field produced by the nuclei.

Once this approximation has been made, it is necessary to then solve the electronic Schrödinger equation. The electronic wavefunction depends parametrically on the position of the nuclei and not their momentum, therefore we solve the equation for fixed atomic positions. The differential of the energy (the force) is then used to propagate the nuclei to their new positions, where they are again fixed, and the electronic problem solved once more. This can be repeated until certain convergence thresholds are met.

Despite the BO approximation, solving the electronic equation is still a complicated task, due to the many-electron interactions within the system (known as the many-body electron problem) and thus the complexity of determining the complete N-electron wavefunction.

Density functional theory (DFT) provides a solution to this problem, and works by ignoring the N-electron wavefunction, and instead suggesting that the ground-state electronic energy can be determined from the electron density ($\rho(\mathbf{r})$). The origins of this theory go back to the 1920s, when Thomas [1927] and Fermi [1928] suggested that for larger systems, the number of electrons was so great, that the system could be treated statistically, and the electron density was thus the number of electrons per small volume element. Therefore, although DFT is know as an "exact" theory, approximations are still made within it. Fundamental to this are the two theorems by Hohenberg and Kohn [Hohenberg and Kohn, 1964], as well as the Kohn-Sham theory [Kohn and Sham, 1965].

2.1.1.1 The Hohenberg-Kohn Theorems

DFT is based on two theorems, postulated by Hohenberg and Kohn [Hohenberg and Kohn, 1964].

The first states that the ground-state electron density distribution $\rho(\mathbf{r})$ must determine a unique external potential $v(\mathbf{r})$ for that distribution, and hence must also determine the many-body wavefuntion $\Psi(\mathbf{r})$ (this is the same as saying that two external

potentials cannot give rise to the same electron density distribution). It therefore follows that that all the properties of a system can be calculated if the electron density is known.

The second theorem (also known as the variational principle), states that in order to find the ground state energy of a system for a given external potential, it is necessary to vary the electron density with respect to the energy of the system. Thus the electron density distribution which gives the minimum energy of the system, must be the electron density in the ground state.

Application of these two theorems enable us to calculate the ground state energy of a system for any given potential, and we can rewrite Schrödinger's equation as a function of the electron density:

$$[T[\rho(\mathbf{r})] + U_{ee}[\rho(\mathbf{r})] + V_{ext}[\rho(\mathbf{r})]]\Psi = E[\rho(\mathbf{r})]\Psi \tag{2.4}$$

where T is the total kinetic energy, U_{ee} is the functional describing the mutual interaction of the electrons, and V_{ext} is the Coulombic interaction between the electrons and nuclei.

2.1.1.2 The Kohn-Sham Theory

Fundamental to this theory [Kohn and Sham, 1965] is the assumption that we now consider the many-body electronic wavefunction to act as a fictitious one-particle, non-interacting wavefunction, which effectively converts all the interactions of all the electrons into one average interaction. We refer to these single particle wavefunctions as Kohn-Sham (KS) orbitals (ψ_i). The Kohn-Sham formalism splits the kinetic energy functional into two parts, one which can be calculated exactly, and the second consisting of a small correction term. The disadvantage of this is that orbitals are now reintroduced, and the complexity increases to N variables, and that the electron correlation reemerges as a separate term.

This theory begins with the postulation that the electron density can be written as a sum of one electron orbitals:

$$\rho(\mathbf{r}) = \sum_{i=1}^{N} |\psi_i|^2 \tag{2.5}$$

Within this system, the electrons are all assumed to be independent such that they do not interact, with the discrepancies between the interacting and non-interacting states being small. We therefore wish to find the set of orbitals which minimise the energy, and this gives rise to the Kohn-Sham equations:

$$\hat{H}_{KS}\psi_i = \varepsilon_i \psi_i \tag{2.6}$$

where $\hat{H}_{KS}$ is the Kohn-Sham Hamiltonian acting on each electron, such that:

$$\hat{H}_{KS} = -\frac{1}{2}\nabla_i^2 - \sum_{A=1} \frac{1}{\mathbf{r} - \mathbf{R}_A} + \frac{1}{2}\int \frac{\rho(\mathbf{r'})}{\mathbf{r} - \mathbf{r'}} d\mathbf{r} + V_{xc} \tag{2.7}$$

where the first term corresponds to the kinetic energy of the electron (∇_i^2 is the Laplacian operator which involves differentiation with respect to the coordinates of the i^{th} electron), the second term relates to the external potential felt by the electron as a result of the all the nuclei (A) in the system (where $\mathbf{r} - \mathbf{R}_A$ is the distance between the electron and the nuclei), the third term relates to the Coulombic interaction between that particular density with the rest of the electrons in the system, whilst the fourth term, V_{xc}, is the exchange-correlation potential experienced by each electron, which relates to the exchange-correlation energy of the system.

This final term is important, as the exchange-correlation energy accounts for the differences between interacting and non-interacting systems, and so all the electronic many-body interactions are conglomerated into this term. The general DFT expression can now be written thus:

$$E[\rho(\mathbf{r})] = T_s[\rho(\mathbf{r})] + V_{ne}[\rho(\mathbf{r})] + J[\rho(\mathbf{r})] + E_{xc}[\rho(\mathbf{r})] \tag{2.8}$$

where T_s is the total kinetic energy of the non-interacting system, V_{ne} is the interaction between the nuclei and electrons, $J[\rho(\mathbf{r})]$ is the Coulombic interaction between the nuclei and electrons and $E_{xc}[\rho(\mathbf{r})]$ is the exchange-correlation energy. It is possible to describe the first three terms without approximations. However, these must be made in order to describe the exchange-correlation.

2.1.2 Exchange-Correlation

Exchange-correlation essentially consists of: exchange, correlation, and a small correction to the kinetic energy. The E_{xc} can be thought of as the difference between the energy obtained from the best model and the exact energy obtained from the real, physical system, due to the exclusion of instantaneous interactions between electrons in the model. The exchange-correlation functional thus accounts for all the electron-electron interactions aside from the Coulombic ones.

The functional used should also account for a correction to the self-interaction phenomenon, which arises when an electron has a Coulombic interaction with itself (the density arising from an electron will interact with itself), so that even for a one electron system, the Coulombic repulsion will not be null, which can lead to artificial delocalisation in the system.

It is the choice between different exchange-correlation functionals that leads to differences between DFT methods. Below we outline two of the most commonly-used approaches for the construction of exchange-correlation functionals.

2.1.2.1 Local Density Approximation and Local Spin Density Approximation

In the local density approximation (LDA) [Parr and Yang, 1989] it is assumed that the exchange-correlation of a real system behaves locally as a uniform, homogeneous

electron gas of the same system. For instance, we use the exchange-correlation potential as it would be for a homogenous electron-gas at point **r**, so there are no spatial variations in the density. The E_{xc} can now take the form:

$$E_{xc}^{LDA}[\rho(\mathbf{r})] = \int \rho(\mathbf{r})\varepsilon_{xc}^{LDA}(\rho(\mathbf{r}))d\mathbf{r} \tag{2.9}$$

where $\varepsilon_{xc}^{LDA}(\rho) = \varepsilon_{xc}^{Hom}(\rho)$ and is thus the exchange-correlation energy per particle of a uniform electron gas, and $\rho(\mathbf{r})\varepsilon_{xc}^{LDA}(\rho(\mathbf{r}))$ will be the exchange-correlation per unit volume at position **r**. It follows that the electron density at that point is taken from a model of the exchange-correlation energy of a uniform gas of equivalent density and shows that the exchange-correlation is a function of the electron density at that point only, and not dependent on the density at other points in the vicinity. This means the LDA will be exact for uniform systems, and as it is a first-principles method, it does not contain any parameters that have been fitted empirically to experimental or calculated results.

In magnetic systems, where the spin densities ($\uparrow$, $\downarrow$) are not equal, it is possible to extend the LDA so that we now consider each group of electrons individually, which gives rise to the Local Spin Density Approximation (LSDA). In this we make use of the spin-interpolation formula devised by Vosko et al. [1980], which means the E_{xc} is now explicitly dependent on the two spin populations, and can be written in terms of total spin density and the total magnetisation/spin polarisation. So,

$$\text{Total spin density} = \rho\uparrow(\mathbf{r}) + \rho\downarrow(\mathbf{r}) = \rho(\mathbf{r}) \tag{2.10}$$

and

$$\text{Total spin polarisation} = \rho\uparrow(\mathbf{r}) - \rho\downarrow(\mathbf{r}) = \partial(\mathbf{r}) \tag{2.11}$$

which means we can now rewrite the E_{xc} as:

$$E_{xc}^{LSDA}[\rho(\mathbf{r}),\partial(\mathbf{r})] = \int \rho(\mathbf{r})\varepsilon_{xc}^{LDA}[\rho(\mathbf{r})]F[\partial(\mathbf{r})]d\mathbf{r} \tag{2.12}$$

so that the E_{xc} is now a function of the spin-polarisation as well. The spin-polarised correlation functional is obtained by interpolating the results for the homogenous electron gas at different spin densities.

Although the LSDA is an improvement upon the LDA, it still has its flaws. Firstly, it has a tendency to overestimate binding energies and strengths, leading to underestimated lattice parameters. It also underestimates elastic constants and phonon frequencies, and band gaps, causing problems by often predicting metallic behaviour for semiconductors. There are also problems from the electron self-interaction problem, which means core levels in atoms and d and f orbitals are poorly described, leading to poor description of strongly localised states. There is also the obvious problem that it is better at describing electron densities more homogeneous than the real one. The generalised gradient approximation (GGA) attempts to correct these failings.

2.1.2.2 Generalised Gradient Approximation

This method, unlike the LDA, accounts for inhomogeneties within the electron density, by including "local" gradients within it. It expands the dependency of the electron density at point $\mathbf{r}$ on the electron densities at different points within the vicinity, so it takes into account short-range forces.

$$E_{xc}^{GGA}[\rho(\mathbf{r})] = \int \rho(\mathbf{r})\varepsilon_{xc}^{LDA}[\rho(\mathbf{r})|\bigtriangledown\rho(\mathbf{r})]d\mathbf{r} \tag{2.13}$$

where $\bigtriangledown\rho(\mathbf{r})$ is the electron density gradient.

There are two main types of GGA ε_{xc}:

1. Parameter-free GGA functionals, which have been derived from first-principles, and are based upon the LDA. We use Perdew and Wang's PW91 functional, which is useful in the description of bulk materials [Perdew et al., 1992].

2. Hybrid GGA functionals, such as BLYP [Becke, 1988, Lee et al., 1988] and B3YLP, which are linear combinations of the DFT exchange-correlation with part of the Hartree-Fock exact exchange.

The GGA addresses many of the issues that arise from the use of the LDA, such as improved calculation of binding energies and bond strengths, which in turn means better estimated lattice parameters. This is also accompanied by a minor improvement in the replication of the band gaps of semiconductors and insulators (wider than the LDA, but still too narrow). However, the electron self-interaction problem still remains, which means there is still difficulty in describing strongly-correlated materials, where a large degree of electron localisation occurs. This is addressed by the incorporation of a further correction, the Hubbard correction.

2.1.3 Hubbard Correction (DFT+U)

In DFT, the exchange contribution is given by a density functional which does not cancel the Coulomb interaction of the electron with itself. Such functionals tend to favour delocalised systems and have a problem in describing strongly correlated systems where a large degree of localisation occurs (i.e. strongly-bound valence electrons). This leads to problems in describing strongly-localised d or f states. For instance, with respect to iron sulphides, this would lead to artificial hybridisation between the Fe d orbitals and the S p orbitals. The effective Hubbard correction (U_{eff}) parameter is a positive energy penalty applied to stop this and localise the d electrons, and thus more accurately describe the electron correlations relating to on-site Coulomb repulsions. For iron, the U_{eff} term acts to localise the d electrons to prevent smearing, so that electrons are associated with specific atoms. This approach is sometimes labelled the GGA+U method:

$$E_{GGA+U} = E_{GGA} + U_{eff} \sum \sigma \mathrm{Tr}[\rho^{\sigma} - \rho^{\sigma}\rho^{\sigma}] \tag{2.14}$$

$$U_{eff} = U - J \tag{2.15}$$

Where U is the Coulomb parameter, J the exchange, σ is the spin component and ρ is the on-site density matrix, and relates to the occupation of the d orbitals (if we have values of 1 or 0, relating to fully occupied or unoccupied respectively, then we do not have to apply the penalty as there is no hybridisation). Intermediate values correspond to partial occupancy or hybridisation, so we need to apply the positive energy penalty U_{eff}. Tr corresponds to the Trace, which is the sum of the diagonal elements in a matrix, to ensure that we only deal with one d orbital at a time (and not two d orbitals overlapping), and a separate penalty is applied for each d orbital that we are interested in.

Typically, it is extremely difficult to determine the U_{eff} from any first principles method, and it must instead be fitted to reproduce experimental data (such as lattice parameters), in a semi-empirical way. This is the procedure followed by Devey et al. [2009], who found that the Hubbard correction was needed to localise the Fe d electrons and correctly describe materials such as greigite. By calculating the lattice constant as a function of the U_{eff} parameter, they found a value of 1 would accurately describe greigite and its properties. This shall be discussed in more detail in Chapter 3 .

2.1.4 Dispersion Correction (DFT-D2)

One other shortcoming of density functionals such as the GGA is the inability to properly describe long-range correlation effects, including van der Waals, which may be occurring within the system. Such interactions arise as a result of the instantaneously-induced dipoles produced by fluctuations in the electron densities of the atoms and/or molecules contained in the system. There are a few dispersion corrections available for DFT, one of which is the Grimme method [Grimme, 2006], also known as

DFT-D2. Compared to other correction schemes, this method is less empirical and requires fewer fitting parameters. Grimme's dispersion-corrected DFT does not require the use of an entirely new functional, but instead makes use of the existing functional with the addition of an extra energy term, as in Equation 2.16. This energy term is a simple function of interatomic distances, and contains adjustable parameters that have been fitted to conformational and interaction energies. Due to the nature of the correction, the add-on term will not affect the wavefunction or any other molecular property, yet will lead to a change in geometry during optimisations, as the correction will affect the forces acting on the atoms. The use of such a correction can lead to a vast improvement in accuracy, with a minimal increase in computational cost.

$$E_{DFT-D2} = E_{KS-DFT} + E_{disp} \tag{2.16}$$

The long range interactions are described via a simple point-wise force field, which would have been optimised for several functionals. The dispersion energy for periodic systems is defined as:

$$E_{disp} = -S_6 \sum_{i=1}^{N_{at}-1} \sum_{j=i+1}^{N_{at}} \frac{C_6^{ij}}{R_6^{ij}} f_{damp}(R_{ij}) \tag{2.17}$$

where N_{at} is the number of atoms in the system, C_6^{ij} is the dispersion coefficient for the atom pair ij and is a semi-empirical parameter proportional to atomic polarizabilities and first ionization energies, S_6 is a global scaling factor that depends only on the functional used, and R_{ij} is the interatomic distance. For small values of R, a damping function f_{damp} must be used:

$$f_{damp}(R_{ij}) = \frac{1}{1 + e^{-d(R_{ij}/R_r - 1)}} \tag{2.18}$$

where R_r is the sum of the atomic vdW radii and d is a parameter that tunes the steepness of the dampening function. The role of the damping function is to minimise

contributions from interactions within typical bonding distances. The global scaling factor has itself been optimised for several DFT functionals.

2.1.5 Basis Sets

Basis sets are an inherent approximation in all *ab initio* calculations, and are necessary to solve the Kohn-Sham equations. Indeed, direct solution of the Kohn-Sham equations is not a practical proposition for molecules and solids. The most popular strategy is to create each molecular orbital as a linear combination of single electron orbitals:

$$\psi_i = \sum_{k=1}^{n} C_{ki}\phi_k \tag{2.19}$$

where ψ_i refers to the i^{th} orbital of the Kohn-Sham Hamiltonian, ϕ are the one electron orbitals that often correspond to the atomic orbitals and are commonly called basis functions, and C_{ki} are the coefficients for the linear combination. Because of the variational principle, the main objective is to determine the set of coefficients which give the lowest energy of the system:

$$\frac{\partial E}{\partial C_{ki}} = 0 \tag{2.20}$$

A complete basis set means that an infinite number of functions must be used, which is impossible. An unknown molecular orbital can be thought of as a function in the infinite coordinate system spanned by the complete basis set. The smaller the basis set, the poorer the representation. However, increasing the size of the basis set sees a corresponding increase in the computational cost, therefore the right balance must be found.

2.1.5.1 Localised Basis Sets

The basis sets most commonly used in quantum chemistry calculations are composed of atomic functions. The two most common types of basis functions used include Slater Type Orbitals (STOs) [Slater, 1930] and Gaussian type orbitals (GTOs) [Boys, 1950]. A STO for an *s*-type atomic orbital has the form:

$$N_s e^{-\xi r} \tag{2.21}$$

where r is the distance of the electron from the nucleus, N_s is the normalisation constant, and ξ is a constant known as the orbital exponent, which dictates the size of the orbital. STOs bear a great resemblance to the atomic orbitals of hydrogen, however, Slater functions are not particularly practical in molecular orbital calculations because of three- or four-centre integrals located on different nuclei, which are difficult to evaluate [Leach, 2001]. They are thus primarily used for atomic and diatomic systems which require high accuracy. They are also favoured in DFT methods which do not include exact exchange.

A Gaussian Type Orbital (GTO) for an *s*-type atomic orbital has the form:

$$N_g e^{-\xi r^2} \tag{2.22}$$

where this time the orbital is r^2 dependent. A consequence of this is that the product of two Gaussians will be another Gaussian, meaning that a two-electron integral can be reduced to that of a single Gaussian. This means GTOs offer a faster integral calculation speed.

The accuracy of the calculations is dependent on the number and type of functions used in the basis function. A minimal basis set will consist of a sum of Gaussian functions with fixed exponents and coefficients per atomic orbital. It is the addition of functions beyond the minimal basis set that allows for the description of non-spherical aspects of the electron distribution required for higher angular momenta.

For instance, to obtain higher orbital angular momentum basis functions, the basis GTO will be multiplied by the appropriate cartesian variables to produce p-type and d-type functions. A cartesian GTO will have the form:

$$N_g x^a y^b z^c e^{-\xi r} \tag{2.23}$$

where a, b and c correspond to the desired orbital type, so for a p_x-type orbital we would set a=1, b=c=0, whilst for a d_x-type orbital, we would set a=b=1, c=0.

The main problem that arises from the use of localised basis sets is the basis set superposition error (BSSE). If two interacting particles approach one another, then their basis sets will overlap, which leads to an increase in the number of basis sets describing the species. It will thus lead to an improved description of the orbitals and will therefore lead to an artificial lowering of the energy.

2.1.5.2 Periodic Systems and Plane Wave Basis Sets

A periodic system refers to those systems composed of a unit cell that can be repeated to form an infinite system, and the unit cell in three dimensions will be characterised by three vectors. The equivalent of a unit cell in reciprocal space is referred to as the first Brillouin zone (BZ). As a point in real space can be described using a vector $\mathbf{r}$, a vector in reciprocal space can be denoted using $\mathbf{k}$. The wave vector, $\mathbf{k}$, has units of inverse length and is closely related to the momentum and kinetic energy of a particle. Bloch's theorem states that the wavefunction value at equivalent positions in different unit cells are related by a complex phase factor. Thus the wavefunction for an electron in a periodic potential can be expressed by adding the multiplicative periodic function, $f_{\mathbf{k}}(\mathbf{r})$, where $f_{\mathbf{k}}(\mathbf{r}+\mathbf{T}) = f_{\mathbf{k}}(\mathbf{r})$, and $\mathbf{T}$ is the translational vector of the lattice (projects vector into the next lattice), such that :

$$\Psi_{\mathbf{k}}(\mathbf{r}) = f_{\mathbf{k}}(\mathbf{r}) \mathrm{e}^{\mathbf{i}\mathbf{k}\cdot\mathbf{r}} \tag{2.24}$$

And as the Blöchl function is periodic, we can further expand it into a 3D Fourier series:

$$f_{\mathbf{k}}(\mathbf{r}) = \sum_{\mathbf{G}} C_{\mathbf{k},\mathbf{G}} e^{i\mathbf{G}\cdot\mathbf{r}} \tag{2.25}$$

where **G** represents the reciprocal lattice vector, and *C* represents the coefficients of the wave vector and reciprocal lattice vector.

A consequence of Blöch's theorem is that the Kohn-Sham equations need to be solved everywhere in the Brillouin zone, therefore the internal energy of the crystal will be obtained by integrating the function over the first Brillouin zone, and an exact value of the integral would require integration over every possible point in the BZ. We instead replace the integral with a finite sum over discrete **k** points, which aims to reproduce the integral to a good approximation.

The Monkhorst-Pack algorithm [Monkhorst and Pack, 1976] is a way of sampling the Brillouin zone. It is an equally-spaced mesh which acts to compartmentalise the reciprocal space over which we perform the integration. The three indices give divisions in each direction (e.g. 4x4x4), and the larger the values of **k**, the smaller the compartments and thus the more accurate the reading.

Plane wave basis sets differ from other basis sets as they are aimed at modelling the full system directly, meaning they are completely delocalised and cannot be attributed to individual atoms. Through application of Bloch's theorem [Bloch, 1928], the basis function can be written as a product of a cell periodic part $f_{\mathrm{k}}(\mathbf{r})$ and a wavelike part $e^{i\mathbf{k}\cdot\mathbf{r}}$:

$$\phi_{\mathrm{k}}(\mathbf{r}) = e^{i\mathbf{k}\cdot\mathbf{r}} f_{\mathrm{k}}(\mathbf{r}) \tag{2.26}$$

And as the Bloch function is periodic, the cell periodic part can further be expanded as a set of plane waves, in accordance with Equation 2.25. The wavefunction

of an electron in a periodic field can then be expressed as a sum of plane waves:

$$\Psi_{\mathbf{k}}(\mathbf{r}) = \sum_{\mathbf{G}} C_{\mathbf{k}+\mathbf{G}} e^{i(\mathbf{k}+\mathbf{G})\cdot\mathbf{r}} \tag{2.27}$$

each of them with kinetic energy:

$$\frac{\hbar(\mathbf{k}+\mathbf{G})^2}{2m} \tag{2.28}$$

A wavefunction with index **k+G** is identical to one wavefunction with index **k**. Thus it is only necessary to find solutions for the values of **k** in one unit cell in the reciprocal space. In order to get a complete basis set, an infinite number of plane waves would be required to expand the wavefunction. However, as this is not possible, we introduce an energy cutoff, E_{cutoff}, that only includes planewaves with kinetic energies less than a stipulated value:

$$\frac{\hbar(\mathbf{k}+\mathbf{G})^2}{2m} < E_{cutoff} \tag{2.29}$$

The value of E_{cutoff} normally relates to the kinetic energy of the fastest electron in the system.

Plane wave basis functions are especially good at describing free electrons, and therefore good at describing metallic systems. VASP uses plane wave basis sets [Pickett, 1989] and implements fast-Fourier-Transform techniques to move between real and reciprocal space. However, a disadvantage of the plane wave approach lies in the uniform resolution. This means a large number of **G** vectors are required to accurately describe the ionic cores and electronic states. This problem is dealt with by utilisation of pseudopotentials.

2.1.6 Pseudopotentials

In order to describe the core electrons, we need to use a large number of basis functions to expand the orbitals, otherwise the valence electrons would not be properly described (due to poor representation of electron-electron repulsion). This is solved by assuming that the relevant properties of the system may be attributed to the valence electrons only, hence only these need to be treated explicitly, whilst the core electrons can instead be thought of as being "frozen", and treated by a suitable function, called the pseudopotential. The valence electrons can thus be thought of as moving in an effective potential produced by the ionic core, and the pseudopotential attempts to reproduce the interaction between the true atomic potential and the valence states.

Advantages to the introduction of pseudopotentials include fewer plane waves (as the core electrons have the highest kinetic energy, and so this cancels out the need for plane waves with very high kinetic energies) and fewer wavefunctions (as only valence wavefunctions need to be calculated). There is also improved precision, as the relative accuracy required to determine energy differences between configurations is much smaller, as the total energy of the valence-electron system is typically a thousand times smaller than the energy of the all-electron system.

There are different approaches within the pseudopotential methodology, such as the use of ultrasoft pseudopotentials [Vanderbilt, 1990]. The projector-augmented wave (PAW) method is also considered to be a pseudopotential method, although, in this instance, all of the core electrons are retained. These core electrons are frozen in their atomic reference levels and only the valence electron states are relaxed.

Thus, the Fe pseudopotential considers the [Ne] inner electrons of the Fe atoms, and the outer $3d^6$ and $4s^2$ are considered as valence electrons described using plane waves. The Ni pseudopotential considers the [Ne] inner electrons of the Ni atoms, and the outer $3d^8$ and $4s^2$ electrons are described using plane waves. The S pseudopotential describes the inner $1s^2$ $2s^2$ $2p^6$ electrons, leaving the outer $3s^2$ and $3p^4$

to be represented by plane waves as valence electrons.

2.1.7 Bader Charge Analysis

Bader et al. [1987] developed a useful method for dividing molecules into atoms, based solely on their electronic charge density. The electron density (in three dimensions) is divided into subsystems by zero-flux surfaces, with each subsystem normally containing only one nucleus. A zero-flux surface is a two-dimensional surface on which the charge density is a minimum perpendicular to the surface i.e. the gradient of the electron density has no component normal to the surface. In this way, the atomic volume is not fixed and is dependent only on the charge density, which varies with the oxidation state and environment.

2.2 Molecular Dynamics

Molecular dynamics is a computational technique which follows the time evolution of a set of interacting particles by integrating their equations of motion. In this simulation, the motion of the nuclei is modelled using the law of classical mechanics.

2.2.1 Equations of Motion

Let us consider the case of a particle moving under the influence of a force $\mathbf{F}(\mathbf{r})$:

$$m\frac{d^2\mathbf{r}}{dt^2} = \mathbf{F}(\mathbf{r}) \tag{2.30}$$

The classical equations of motion are:

$$\frac{d\mathbf{r}(t)}{dt} = \frac{\mathbf{p}(t)}{m} \tag{2.31}$$

$$\frac{d\mathbf{p}(t)}{dt} = \mathbf{F}(\mathbf{r}) \tag{2.32}$$

where $\mathbf{p}(t) = m\mathbf{v}(t)$ is the particle's momentum. The integration of equations 2.31 and 2.32 will define the trajectory of the particle subject to the external force-field $\mathbf{F}(\mathbf{r})$, by the value of the position $\mathbf{r}(t)$ and momentum $\mathbf{p}(t)$ at each time step, t. In the simple case of a constant force, $\mathbf{F}(\mathbf{r}) = F$, the time evolution of the particle's momentum and position will be given by:

$$\mathbf{p}(t) = Ft + \mathbf{p}_0 \tag{2.33}$$

$$\mathbf{r}(t) = \frac{1}{2}\frac{F}{m}t^2 + \frac{\mathbf{p}_0}{m}t + \mathbf{r}_0 \tag{2.34}$$

where $\mathbf{r}_0$ and $\mathbf{p}_0$ are the initial position and momentum of the particle, that will define the initial trajectory of the particle.

However, systems will often consist of more than one particle, all of which interact with one another. Therefore, in a set of N-interacting particles, the force acting on each particle will change whenever the particle changes position, or when one of the other particles that it is interacting with changes position: $\mathbf{F}_i = \mathbf{F}_i(\mathbf{r}_1,\mathbf{r}_2,...,\mathbf{r}_i,...,\mathbf{r}_N)$. We now have a set of N-coupled Newton's equations:

$$m_i \frac{d^2\mathbf{r}_i}{dt^2} = \mathbf{F}_i(\mathbf{r}_1, \mathbf{r}_2, ..., \mathbf{r}_i, ..., \mathbf{r}_N),\ i = 1, N \tag{2.35}$$

and the equations of motion for each individual particle become:

$$\frac{d\mathbf{r}_i}{dt} = \frac{\mathbf{p}_i}{m} \tag{2.36}$$

$$\frac{d\mathbf{p}_i}{dt} = \mathbf{F}_i \tag{2.37}$$

These new equations of motion are now too complicated to be solved analytically, and so these differential equations will be solved using a finite difference approach (such as the Verlet scheme described in Section 2.2.3). The general approach in MD simulations is to divide the simulation period into a series of very short time steps Δt (normally between 10^{-15} and 10^{-14} seconds), where at each step the forces on each atom are computed and combined with the current positions and velocities to generate new positions and velocities for the next time step. Within each time interval, the force acting on each atom is assumed to be constant. The atoms are then moved to their new positions, and the new forces for the next time step will now be computed, and so on. Using this method, the MD simulation generates a dynamical trajectory, which describes the dynamical variables ($\mathbf{r}_i$ and $\mathbf{p}_i$) of each particle in the simulation time period. MD is thus a technique that allows us to follow the microscopic dynamics of a system by following the trajectory of each particle in the system. It can therefore be thought of as a deterministic technique, where given the initial set of positions $\mathbf{r}_i(t_0)$ and momenta $\mathbf{p}_i(t_0)$, it is possible to completely define

the subsequent time evolution.

In a MD simulation, the N-interacting particles follow Newton's equations of motion, and thus the total energy of the system is conserved. This is an important property of the system, as it helps to establish a link between molecular dynamics and statistical mechanics.

2.2.2 Concepts of Statistical Mechanics

Statistical mechanics helps relate the macroscopic properties of a system to the microscopic details of the system, such as the distribution and motion of the atoms and molecules of the N-body system.

The thermodynamic state of a system is defined by a small set of parameters, such as the temperature T, the pressure P, and the number of particles N. The microscopic state of a system is defined by the atomic positions $\mathbf{r}_1$, $\mathbf{r}_2$,..., $\mathbf{r}_N$ and the momenta $\mathbf{p}_1$, $\mathbf{p}_2$,..., $\mathbf{p}_N$ of the N particles of the system.

Statistical mechanics is based on the Gibbs ensemble concept, whereby an ensemble is a collection of all the possible systems that have different microscopic states (for instance, different microscopic configurations which have an identical thermodynamic state). Thus, many individual microscopic configurations of a large system can lead to the same macroscopic properties. Different ensembles include:

- Microcanonical ensemble (NVE), which corresponds to an isolated system, and the thermodynamic state is characterised by a fixed number of atoms N, a fixed volume V and a fixed energy E.

- Canonical ensemble (NVT), whose thermodynamic state is characterised by a fixed number of atoms N, a fixed volume V and a fixed temperature T.

- Isothermal-isobaric ensemble (NPT), whose thermodynamic state is characterised by a fixed number of atoms N, a fixed pressure P and a fixed temperature T.

- Grand-canonical ensemble (μVT), whose thermodynamic state is characterised by a fixed chemical potential μ, a fixed volume V and a fixed temperature T.

If we now consider a system of N particles occupying a container of volume V and evolving under Newton's equations of motion, then the energy will be conserved during this time evolution, and in addition, the number of particles and volumes are assumed to be fixed. Therefore, a dynamical trajectory of a molecular dynamics simulation (i.e. the position and momenta of all particles over time) will generate a series of classical states having constant N, V and E, which corresponds to states of a microcanonical ensemble. This shows that MD is a statistical method. MD will normally be performed under conditions of constant number of particles, temperature and volume, but its trajectory can be modified to sample from other ensembles.

2.2.3 Integration Algorithms - The Verlet Algorithm

An integration algorithm is key to any molecular dynamics program, and is required to integrate the equations of motion of the interacting particles and follow their trajectory. The Verlet algorithm [Verlet, 1967] is probably the most widely used algorithm in MD calculations. The method involves writing two third-order Taylor expansions for the position $\mathbf{r}(t)$, one forward and one backward in time. Calling $\mathbf{v}$ velocities (the first derivative of the position), $\mathbf{a}$ the accelerations (second derivative of the position), and $\mathbf{b}_i$ the third derivative of the position with respect to time, the result is:

$$\mathbf{r}(t+\Delta t) = \mathbf{r}(t) + \mathbf{v}(t)\Delta t + \left(\frac{1}{2}\right)\mathbf{a}(t)\Delta(t)^2 + \left(\frac{1}{6}\right)\mathbf{b}(t)\Delta t^3 + O(\Delta t^4) \tag{2.38}$$

$$\mathbf{r}(t-\Delta t) = \mathbf{r}(t) - \mathbf{v}(t)\Delta t + \left(\frac{1}{2}\right)\mathbf{a}(t)\Delta(t)^2 - \left(\frac{1}{6}\right)\mathbf{b}(t)\Delta t^3 + O(\Delta t^4) \tag{2.39}$$

Adding these two equations gives:

$$\mathbf{r}(t+\Delta t) = 2\mathbf{r}(t) - \mathbf{r}(t-\Delta t) + \mathbf{a}(t)\Delta t^2 + O(\Delta t^4) \tag{2.40}$$

This is the basic form of the Verlet algorithm. Note that the velocities have been eliminated by addition. Although not required for the generation of trajectories, velocities can be useful for computing the kinetic energy, and thus the total energy E. It is possible to compute the velocities from the positions using:

$$\mathbf{v}(t) = \frac{\mathbf{r}(t+\Delta t) - \mathbf{r}(t-\Delta t)}{2\Delta t} \tag{2.41}$$

where the error associated with Equation 2.40 is of the order Δt^4. An improvement to the Verlet Algorithm is the Verlet Scheme, in which the positions, velocities and accelerations at time $(t+\Delta t)$ are computed from the same quantities at the time t. However, because in CPMD Δt must be very small as the dynamics are controlled by the small fictitious mass of the electrons, the Verlet algorithm has been chosen here.

2.2.4 Periodic Boundary Conditions

A common problem when simulating systems is that such systems will be of a finite size, and as such surrounded by "surfaces", meaning those atoms near the surfaces will have fewer neighbours than those inside the system. Although this may be ideal for cluster simulations, it is unrealistic for materials simulations, and would give a false ratio between the surface atoms and the total number of atoms, and would cause surface effects to be overestimated. The solution to this problem is to employ Periodic Boundary Conditions (PBC). This allows for unit cell replication in each of the three Cartesian directions, completely filling the space. Every particle in the simulation box thus has an exact duplicate of itself in each of the other cells. This means that whenever an atom leaves the simulation cell, it is replaced by another with exactly the same velocity, entering from the opposite cell face. This not only helps to

conserve the total number of atoms in the cell, but also removes any false surface effects experienced by the atom.

We now discuss the two main branches of MD: classical and *ab initio*, the latter of which is employed in this study.

2.2.5 Classical Molecular Dynamics

Classical molecular dynamics is based on the Born-Oppenheimer approximation, which, as explained in Section 2.1.1, assumes that the nuclei move in an effective potential due to the electrons V^e, in accordance with classical mechanics. The electronic potential should be computed by solving the electronic Schrodinger equation for each set of fixed nuclear coordinates $\mathbf{R}_I$, but in classical molecular dynamics, the effective potential is normally given in an approximate form, in terms of a truncated expansion of many-body contributions:

$$V^e \approx V^{approx.}(\mathbf{R}_\mathrm{I}) = \sum_I^N \upsilon_1(\mathbf{R}_\mathrm{I}) + \sum_I^N \sum_{J=I+1}^N \upsilon_2(\mathbf{R}_\mathrm{I},\mathbf{R}_\mathrm{J}) + \sum_I^N \sum_{J=I+1}^N \sum_{K=J+1}^N \upsilon_3(\mathbf{R}_\mathrm{I},\mathbf{R}_\mathrm{J},\mathbf{R}_\mathrm{K}) + ... \tag{2.42}$$

The electronic degrees of freedom are therefore replaced by interaction potentials υ_n, and are not featured as explicit degrees of freedom in the equation of motion. Therefore the mixed quantum/classical problem is reduced to pure classical mechanics, where two-body υ_2 and three-body υ_3 interactions are taken into account. This simplification means the effective potential from the electrons is now built from a manageable sum of additive few-body contributions. However, the penalty of using this is that the possibility of chemical transformation is now removed from classical MD simulations. Thus, in order to study processes involving bond transformations, such as hydrogen-transfer processes, *ab intio* molecular dynamics are needed instead.

2.2.6 *Ab intio* Molecular Dynamics

Ab initio molecular dynamics (AIMD) serves as a combination of classical molecular dynamics calculations and quantum mechanical electronic structure calculations. Rather than relying on empirical potentials, AIMD acts by combining electronic structure calculations with finite temperature dynamics. Although more computationally expensive, it is the natural choice in MD calculations when one wishes to study chemical bonding and electronic transformations.

There are two main implementations of AIMD that rely on the Born-Oppenheimer approximation [Marx and Hutter, 2000]:

- Born-Oppenheimer molecular dynamics (BOMD)
- Car-Parinello molecular dynamics (CPMD)

In this study, we used the latter to simulate FeS clusters in water. We thus briefly give an outline of BOMD first, before going into the theoretical approach of CPMD.

2.2.7 Born-Oppenheimer Molecular Dynamics

Born-Oppenheimer molecular dynamics (BOMD) is based on the Born-Oppenheimer approximation, where we solve the static electronic calculation for each molecular dynamics time step, with the nuclear positions fixed at each step. Therefore, the electronic structure part is reduced to solving a time-independent quantum problem, by solving the time-independent Schrödinger equation, and propagating the nuclei via classical molecular dynamics. The resulting BOMD equations of motion for the nuclear potentials are as such:

$$M_I \ddot{\mathbf{R}}_I(t) = -\nabla_I [E_0(\{\mathbf{R}_I\}) + V_{NN}(\{\mathbf{R}_I\})] \tag{2.43}$$

where $E_0(\{\mathbf{R}_I\})$ is the corresponding ground-state electronic energy at the nuclear configuration $\{\mathbf{R}_I\}$:

$$E_0(\{\mathbf{R}_I\}) = \langle\Psi_0|H_e(\mathbf{R}_I)|\Psi_0\rangle \tag{2.44}$$

and $V_{NN}(\{\mathbf{R}_I\})$ is the nuclear repulsion:

$$V_{NN} = \frac{1}{2}\sum_{IJ}\frac{Z_I Z_J e^2}{|\mathbf{R}_I - \mathbf{R}_J|} \tag{2.45}$$

For each set of nuclear configurations, $\{\mathbf{R}_I\}$, the time-independent Schrödinger equation must be solved in order to obtain the ground-state electronic wavefunction, Ψ_0, from which we can then compute the forces acting on the atoms:

$$\mathbf{F}_I = -\nabla_I\langle\Psi_0|H_e(\mathbf{R}_I)|\Psi_0\rangle + \mathbf{F}_{\text{ion}-\text{ion}} \tag{2.46}$$

where $\mathbf{F}_{\text{ion}-\text{ion}}$ is the force due to the direct nuclear-nuclear repulsion, whilst the first term can be calculated using the Hellmann-Feynman theorem [Feynman, 1939, Hellmann, 1937]:

$$\mathbf{F}_I^{HFT} = -\langle\Psi_0|\nabla_I H_e(\mathbf{R}_I)|\Psi_0\rangle \tag{2.47}$$

Use of this theorem means the need to calculate contributions from variations in the wavefunction with respect to atomic displacement can be avoided, meaning that we can instead compute the forces acting on the nuclei from the evaluation of Ψ_0 at only one nuclear configuration.

The forces acting on each atom are thus calculated, and the ionic positions updated via the Verlet algorithm, and this process is repeated until a sufficiently long MD trajectory is generated. The steps involved in the MD simulation are thus:

1. Relax the electronic configuration to its ground state for the present ionic configuration $\mathbf{R}_\mathrm{I}(t)$.

2. Calculate the forces on the atoms $\mathbf{F}_I$ using the Hellman-Feynman theorem.

3. Integrate the equations of motion for the ionic system $M_I\ddot{\mathbf{R}}_I(t)=\mathbf{F}_I$ to give the next set of ionic configurations $\mathbf{R}_I(t+\Delta t)$.

4. Repeat

There are two main problems with this procedure. The first is that the solution to Schrödinger's equation is not exact. Early applications of BOMD would rely on approximation schemes, such as semi-empirical and Hartree-Fock approximations to solve the electronic structure approximation. However, the breakthrough of DFT to solve Schrödinger's equation has helped to eradicate this problem. The second difficulty lies in the need to solve the electronic structure calculation for each electronic configuration during the simulation, which is a rather costly process, which CPMD aims to lessen.

2.2.8 Car-Parrinello Molecular Dynamics

Car-Parinello molecular dynamics (CPMD) [Car and Parrinello, 1985] is also based on the Born-Oppenheimer approximation. The electronic energy of the system E_0 can be evaluated for some wavefunction Ψ_0, which is also a functional of the nuclear positions, $\mathbf{R}_I$:

$$E_0 = \langle\Psi_0|H_e(\mathbf{R}_I)|\Psi_0\rangle = E_0(\mathbf{R}_I) \tag{2.48}$$

But at the same time, E_0 can also be considered as a functional of the wavefunction:

$$E_0 = E_0[\Psi_0(\mathbf{r})] \tag{2.49}$$

and in the framework of the Kohn-Sham density functional theory, E_0 can be written as a functional of the one-electron orbitals ψ_i used to build the wavefunction Ψ_0. We can therefore write the electronic energy of the system as a function of two components, quantum (electrons) and classical (nuclei):

$$E_0(t) = E_0(\psi_i(\mathbf{r}), \mathbf{R}_I(t)) \tag{2.50}$$

This represents a BO system. Car and Parinello regarded a system of electrons and nuclei that evolve according to the BO approximation as a two-component system, with two different energy scales. In this, the ions move at a pre-assigned temperature, while the electrons follow adiabatically, remaining in their instantaneous ground states, and are essentially at zero temperature. In the Car-Parinello method, the BO system is mapped onto a sytem whereby the nuclei and electrons are treated classically (i.e. they move according to Newton's equations of motion). To achieve this, the single-electron orbitals are imbued with a fictitious time dependence, $\psi_i(\mathbf{r}) \rightarrow \psi_i(\mathbf{r},t)$, and the orbitals are moved in accordance to the Newtonian equations of motion by defining a particular class of Lagrangians ($L = T - V$).

In the CP-method, the potential energy of the system at a certain time t is given by:

$$E_0(t) = E_0(\psi_i(\mathbf{r},t), \mathbf{R}_I(t)) \tag{2.51}$$

with the orbitals now dependent on time t.

The kinetic energy of the system is now the sum of two terms, one for the kinetic energy of the nuclei T_N, and the other for the kinetic energy of the electrons T_e,:

$$T_N = \frac{1}{2}\sum_I M_I \mathbf{R}_I^2 \tag{2.52}$$

$$T_e = \frac{1}{2}\mu \sum_i \int \dot{\psi}_i^*(\mathbf{r},t)\dot{\psi}_i(\mathbf{r},t)d\mathbf{r} \tag{2.53}$$

where μ is some fictitious mass ascribed to the orbital degrees of freedom. Car and Parinello defined the Lagrangian as:

$$L_{CP} = T_N + T_e - E_0 + \{constraints\} \tag{2.54}$$

where the $\{constraints\} = \int \psi_i^*(\mathbf{r},t)\psi_j(\mathbf{r},t)d\mathbf{r} = \delta_{ij}$

The Euler-Lagrange equations can now be applied:

$$\frac{d}{dt}\frac{\partial L}{\partial \dot{q}_j} = \frac{\partial L}{\partial q_j} \tag{2.55}$$

Considering the nuclear case, where the variables q_j equals a nuclear coordinate:

$$\frac{d}{dt}\frac{\partial L_{CP}}{\partial \dot{\mathbf{R}}_I} = \frac{\partial L}{\partial \mathbf{R}_I} \tag{2.56}$$

from which we obtain the equation which defines the classical equation of motion for the nuclei:

$$M_I\ddot{\mathbf{R}}_I(t) = \frac{-\partial E_0(t)}{\partial \mathbf{R}_I} \tag{2.57}$$

which defines the classical equation of motion for the nuclei.

For the electronic degrees of freedom, we have to substitute the simple derivative by the functional derivative, as our parameters are now functions in a continuous position space:

$$\frac{d}{dt}\frac{\delta L_{CP}}{\delta \psi_i^*(\mathbf{r},t)} = \frac{\delta L_{CP}}{\delta \psi_i^*(\mathbf{r},t)} \tag{2.58}$$

from which we obtain the Newtonian equation of motion for the electron orbitals:

$$\mu\ddot{\psi}(\mathbf{r},t) = \frac{-\delta E_0(t)}{\delta \psi_i^*(\mathbf{r},t)} + \frac{\delta}{\delta \psi_i^*(\mathbf{r},t)}\{constraints\} \tag{2.59}$$

As the CP method is usually implemented in the framework of the Kohn-Sham DFT, the force acting on the KS orbitals can be defined as:

$$\frac{\delta E_0^{KS}(t)}{\delta \psi_i^*(\mathbf{r},t)} = H_{eff}^{KS}(t)\psi_i(\mathbf{r},t) \tag{2.60}$$

where H_{eff}^{KS}(t) is the single particle Kohn-Sham operator (which now becomes time-dependent).

Hence, in CPMD the nuclei and orbitals evolve together i.e. the equations of motion for nuclear 2.57 and electronic 2.59 degrees of freedom are solved simultaneously using a standard time integration algorithm, such as the Verlet.

If we consider the expansion of the single-electron orbital in terms of a basis set:

$$\psi_i = \sum_k C_{ki}\phi_k(\mathbf{r}) \tag{2.61}$$

and introducing the time dependence of the orbitals $\psi_i(\mathbf{r}) \rightarrow \psi_i(\mathbf{r},t)$, we now have:

$$\psi_i(\mathbf{r},t) = \sum_k C_{ki}(t)\phi_k(\mathbf{r}) \tag{2.62}$$

The CPMD equations of motion are thus:

$$M_I\ddot{\mathbf{R}}_I(t) = \frac{-\partial E_0(t)}{\partial \mathbf{R}_I} \tag{2.63}$$

$$\mu\ddot{c}_{ki}(t) = \frac{-\partial E_0(t)}{\partial c_{ki}(t)} + \frac{\partial}{\partial c_{ki}(t)}\{constraints\} \tag{2.64}$$

In CPMD, the nuclei and orbitals are considered a part of an extended classical system, where the nuclei evolve in time at a certain physical temperature and a "fictitious temperature" associated with the electronic degrees of freedom. The use of the terms "low electronic temperature" or "cold electrons" means that the electronic subsystem is close to its instantaneous minimum energy. Thus, a ground state wavefunction optimised for the initial configuration of the nuclei will stay close to its ground state also during the time evolution if it is kept at a sufficiently low temperature. Hence, in CPMD calculations it is important to check that the time evolution of

the “fictitious temperature” of the electrons maintains a constant value close to zero.

2.3 Solvation Modelling

Molecules in solution experience interactions with the solvent molecules, and this will lead to changes in properties (e.g. geometry) when compared to the molecule in the gas phase. Therefore, it is necessary to be able to appropriately describe systems in the liquid phase, rather than just assume the properties will remain unchanged when going from the gas phase to the liquid. The interactions between the solvent and solute molecules tend to be very weak, assuming no covalent bonds form. There are two broad types of method for describing the solvent effect: the first evaluates the individual solvent molecules, and the second treats the solvent as a continuous medium. The first would involve building a finite system that should be sufficiently large enough to imitate the infinite system, but in practical terms, this could lead to a considerable computational cost due to the size of the system, especially if the whole system is described at the quantum mechanical level. An alternative approach is to assume that the solvent acts as a homogenous medium with a dielectric constant [Duben and Miertus, 1981], as in Continuum Solvation Models.

2.3.1 Continuum Solvation Models and the Polarisable Continuum Model

In Continuum Solvation Models, we treat the solvent as a uniform polarisable medium with a dielectric constant ε, and with the solute, M, placed in a suitably shaped hole in the medium [Cramer, 2004, Jensen, 2006, Roux and Simonson, 1999, Tomasi and Persico, 1994, Tomasi et al., 2005], as in Figure 2.1.

The hole in the medium will cause destabilisation and thus cost energy, whilst dispersion interactions between the solvent and solute adds stabilisation. The electric charge distribution of M will polarise the medium by inducing charge moments, and this in turn acts back on the molecule, producing an electrostatic stabilisation. However, there may also be repulsive elements to this interaction.

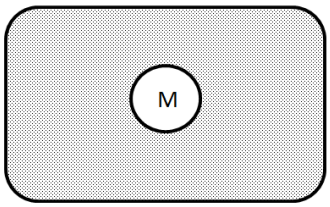

Figure 2.1: Continuum solvation model.

The dielectric constant is normally taken as having a constant value of ε, but can in some instances be taken to depend on the distance from the solute M. It can also be allowed to be frequency-dependent, so that the response of the solvent is different for a "fast" reaction (i.e. electronic transition), than for a "slow" reaction (i.e. molecular reorientation) [Mikkeslen and Sylvester-Hvid, 1996]. ε is the only parameter which defines the solvent.

There are five main ways in which models may differ [Jensen, 2006]:

1. How the size and shape of the hole are defined.
2. How the cavity/dispersion contribution is calculated.
3. How the charge distribution of the solute is represented.
4. How the solute is described, either classical (force field) or quantum (semi-empirical or *ab initio*).
5. How the dielectric medium is described.

In the Polarisable Continuum Model (PCM), the size and shape of the cavity must first be defined, followed by insertion of the solute into the cavity, and calculation of the solute's wavefunction via Hartree-Fock, post-HF or DFT methods, which is used to evaluate the electrostatic interactions between the solute and its polarised surroundings.

The construction of the cavity is an important step, and an ideal cavity is one which reproduces the shape of the solute and contains within it the entire solute

charge distribution, whilst excluding the solvent [Onsager, 1936]. If the cavity is too large, the solvation effects become muted, whilst if too small, errors will occur with regards to the interaction energy near the boundaries between the solute and solvent [Tomasi and Persico, 1994]. The shape of the cavity is equally important. The simplest shape for the hole is a spherical ellipsoid, which has the advantage that the electrostatic interaction between the solute and the dielectric medium can be calculated analytically. However, when simulating molecules, this model proves to be too simplistic. More realistic models use molecular-shaped holes, generated by interlocking spheres located on each nucleus [Tomasi and Persico, 1994, Tomasi et al., 2005]. In the original PCM paper [Miertus et al., 1981], the cavity was defined in terms of spheres with radii R_α, proportional to the van der Waals radius:

$$R_\alpha = f R_\alpha^{vdW} \tag{2.65}$$

1.2 is the normal value given for f, due to the consideration that the van der Waals radius should act as a lower limit for the cavity radius. The most popular set of atomic van der Waals radii is that of Bondi, obtained from crystallographic data [Bondi, 1964].

Once inside the cavity, the charge distribution polarises the dielectric continuum, which will in turn polarize the solute charge distribution. This interaction relates to a self-consistent procedure, which is necessary to solve the correlations between the polarisation of the dielectric continuum and the electron distribution of the solute. A consequence of the redistribution of the electrons is that the structure of the solute may change. In most calculations involving neutral molecules, the geometry of the solute in the solvent is kept fixed to the optimised gas phase geometry. However, when dealing with charged species, it becomes important to reoptimise the geometry within the PCM model [Di Tommaso and de Leeuw, 2009]. The basic definition of a PCM can be summed up in the following equation [Tomasi et al., 2005]:

$$\sigma(\bar{s}) = \frac{\varepsilon - 1}{4\pi\varepsilon} \frac{\partial}{\partial \overrightarrow{\mathbf{n}}} (V_{total})_{in} \tag{2.66}$$

where $\sigma(\bar{s})$ is the surface charge, ε is the relative permittivity of the dielectric continuum, $\frac{\partial}{\partial \overrightarrow{n}}$, is the gradient factor where $\overrightarrow{\mathbf{n}}$ indicates that the unit vector is perpendicular to the cavity surface and pointing outward, and V_{total} is the total electrostatic potential of the cavity, such that :

$$V_{total} = (V_M + V_\sigma) \tag{2.67}$$

where V_M is the electrostatic potential generated by the charge distribution and the solvent reaction potential, and V_σ is the electrostatic potential generated by the polarisation of the dielectric continuum.

Within *ab initio* calculations, there exist two types of PCMs: dielectric PCM (DPCM) and conductor-like PCM (CPCM). In DPCM the continuum is treated like a polarisable dielectric continuum, with a specific value of the dielectric constant ε. In CPCM, the continuum is treated like a conductor-like continuum with a dielectric constant equal to infinity, $\varepsilon = \infty$, which corresponds to the conductor, as for example in the COnductor-like Screening MOdel (COSMO).

2.3.2 COnductor-like Screening MOdel (COSMO)

The COnductor-like Screening MOdel (COSMO) [Klamt, 1995, Klamt and Schuurmann, 1993] has been used in this investigation to evaluate solvation free energies. Here, the molecule forms a cavity within the dielectric continuum, whilst the construction of the cavity differs in different COSMO implementations. The most common technique is to construct atom-centred spheres with radii $\sim$20% larger than the van der Waals radius. In COSMO, the dielectric constant of the continuum equals infinity, instead of a given value, by assuming the continuum is a conductor. Thus, the electrostatic potential will cancel out at the cavity surface, and if the distribution of the electric charge of the molecule is known (via quantum mechanical calculations),

it is possible to calculate the surface charge, using the value of the local electrostatic potential, rather than a component of its gradient as in Equation 2.66. To obtain the surface charge $\sigma(\bar{s})$, the ideal unscreened charge density $\sigma^*(\bar{s})$ which corresponds to $\varepsilon = \infty$ will be scaled by a function of ε [Tomasi et al., 2005]:

$$\sigma(\bar{s}) = f(\varepsilon)\sigma^*(\bar{s}) \tag{2.68}$$

And the scaling function $f(\varepsilon)$ is in turn empirically determined via comparison of COSMO (unscaled) energies with the correct electrostatic solvent-solute energies, and given by:

$$f(\varepsilon) = \frac{\varepsilon - 1}{\varepsilon + k} \tag{2.69}$$

Based on theoretical arguments outlining the dependency of k on the cavity shape and distribution of charges in the solute [Klamt and Schuurmann, 1993], a value of 0.5 for k was suggested. Since then, further studies have advised values of 0 [Barone and Cossi, 1998, Stefanovich and Truong, 1995, Truong and Stefanovich, 1995], whilst a study by Cossi et al. [2003] showed the value of k to be irrelevant for water, albeit important for other solvents, such as CCl_4. Therefore the energy of the solute-solvent interaction can be calculated via COSMO from knowledge of the solvent charge and the charge distribution of the molecule.

COSMO has the advantage over other methods in that it can be used for large and/or irregular molecules. It is also better used with solvents that have a higher permittivity, such as water ($\varepsilon \approx 80$), due to the theoretical assumption that we treat the solvent as a conductor in the model. It also negates the outlying charge error experienced with other dielectric methods, which is caused by small parts of the electron density of the solute appearing outside of the cavity in the solvent, via local corrections of the ideal screening charges, and of the corresponding solute potential [Baldridge and Klamt, 1997].

2.3.3 Calculation of the Free energy of Solvation using Polarisable Continuum Models

The free energy of solvation is arguably one of the most important methods of describing the interaction of a solute with a surrounding solvent [Cramer, 2004]. Ben-Naim [1974, 1978, 1987] described this solvation process as the transfer of a solute from a fixed position in the ideal gas phase to a fixed position in the solvent, at constant temperature, pressure, and chemical composition. There are various components to the solvation free energy (ΔG_{solv}), the most important of which include: the electrostatic interactions (ΔG_{el}), the cavitation energy (G_{cav}), and the van der Waals interactions (consisting of dispersion (G_{disp}) and repulsion effects (G_{rep})):

$$\Delta G_{solv} = \Delta G_{el} + G_{cav} + G_{disp} + G_{rep} \tag{2.70}$$

The electrostatic interactions are composed of Coulomb and polarisation terms, and we may obtain this term directly from *ab initio* calculations. It can merely be thought of as the difference between the *ab initio* energy of the isolated molecule in the BO approximation (G^0), with the analogous quantity computed in solution (G_{el}), such that $\Delta G_{el} = G_{el} - G^0$ [Tomasi et al., 2005]. However, when passing from the gas phase to solution, there will always be some change in internal geometry, and this also needs to be accounted for. Dipole moments in solution will always be larger than the corresponding dipoles in the gas phase, due to the effect of the solvent [Cramer, 2004].

The cavitation energy refers to the formation of the cavity within the solvent, and is a positive energy term which refers to the work spent in forming the cavity within the liquid, in the absence of solute-solvent interactions [Tomasi and Persico, 1994]. The process essentially consists of two steps, the first of which involves the formation of the cavity within the liquid, followed by insertion of the molecule into the cavity [Uhlig, 1937]. Once this is done, the other interactions are “switched on”, enabling

us to evaluate the other elements of the solvation free energy.

The dispersion and repulsion terms are sometimes conglomerated into one term known as the van der Waals contribution to the interaction energy, however, due to their different origins, actions and opposite signs, it is often deemed better to consider each separately. The dispersion merely refers to the favourable interactions between simultaneously-induced dipoles in adjacent molecules. Once a solute has been inserted into the cavity, it will experience favourable interactions with the solvent.

Chapter 3

GREIGITE: CATION DISTRIBUTION AND MIXING THERMODYNAMICS

In this chapter, a theoretical investigation into the partitioning of Ni over the tetrahedral and octahedral sites of greigite has been conducted. The thermodynamics of mixing in the $(Fe,Ni)_3S_4$ system is discussed in order to help understand why violarite ($FeNi_2S_4$) is the most common composition in the solid solution series between greigite and polydymite (Ni_3S_4), while low Ni/Fe ratios are much less abundant [Misra and Fleet, 1974]. The variation in cell parameter with composition is also discussed.

3.1 Introduction

Greigite was first discovered in lacustrine sediments by Skinner et al. [1964], where it formed as small grains and crystals dispersed throughout clays and fine silts that were blackish-grey in colour. It was deduced through studies that the formula of this mineral was Fe_3S_4, and as such it is an iron member of the thiospinel family. This family consists of materials with a unit cell consisting of eight AB_2S_4 units, where

A refers to cations in tetrahedral sites, and B to cations in octahedral sites. When divalent cations occupy the A sites, the structure is that of a normal spinel; if they occupy the B sites, we now have an inverse spinel. Whilst fairly stable in air, it was noted that the mineral was strongly magnetic in nature, and described as possessing similar magnetic properties as that of magnetite (Fe_3O_4). Formation in nature was said to occur via the reduction of iron solutions by the bacteria *Desulphovibrio desulphuricans* [Freke and Tate, 1961], but only under anaerobic conditions in H_2S-rich waters, such as those that would have been present on the Hadean ocean floor.

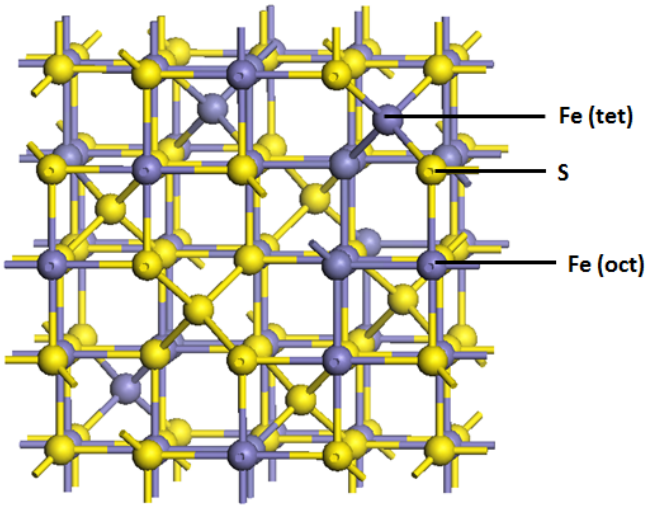

Figure 3.1: Greigite as seen along the c-axis; S in yellow, Fe in purple.

Interest in greigite as a potential catalyst in the Iron-Sulphur Membrane Theory has meant that studies into this mineral and other iron sulphides have become more numerous. Investigations into the Ni-doping of greigite would be particularly beneficial in further developing the chemical analogy between FeNi-sulphide enzymes and FeNi-sulphide minerals, as would a comparison between the coordination environment of the cations in the enzymes and the minerals.

In NiFe hydrogenases, a class of enzymes responsible for the conversion of molecular hydrogen into protons [Canaguier et al., 2008, Ragsdale, 2009, Russell and Hall, 1997, Volbeda and Fontecilla-Camps, 2003], the coordination of nickel in the active

site is always lower than that of iron. For instance, when the enzyme is in the oxidised state, Ni is in square-planar coordination, while Fe is square-pyramidal; in the reduced state, Ni exhibits a square-pyramidal coordination, and the Fe has an octahedral geometry [Canaguier et al., 2008, Volbeda and Fontecilla-Camps, 2005, Volbeda et al., 1995]. In carbon monoxide dehydrogenase (CODH), responsible for the catalysis of CO_2 to CO [Ragsdale, 2009, Russell and Martin, 2004], Ni is in a tetrahedrally distorted square-planar coordination, and the proximal Fe also displays tetrahedral geometry [Dobbek et al., 2001, Gencic et al., Svetlitchnyi et al., 2004]. This is also the case for the distal Ni in acetyl coenzyme-A synthetase (ACS) (the enzyme which acts to combine the resultant CO with a methyl group [Volbeda and Fontecilla-Camps, 2005]), where Ni exhibits a square-planar geometry [Lindahl, 2004]. From these observations, it would appear that the analogy between sulphide minerals and enzymes is closer when Ni is preferentially located in the tetrahedral sites of the greigite structure, and indeed, this agrees with the representation made of the Ni-doped greigite structure in the original paper on the Iron-Sulphur Membrane Theory by Russell and Martin [2004]. However, so far the coordination environment of Ni in greigite has not been investigated. Although the nickel-analogue of violarite is said to have an inverse spinel structure of the form $Fe^{3+}[Ni^{2+}Fe^{3+}]S_4$, there is no real experimental evidence for this (Hulliger [1968], see Section 3.1.4).

Further on in this chapter we shall discuss the calculations involved and the results from our theoretical investigation into the cation distribution in greigite, but we shall begin with a review of the mineral and its structure and properties, as reported in the literature.

3.1.1 Greigite: Structure and Properties

Greigite is a cubic ferrimagnetic semi-metal [Devey et al., 2009] belonging to the *Fd3m* space group with the cell parameter a = 9.876Å [Skinner et al., 1964]. Ferrimagnetism arises as a result of unequal opposing spin moments in the solid, which

leads to permanent magnetism; semi-metallicity infers that only one spin population (either up or down) has an appreciable density of states at the fermi level i.e. only one population of spin may pass freely from the valence to the conduction band, whilst the other population has a band gap between the two. Sixteen of the twenty-four irons in the greigite unit cell are trivalent Fe^{3+}, and the remaining eight divalent Fe^{2+} [Vaughan and Ridout, 1971]. As mentioned above, it is widely accepted as the sulphur analogue to magnetite (Fe_3O_4), where the sulphur anions S^{2-} are held together in a cubic close-packed lattice, while the iron ions occupy a mixture of tetrahedral (A) sites and octahedral (B) sites [Devey et al., 2009, Vaughan et al., 1971]. Mössbauer measurements by Vaughan and Ridout [1971] have revealed an inverse spinel structure, with the ions arranged as $(Fe_A^{3+})_8(Fe_B^{3+})_8(Fe_B^{2+})_8S_{32}^{2-}$. Yet the exact distribution of the cations over the B sites is still unknown, owing to the significantly covalent character of the iron sulphide bonds, making it difficult to discern multiplet structures in spectroscopy [Letard et al., 2005]. It is the presence of the Fe^{2+} cations in the lattice that accounts for the semi-conducting behaviour [Vaughan and Ridout, 1971], via electron-hopping between the ferrous and ferric sites [Spender et al., 1972].

3.1.2 Greigite: Synthesis and Formation

Yamaguchi and Katsurai [1960] were the first to synthesis a magnetic iron sulphide with a spinel structure, prior to greigite's actual discovery in nature. Shortly after, Uda [1965] proposed a modified method for the synthesis of greigite. This method involved the production of a black non-magnetic sulphide, prepared from mixing Mohr's salt ($(NH_4)_2Fe(SO_4)_2{\cdot}6H_2O$) with sodium sulphide. Once the precipitate had settled, the mixture was then subjected to autoclaving by immersion in an oil bath, proceeded by quenching the resultant material to obtain greigite.

It is possible to synthesise micro-rods of greigite, via an in-situ magnetic-field-assisted hydrothermal route [He et al., 2006]. In this process, ammonium iron sulphate hexahydrate and various sulphur precursors are dissolved in water. The resul-

tant solution is then placed in a vessel with circular magnets placed at the top and bottom, and placed inside a stainless steel autoclave. After twenty-four hours, black products are obtained. Various other methods are suggested for the synthesis of iron sulphide nano-sheets, including greigite [Han and Gao, 2008].

Conditions particularly indicative of the formation of greigite in nature, include an anaerobic sulphate-rich environment, and the presence of other partially non-magnetic iron sulphides, such as smythite ($(Fe,Ni)_9S_{11}$ [Taylor and Williams, 1972]), mackinawite and pyrite. There are said to be two main routes for the formation of greigite in sediments [Hoffmann, 1992]: One, which we have already mentioned, involves the production of iron-sulphides by sulphate-reducing bacteria under anaerobic conditions in H_2S-rich water, or freshwater sediments, in the presence of sufficient Fe ions. The second is via intracellular biomineralisation. This will occur in single or multicellular magnetotactic bacteria, common in brackish, sulphide-rich water and sediments.

Formation of greigite is also believed to occur from the mineral mackinawite ($Fe^{2+}S^{2-}$) [Lennie et al., 1995] or FeS_m [Berner, 1962], via oxidation of two-thirds of the Fe^{2+} cations in mackinawite to Fe^{3+} in greigite. These ions are now octahedrally coordinated within the lattice, and the phase transition is accompanied by a rearrangement about the sulphur sublattice, which results in a reduction in volume that leads to an increase in the stability of the structure [Rickard and Luther, 2007]. One process by which this is believed to occur is given in the equation below [Rickard and Luther, 2007]:

$$3FeS + S^0 = Fe_3S_4 \;\; \Delta G_r^0 = -13.7 \text{ kJ mol}^{-1} \tag{3.1}$$

This shows that greigite is stable with respect to mackinawite and sulphur, and in acidic conditions where S is stable, the transformation to greigite will occur readily. Consequently, greigite dominates in more acidic systems, and this fits with obser-

vations that it is more commonly found in freshwater conditions rather than marine environments.

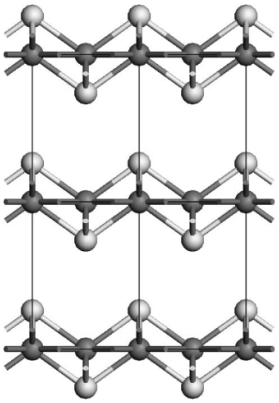

Figure 3.2: Devey et al. [2008]: Mackinawite, as seen along the *a*-axis; S in grey, Fe in black.

3.1.3 Bonding in Greigite and other (Fe,Ni) Sulphides

In iron sulphides, it is predominantly the metal 3*d* orbitals that occur at the top of the valence band and have the greatest effect on the properties of the mineral [Vaughan and Tossell, 1981]. Transition metals in B sites have σ_B bonding orbitals and $\sigma_B{}^*$ antibonding molecular orbitals, formed by overlap of the metal e_g, 4*s* and 4*p* orbitals with the 3*s* and 3*p* orbitals of the sulphur ions (see Figure 3.3) [Vaughan and Craig, 1978, Vaughan and Ridout, 1971]. The filled t_{2g} orbitals remain essentially nonbonding. For cations in A sites, it is the *e* orbitals that remain nonbonding, while the t_2, 4*s* and 4*p* orbitals now form σ_A bonding molecular orbitals and $\sigma_A{}^*$ antibonding orbitals with the sulphur 3*s* and 3*p* orbitals.

Both σ_B and σ_A bonding orbitals contribute to the valence band, while σ_B^* and σ_A^* contribute to the conduction band. Because *d*-electrons are inefficient at effectively screening nuclear charge, 3*d* electrons will become more stable and the cations less ionic as we go across the transition metal row in the periodic table, meaning that nickel will be more stable but less cationic than iron [Vaughan and Ridout, 1971].

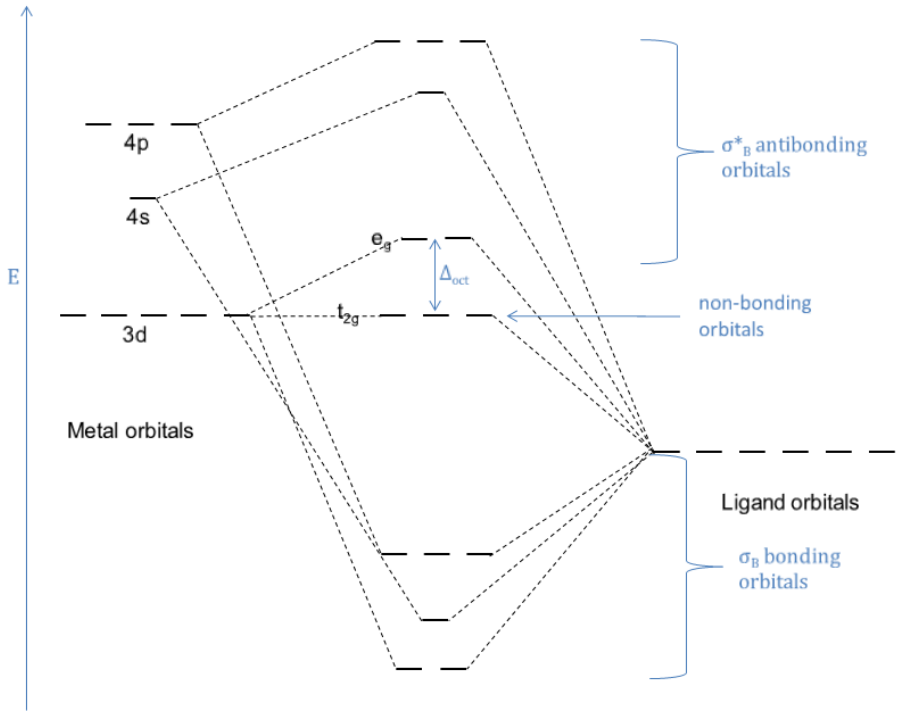

Figure 3.3: Combination of the metal atomic orbitals with the ligand atomic orbitals to form new molecular orbitals.

Solid solutions exist within the thisopinel family, usually involving two different cations [Vaughan and Craig, 1985]. Violarite ($FeNi_2S_4$) is a member of the range of solid solutions that has as its end-members greigite (Fe_3S_4) and polydymite (Ni_3S_4) [Hui et al., 2004, Vaughan and Craig, 1985]. Although part of the same series, we can see how differing occupation of the bonding and antibonding orbitals can lead to a difference in properties within this particular set of thiospinels.

The ferrous ions in greigite appear in high-spin states compared to low-spin states in violarite [Vaughan and Ridout, 1971], i.e., in greigite, the 3*d* electrons have unpaired spins that are uncoupled at lower temperatures [Vaughan and Craig, 1985]. As such, there is a higher number of electrons in the anti-bonding σ^* orbitals (7 electrons per formula unit for greigite, compared to 6 in polydymite and just 4 in violarite [Vaughan and Craig, 1978], Figure 3.4) resulting in a lower thermal stability of greigite, but also giving rise to a larger cell parameter, due to the fact that σ^* orbitals are

closer to the sulphur ligands and act to repel them. For instance, a in greigite is 9.876 Å, while in violarite a = 9.465 Å and in polydymite a = 9.489 Å [Craig, 1971]. This difference in spin states also helps to explain why, although the compositional range Ni_3S_4-Fe_3S_4 is observable in nature, bonding models suggest that the range $FeNi_2S_4$-Fe_3S_4 is metastable [Vaughan and Craig, 1985] and therefore experimentally limited and difficult to replicate. Interestingly, violarite may be stable up to temperatures as high as 461 °C, while the solid solution between polydymite and violarite still exists at temperatures of around 356 °C [Vaughan and Craig, 1985]. Yet the nickel analogue of violarite (also known as nickel-doped greigite), $NiFe_2S_4$, also possesses semiconducting and ferrimagnetic properties [Hulliger, 1968], and is suggested to have an inverse spinel structure, $Fe^{3+}[Ni^{2+}Fe^{3+}]S_4$, since Ni^{2+} has a strong preference for octahedral sites. The occurrence of $NiFe_2S_4$ supports the existence of a solid solution along the Fe_3S_4-$NiFe_2S_4$ series.

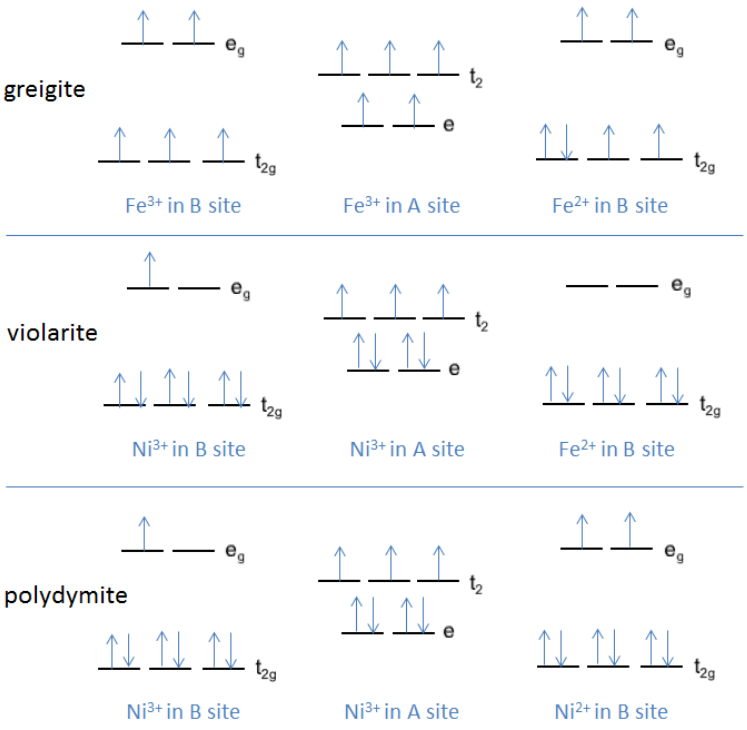

Figure 3.4: Occupation of the metal 3*d* orbitals in greigite, violarite and polydymite. The e_g and t_2 orbitals contribute to the σ^* antibonding molecular orbitals.

3.1.4 Experimental Studies

Greigite is one of the lesser explored minerals due to the difficulty associated with its synthesis. Mössbauer experiments have proved to be extremely useful when elucidating the structure of iron sulphide minerals such as greigite. Studies by Vaughan and Ridout [1971] were key in understanding that greigite possessed an inverse spinel structure, and the spectra they obtained were interpreted as three different sets of magnetic hyperfine spectra, which referred to the iron in the three different crystallographic sites. They were able to deduce from the isomer shifts, quadrupole splittings and hyperfine fields that high-spin ferrous and ferric ions would be located in the octahedral sites, whilst ferric ions would be found in the tetrahedral sites, lending itself to the formula $Fe^{3+}(Fe^{2+},Fe^{3+})S_4^{2-}$. They showed that the Fe cations in greigite exist in a high-spin state, meaning that there will be a significant number of electrons in anti-bonding orbitals, which would in turn lead to a larger cell parameter and lower thermal stability compared to other thiospinels such as violarite. It was also said that the semi-conducting and ferrimagnetic properties were indicative of the $3d$ electrons being more localised on the cations in greigite than in other thiospinels in the Cu-Co-Ni-Fe-S system. This could also explain why it is difficult to synthesise a complete solid solution between violarite and greigite, due to the difference in spin states. It is known that low-spin Fe^{2+} with half- or completely-filled t_{2g} orbitals are particularly stable in octahedral coordination, and thus have large octahedral-site preference energies. High-spin Fe^{3+} with half- or completely-filled $3d$ orbitals are stabilised relative to low-spin configurations in accordance with Hund's interatomic exchange energies. The isomer shifts obtained from Mössbauer experiments were attributed to high-spin Fe^{2+} in B sites.

Conductivity measurements performed by Spender et al. [1972] demonstrated that the presence of delocalised charge carriers in the compound can be attributed to electron-hopping between the ferrous and ferric sites, accounting for greigite's semiconducting activity.

Magnetite, of which greigite is an analogue, undergoes a Verwey transition whereby at T=121 K, the high-temperature spinel structure ($Fd3m$) lowers it symmetry to monoclinic Cc, and transforms from a metal to an insulator, accompanied by a drop in resistivity by two orders of magnitude [Pinto and Elliott, 2006, Verwey and Haayman, 1941]. Therefore, it was presumed that greigite might also undergo a similar transition. Dekkers et al. [2000] decided to investigate such magnetic behaviour of greigite within the temperature range 4 K - 700 °C . Upon heating in air, it was discovered that the products and magnetic behaviour were highly dependent on the amount of oxygen in the air. X-ray diffraction results showed that the first major product upon heating greigite above room temperature was pyrite (FeS_2), which itself would be converted to pyrrhotite ($Fe_{1-x}S$) and sulphur as a result of further heating to $550-600\,^{\circ}C$ in inert atmospheres. Heating greigite at temperatures above 400 °C would result in the production of magnetite and maghemite (Fe_2O_3, γ-Fe_2O_3), whilst haematite (Fe_2O_3) is the main product at 700 °C. They also showed that cooling to 4 K would not result in a Verwey-type transition in greigite, as previously shown by Spender et al. [1972].

Letard et al. [2005] performed high-resolution electron energy loss spectroscopy (EELS) experiments. X-ray absorption spectra were recorded on synthetic greigite samples a few weeks after synthesis, and then again six months later. They observed that greigite ages and transforms over time into an iron oxide similar in composition to haematite, α-Fe_2O_3, which contains only Fe^{3+} in octahedral sites. Their EELS on natural greigite samples showed a core-shell structure composed of a core of well-crystallised Fe_3S_4, and a shell of amorphous iron oxide, a possible precursor of haematite α-Fe_2O_3.

The transformation of mackinawite into greigite has also been studied, and shown to occur at temperatures above 373 K [Lennie et al., 1997]. Transmission electron microscopy (TEM) results revealed that during this transformation, the ccp sulphur sublattice is maintained, and that it is the oxidation of the ferrous ions to ferric ions in mackinawite that propels the formation of this new phase, via rearrangement of the

iron cations. This led the investigators to postulate that as mackinawite oxidises easily to form greigite, the transformation to pyrite should also be feasible, and if so, it would likely occur via the incorporation of more sulphur into greigite, and the reduction of the ferric ions to ferrous ions in pyrite. However, Rickard and Luther [2007] argued that while all three minerals have anionic cubic close-packing, in mackinawite and greigite there exists a simple array of ions, while in pyrite the anion ccp is only conceptual, the result of rationalising the average centre points of the sulphur anions. The implication of this is that while the transformation of mackinawite to greigite is relatively easy, achieved via rearrangement of Fe atoms in the ccp sulphur sublattice, conversion to pyrite would necessitate rearrangement of the sulphur sublattice itself.

Berner [1962] measured the solubility of greigite, which had been synthesised by bubbling H_2S through an aerated $FeSO_4$ solution at $80-90\,^{\circ}C$ for around 45 minutes. The solubility was then calculated for the reaction:

$$Fe_3S_4 = 3Fe^{2+} + 3S^{2-} + S^0 \tag{3.2}$$

where S^0 is rhombic sulphur, with which Berner assumed the system to be in equilibrium. From this he calculated the free energy of formation of greigite to be -290.4 kJ mol^{-1}. Rickard and Luther [2007] then recalculated this value, but according to the equation:

$$Fe_3S_4 + 3H^+ = 3Fe^{2+} + 3HS^- + S^0 \tag{3.3}$$

to avoid uncertainty in pK values for H_2S, and obtained a value of -308 kJ mol^{-1} for the reverse reaction, suggesting that greigite is even more stable than originally expected.

There has been much doubt regarding the Curie temperature (T_c) of greigite, with reported values of T_c often falling within the range of 600-800 K. Spender et al. [1972] estimated it to be around 606 K by extrapolation of thermomagnetic curves at high

temperatures. Vandenberghe et al. [1991] performed Mössbauer spectroscopic measurements up to 480 K and extrapolated the effective field of iron in tetrahedral sites to suggest the T_c had a value of at least 800 K. Magnetic measurements performed by Chang et al. [2008] on high-quality pure greigite samples suggested a temperature higher than 630 K. More recently, Wang et al. [2011] performed high-temperature magnetic measurements on hydrothermally-synthesised greigite, and showed that the T_c is around 677 K, much lower than the value for magnetite.

The nickel-analogue of violarite is said to possess semiconducting and ferrimagnetic properties [Hulliger, 1968], and is also predicted to have an inverse spinel of the form $Fe^{3+}[Ni^{2+}Fe^{3+}]S_4$, as Ni^{2+} has a high octahedral site preference. A solid solution is therefore predicted along the Fe_3S_4-$NiFe_2S_4$ series.

Vaughan and Craig [1985] also said that the unit cell parameter would increase from $FeNi_2S_4$-Ni_3S_4, and that greigite would have a larger cell parameter than the two, but the effect of Ni substitution in it would be unknown. They also determined the composition of a range of natural (Fe,Ni)S compounds using electron microprobe analysis, and found that while synthetic compounds do not form compositions more iron-rich than $FeNi_2S_4$, natural samples will show a complete compositional range from Ni_3S_4 to Fe_3S_4.

3.1.5 Theoretical Studies

DFT calculations have previously been conducted to investigate the effect of the Hubbard U_{eff} parameter when modelling greigite [Devey et al., 2009], which was found to be necessary to accurately describe the unit cell structure and magnetic moment. No U_{eff} would mean that the lattice parameter and magnetic moment would be underestimated, as well as giving an incorrect description of the electronic arrangement. This is due to one of the failings of the GGA methodology, whereby the electron correlation associated with Fe atoms is neglected. At U_{eff} = 0, Devey found that a ferrimagnetic spinel was obtained, whilst for higher values, the correct inverse spinel

structure was reproduced. Low values of U_{eff} ($0 < U_{eff} < 4$ eV) correctly predict an electronic structure which corresponds to that of a semi-metal, with semimetallicity arising from electron-hopping between ferric and ferrous cations in the octahedral sites. It was thus shown that an accurate description of greigite and all its properties could be achieved with U_{eff} = 1 eV. More recently, Wang et al. [2011] have also confirmed that the use of a low value (1.166 eV) for U_{eff} value enables the lattice constant and relative spin orientations on the different lattice sites to be predicted correctly in accordance with measured experimental values.

Gibbs et al. [2007] suggested that the Fe in A sites was tetravalent (Fe^{4+}) rather than trivalent, from calculating the theoretical electron density distributions, due to the shorter Fe-S bond lengths. This is something that had previously been considered by Hoggins and Steinfink [1976], however it is known that Fe^{4+} is extremely unstable in this state, and thus unlikely to exist in this form. Further comparison with other Mössbauer experiments on minerals such as Ba_3FeS_5 show the Fe to be trivalent. As such, there is no conclusive evidence to support this suggestion.

McCammon et al. [1992] compared greigite with the mineral cubanite ($CuFe_2S_3$), and this also led to the suggestion that the valences of the Fe atoms in B sites are down to the rapid transfer of electrons between the ferrous and ferric ions in the octahedral site, implying delocalisation of the electrons in the B sites.

3.2 Computational Techniques

3.2.1 Geometry Optimisations, Cell Relaxations and Single Point Calculations (DFT)

Density functional theory (DFT) calculations were employed to obtain the energies and equilibrium geometries of the (Fe,Ni) thiospinels, using the Vienna *ab initio* simulation package (VASP) [Kresse and Furthmuller, 1996, Kresse and Hafner, 1993,

1994], which uses spin-polarised density functional theory in the plane wave formulation. This approach has already been used successfully in the modelling of a number of iron sulphide minerals (e.g. Devey and de Leeuw [2010], Devey et al. [2008, 2009], Rohrbach et al. [2003]). All calculations are performed within the generalised gradient approximation (GGA), with the exchange-correlation functional developed by Perdew et al. [1992], and the spin interpolation formula of Vosko et al. [1980]. Following the previous work by Devey et al. [2009], a Hubbard correction with U_{eff} = 1 eV was applied to the Fe d orbitals to improve the description of the electron localization and to accurately replicate the experimental structure.

The valence orbitals are calculated as linear combinations of plane waves, and the size of the basis set is determined by a cutoff energy (400 eV in our case). The core levels are kept "frozen" during the calculations, which in this instance consist of orbitals up to, and including $3p$ for Fe and Ni, and $2p$ for S. The interaction between the valence electrons and core orbitals are described using the projector augmented wave (PAW) method [Blöchl, 1994] in the implementation of Kresse and Joubert [1999]. All calculations were performed in a cell with composition $Fe_{24-N}Ni_NS_{32}$. A Monkhorst-Pack grid [Monkhorst and Pack, 1976] of 4x4x4 was employed to sample the Brillouin zone. All calculations were spin-polarized, and the magnetic moments of the octahedral and tetrahedral sublattice were always given opposite orientations, in agreement with experimental evidence that the mineral is a ferrimagnet [Devey et al., 2009]. This allowed us to accurately reproduce the cell parameter, with a value of a = 9.83 Å.

3.2.2 SOD and Statistical Mechanics of Configurations

SOD (Site Occupancy Disorder) is a program developed to investigate site-occupancy disorder in solids, by utilising information about the crystal symmetry of the lattice to reduce the configurational space that must be considered, selecting only the symmetrically inequivalent configurations of atoms distributed in the lattice [Grau-Crespo

et al., 2007]. These structures can then be geometry optimised, either using interatomic potential-based programs such as GULP, or, as we have done here, using VASP. It has already been employed successfully in the simulations of ionic distributions in minerals (e.g. Grau-Crespo et al. [2003, 2004, 2010], Ruiz-Hernandez et al. [2010]). Knowledge of the symmetry operators of the parent structure, and consequently all the possible isometric transformations, enables the code to decipher which two configurations are symmetrically inequivalent, simply by the fact that if they are equivalent, an isometric transformation will allow for interchange between the two. It is the assumption that after each relaxation, all of the configurations will still retain the same symmetry operators as that of the parent structure, allowing of course for symmetry breaking caused by the substitution of, in this instance, nickel. The likelihood of occurrence and the thermodynamic properties of a particular configuration can be described via a Boltzmann-like probability obtained through a series of equations.

If it is considered that all configurations are in thermodynamic equilibrium at temperature T, each configuration n in the complete space (n = 1,..., N) can then be assigned an occurrence probability:

$$P_n = \frac{1}{Z}\exp\left(\frac{-E_n}{k_B T}\right) \tag{3.4}$$

where E_n is the energy of that configuration, k_B is Boltzmann's constant and equal to 8.6173 x 10^{-5} eV K^{-1}, and Z is the partition function defined as:

$$Z = \sum_{n=1}^{N} \exp\left(\frac{-E_n}{k_B T}\right) \tag{3.5}$$

This means that at configurational equilibrium, the energy of the system can be calculated as an average

$$E = \sum_{n=1}^{N} P_n E_n \tag{3.6}$$

and the configurational free energy can be calculated from the partition function as:

$$F = -k_B T lnZ \tag{3.7}$$

with the configurational entropy S simply taken as:

$$S = \frac{E - F}{T} \tag{3.8}$$

The above equations can then be translated to the reduced configurational space. The probability $\tilde{P}$ of an independent configuration m ($m = 1, ..., M$) with degeneracy Ω_m occurring is

$$\tilde{P}_m = \frac{1}{Z}\Omega_m \exp\left(\frac{-E_m}{k_B T}\right) = \frac{1}{Z}\exp\left(\frac{-\tilde{E}_m}{k_B T}\right) \tag{3.9}$$

where $\tilde{E}_m$ is the reduced energy such that

$$\tilde{E}_m = E_m - T S_m \tag{3.10}$$

which can be seen as a temperature-dependent free energy associated with the degeneracy entropy S_m:

$$S_m = k_B T \ln\Omega_m \tag{3.11}$$

The degeneracy entropy accounts for the effect of the configuration degeneracy and enables us to make direct comparisons of independent configurations via the reduced energies (which contain information on both the energy and degeneracy). In particular, if two configurations have the same energy, the one with the higher degeneracy will have higher degeneracy entropy, which in turn lowers its reduced energy $\tilde{E}_m$, resulting in a higher probability of that configuration occurring. The energy and partition function can thus be calculated in the reduced space as:

$$E = \sum_{m=1}^{M} \tilde{P}_m E_m \tag{3.12}$$

$$Z = \sum_{m=1}^{M} \exp\left(\frac{-\tilde{E}_m}{k_B T}\right) \tag{3.13}$$

As external pressure is assumed to be null, the enthalpy of each configuration is simply the energy of each configuration.

When there is access to the full configurational spectrum, then exact statistics are performed within the given supercell [Grau-Crespo et al., 2004, 2010, Ruiz-Hernandez et al., 2010]. Such calculations are conducted using the program SOD, whereby the probability of a configuration occurring can be calculated via equation 3.9, and any variable A then averaged using:

$$< A >= \sum_{m=1}^{M} P_m A_m \tag{3.14}$$

For low Ni-dopant concentrations, all the different configurations of (Fe,Ni) substitutions in the simulation cell were evaluated, using the SOD program. However, at high dopant concentrations, it becomes increasingly difficult to calculate the full configuration spectrum (as discussed in Section 3.4), and therefore a model was devised based on nearest-neighbour (NN) concentration-dependent interactions (hereafter referred to as the NN model), which was then implemented using Monte Carlo methods.

3.2.3 NN Model and Monte Carlo Methods

The results obtained from our DFT calculations were used to fit a model whereby the energy of any configuration could be calculated quickly using nearest-neighbour interactions. The model is based on an Ising-type Hamiltonian with three types of nearest-neighbour (NN) interactions and separate concentration-dependent substitu-

tion energies for tetrahedral (A) and octahedral (B) sites:

$$E = E_o + N_A\varepsilon_A + N_B\varepsilon_B + N_{AA}J_{AA} + N_{BB}J_{BB} + N_{AB}J_{AB} \tag{3.15}$$

where N_A and N_B refer to the number of Ni ions in A and B sites, and N_{AA}, N_{BB} and N_{AB} refer to the number of tetrahedral-tetrahedral, octahedral-octahedral and tetrahedral-octahedral nearest-neighbour Ni-Ni pairs. These parameters are specific for each configuration. E_o is the energy of un-doped (pure iron) greigite, and the constants J then refer to the interaction energies between Ni ions in the corresponding NN sites. ε_A and ε_B are the costs of individual Ni substitutions in sites A and B, respectively, and these values are allowed to vary linearly with concentration as:

$$\varepsilon_A = \varepsilon_A^o(1+\alpha x);\ \varepsilon_B = \varepsilon_B^o(1+\beta x) \tag{3.16}$$

where ε_A^o and ε_B^o are the costs of placing a nickel in the A or B site in the limit of low concentrations, and α and β are the rate at which the substitution energies change with concentration in the respective tetrahedral and octahedral sites. This leads to an energy model with a total of seven parameters. The DFT data used for the fitting consisted of all configurations with $N = 0-3$ Ni per unit cell; all configurations with $4 \leq N \leq 8$ and either pure tetrahedral or pure octahedral occupancy; and a random selection of tetrahedral/octahedral mixed occupancy configurations for each composition. The final fitted values were ε_A^o = 2.590 eV, ε_B^o = 2.091 eV, α = -1.02741, β = 0.07771, J_{AA} = 0.05465 eV, J_{BB} = -0.02997 eV, J_{AB} = 0.05290 eV, while E_o was taken directly from the DFT calculation of pure greigite.

We then used Monte Carlo methods to simplify the configurational space to be sampled, a procedure used successfully in other investigations [Lavrentiev et al., 2003, Purton et al., 2005]. We implemented our NN Model in a code which would generate configurations randomly and calculate their energies in accordance with our model, and whose acceptance or rejection was based on the Metropolis algorithm

[Metropolis et al., 1953] (for a basic outline of the code, see Appendix).

This procedure involves a series of steps, the first of which involves a calculation of the energy difference, ΔE, between the current (m) and previously accepted ($m-1$) configurations generated:

$$\Delta E = E_m - E_{m-1} \tag{3.17}$$

If $\Delta E < 0$, then the configuration is accepted. Otherwise, a random number r is generated such that $0 < r < 1$, and the condition of acceptance then becomes:

$$r < exp(-\Delta E/k_B T) \tag{3.18}$$

Within this procedure, a technique known as importance sampling was utilised, whereby configuration m evolves from the previous configuration $(m-1)$ [Landau and Binder, 2009]. In the absence of importance sampling, calculations are performed using an arbitrary set of configurations selected from any random probability distribution. This can have a detrimental effect on the efficiency of the procedure and the variable that is being calculated. If, however, certain factors are known to have a significant impact on that parameter, and are thus deemed "important", the sampling can be biased in such a way that the distribution is chosen so that emphasis is placed on these factors and they are sampled more regularly.

Hence, the generation of our "random" configurations is biased in such a way that the previous accepted configuration is used as a template for the new one, with the difference that two of the ions swap sites within the lattice (a swap which will always involve one dopant Ni cation with the original species, Fe).

This ensures that the samples are collected from a more concentrated non-uniform distribution where the integral of the function has a large value, meaning that the collected data has a greater relevance to, and impact on the final variable. This technique also helps to speed up the sampling process.

The equilibration time (the duration for which the simulation is allowed to run before we begin to extract data from it) must also be considered. The purpose of equilibration is to eliminate the impact of uncommon/extreme readings on the final result. By allowing the simulation to run over a period of time (defined by ourselves) first, and thereby allowing the system to equilibrate, the range from which the overall average is calculated will be much smaller, and hence the final result more accurate, with exceptionally large or small values bearing little weight on the overall result.

Convergence was monitored by checking the deviation in energy of the new configuration from the previously calculated average, and comparing it to a stipulated parameter. If the difference between the two is less than the value dictated by that parameter, then the calculations are accepted to have converged for that particular concentration of dopant, otherwise the simulation is allowed to keep running until this condition has been satisfied.

The validity of our model was checked by plotting the energies of greigite per nickel substitution from DFT and the Nearest-Neighbour Energy Model against one another, as replicated in Figure 3.5. The clear correlation between the energies obtained from these two differing methods justifies the use of this model when calculating energies and dopant distributions over the A and B sites at higher concentrations of nickel.

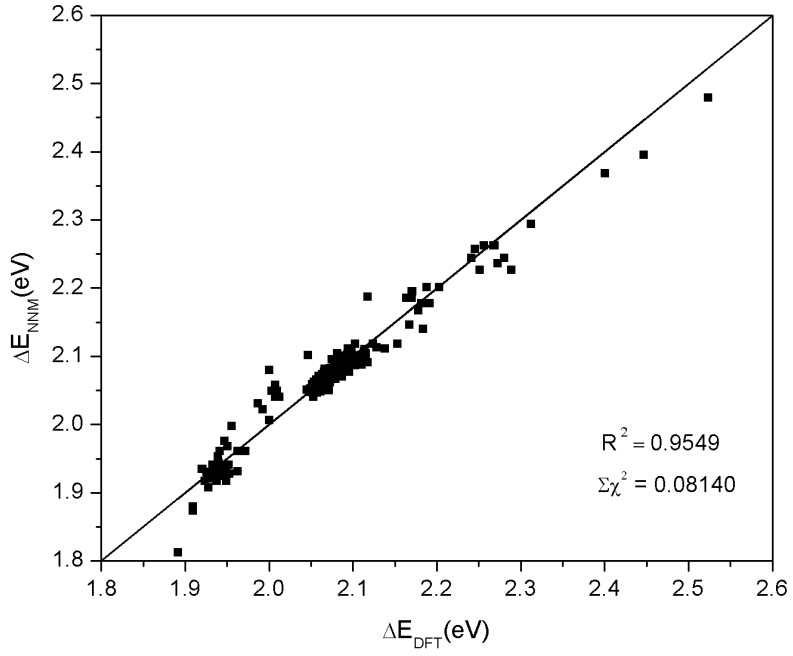

Figure 3.5: Comparison between the energies per Ni substitution as calculated with DFT and those calculated with a nearest-neighbour interaction model (NNM). R^2 is the linear correlation coefficient, which measures the strength of correlation between the variables. $\Sigma\chi^2$ is the residual sum of squares, and is a measure of the discrepancies between the NNM and the DFT results.

3.3 Ni-doping of Greigite at Low Concentrations

For low concentrations of nickel in greigite (0-3 ions per unit cell, or fractional concentrations $x \leq 0.125$ in $(Ni_xFe_{1-x})_3S_4$), it was possible to obtain the full configurational spectrum via DFT calculations. Table 3.1 shows the average solution energy E_S, per dopant N, of each configuration for a simulation cell of 56 atoms, and is calculated via equation 3.19:

$$E_S = \frac{E(\mathrm{Fe}_{24-N}Ni_N\mathrm{S}_{32}) - \frac{24-N}{24}E(\mathrm{Fe}_{24}\mathrm{S}_{32}) - \frac{N}{24}E(\mathrm{Ni}_{24}\mathrm{S}_{32})}{N} \tag{3.19}$$

which in this instance calculates the energetic cost of removing a nickel ion from polydymite and substituting into greigite, in place of an iron. From Table 3.1 it also becomes apparent that each subsequent addition of Ni into an A site leads to a greater increase in energy than the equivalent substitution into one of the B sites. For instance, if we look at a concentration of two Ni per unit cell, then placing one Ni in each of the A and B sites (rather than having both located in the B sites) leads to an increase in E_S by 0.208 eV, and to place both Ni in the A sites leads to another (albeit smaller) increase in the E_S by 0.142 eV. The difference in solution energy between the $1\mathrm{Ni}_B$ and $1\mathrm{Ni}_A$ configurations is 0.440 eV, whilst the difference between the $3\mathrm{Ni}_B$ and $3\mathrm{Ni}_A$ configurations is less pronounced at 0.201 eV, suggesting that the energetic cost of placing a Ni in one of the A sites over the B sites may decrease at higher concentrations of the dopant.

Table 3.1: Results of DFT calculations at low concentrations (x = 0.0417 - 0.125) of Ni in the unit cell. N refers to the total number of Ni ions in the unit cell, N_A and N_B are the number of Ni ions in the tetrahedral and octahedral sites respectively, and E_S is the average solution energy (per dopant). In each case, the energy of the most stable configuration is given for that concentration.

N	N_A	N_B	E_S (eV)
1	0	1	-0.504
	1	0	-0.064
2	0	2	-0.536
	1	1	-0.328
	2	0	-0.187
3	0	3	-0.543
	1	2	-0.423
	2	1	-0.346
	3	0	-0.342

In order to explain the initial trends observed from these results, we decided to focus on the substitution of one Ni in the unit cell, for which there are only two possible substitutional configurations: in an octahedral or in a tetrahedral site. The energy of the substitution in the tetrahedral site is $\Delta\varepsilon$ = 0.439 eV higher than in the octahedral site, as we have calculated. In order to interpret this energy difference, we then calculated the occupancies x_A and x_B of the two types of sites in the limit of very low overall concentrations x from the equation:

$$\frac{x_A}{x_B} = e^{-\frac{\Delta\varepsilon}{RT}} \tag{3.20}$$

which together with the condition

$$\frac{1}{3}x_A + \frac{2}{3}x_B = x \tag{3.21}$$

leads to

$$x_A = \frac{3xe^{-\frac{\Delta\varepsilon}{RT}}}{2+e^{-\frac{\Delta\varepsilon}{RT}}}; x_B = \frac{3x}{2+e^{-\frac{\Delta\varepsilon}{RT}}} \tag{3.22}$$

In real samples the distribution of cations is unlikely to be equilibrated at room temperature because the thermal energy is not enough to overcome the activation barriers for cation diffusion. We therefore discuss here the equilibrium distribution of cations at a representative temperature, T = 600 K, which is chosen close to the maximum temperature at which the whole $(Ni_xFe_{1-x})_3S_4$ series is known to be stable [Vaughan and Craig, 1985]. At this temperature, $x_A = 0.0003x$, which means that in the limit of low concentrations only 0.01% of the total Ni content would be in tetrahedral sites.

For two or more Ni atoms per unit cell, the analysis cannot be done in terms of one energy difference, because there are several possible configurations for the ions in the cell (Table 3.2). For example, for 2 Ni atoms in the cell there are 24!/(22!2!) = 276 combinations, of which 7 are symmetrically different. These include configura-

tions with both Ni in octahedral positions, configurations with both Ni in tetrahedral positions, and configurations with one octahedral and one tetrahedral Ni. In this case, the effective Ni occupancy of the tetrahedral (A) sites can be obtained as an average (equation 3.14) of the Ni tetrahedral occupancies of the configurations:

$$x_A = \frac{1}{8} \sum_{m=1}^{M} P_m t_m \tag{3.23}$$

where t_m is the number of tetrahedral Ni atoms per cell in configuration m, which has probability P_m (equation 3.9). At 600 K and Ni concentrations x = 0.0833 and 0.1250 (2 and 3 Ni per cell), the tetrahedral site occupancies are 4.3 x 10^{-4} and 4.1 x 10^{-3}, which correspond to 0.5% and 3.3% of the total Ni content, respectively. This in turn means the corresponding octahedral occupancies at these Ni concentrations are 99.5% and 96.7%.

From this it becomes apparent that although Ni strongly prefers to occupy octahedral positions when substituted at low concentrations, an increase in the overall concentration leads to an increase in the fraction of Ni occupying tetrahedral positions. Whether this trend remained at even higher concentrations, we hoped to establish via our NN Model and Monte Carlo simulations.

Table 3.2: Number of cation configurations as a function of the total number n of Ni ions per unit cell.

n	Total number of configurations	Symmetrically inequivalent configurations
1	24	2
2	276	7
3	2024	25
4	10626	97
5	42504	297
6	134596	853

3.4 Heavy Ni-doping of Greigite: Monte Carlo Simulations

From Table 3.2 it is shown that at higher dopant concentrations (more than 3 Ni ions per cell, or $x > 0.125$), it becomes too expensive to perform DFT calculations of the entire configurational spectrum, due to the large number of possible configurations. We therefore relied on our NN model to run Monte Carlo simulations at 600 K for concentrations $0 \leq x \leq 0.333$. This enabled us to extract the average energies and tetrahedral occupancies at each concentration from the accepted configurations. The calculated tetrahedral/octahedral partition for the whole range of concentrations is shown in Figure 3.6, where we show the total Ni concentration (x) as a sum of both tetrahedral ($\frac{1}{3}x_A$) and octahedral ($\frac{2}{3}x_B$) contributions. Part a) illustrates the distribution of cations that is expected in the full disorder limit, where the concentration of nickel in the A sites is always one-third of the total nickel concentration. Part b) of Figure 3.6 shows the Monte Carlo result at 600 K, which deviates significantly from the random distribution. As discussed above, at low Ni concentrations, B site substitutions are strongly favoured, while at higher concentrations there is a greater proportion of nickel ions in the A sites than in the B sites. The change in site preference occurs between $x = 0.20$ and $x = 0.25$. At x = 1/3, 87% of the Ni is located in tetrahedral sites. This could come as surprise in entropy terms, where the 2:1 ratio of B to A sites would imply that there are a greater possible number of arrangements within the B sites, and thus these should be favoured. Thus, the preference for the A sites at these high concentrations may be best explained by referring back to the coefficients obtained from the fitting of our NN model to our DFT results. Although the coefficient J_{BB} has a negative value of -0.02997 indicating that it is energetically favourable to place nickel ions within B sites that "pair" with one another, the value of α which corresponds to substituting a nickel ion in any tetrahedral site (in relation to the total Ni concentration) regardless of what position or "pairs" are formed, is

considerably more negative at -0.1108 eV. This means that the energetic interactions within the A sites at higher concentrations of nickel become much more favourable.

The plateau in the amount of tetrahedral Ni near $x = 1/3$ in Figure 3.6 should be expected, as this represents complete saturation of the tetrahedral sites (of which there are only 8). This is also consistent with observations that violarite $FeNi_2S_4$, with an even higher Ni/Fe ratio, has only Ni in its tetrahedral sites [Tenailleau et al., 2006, Waldner, 2009].

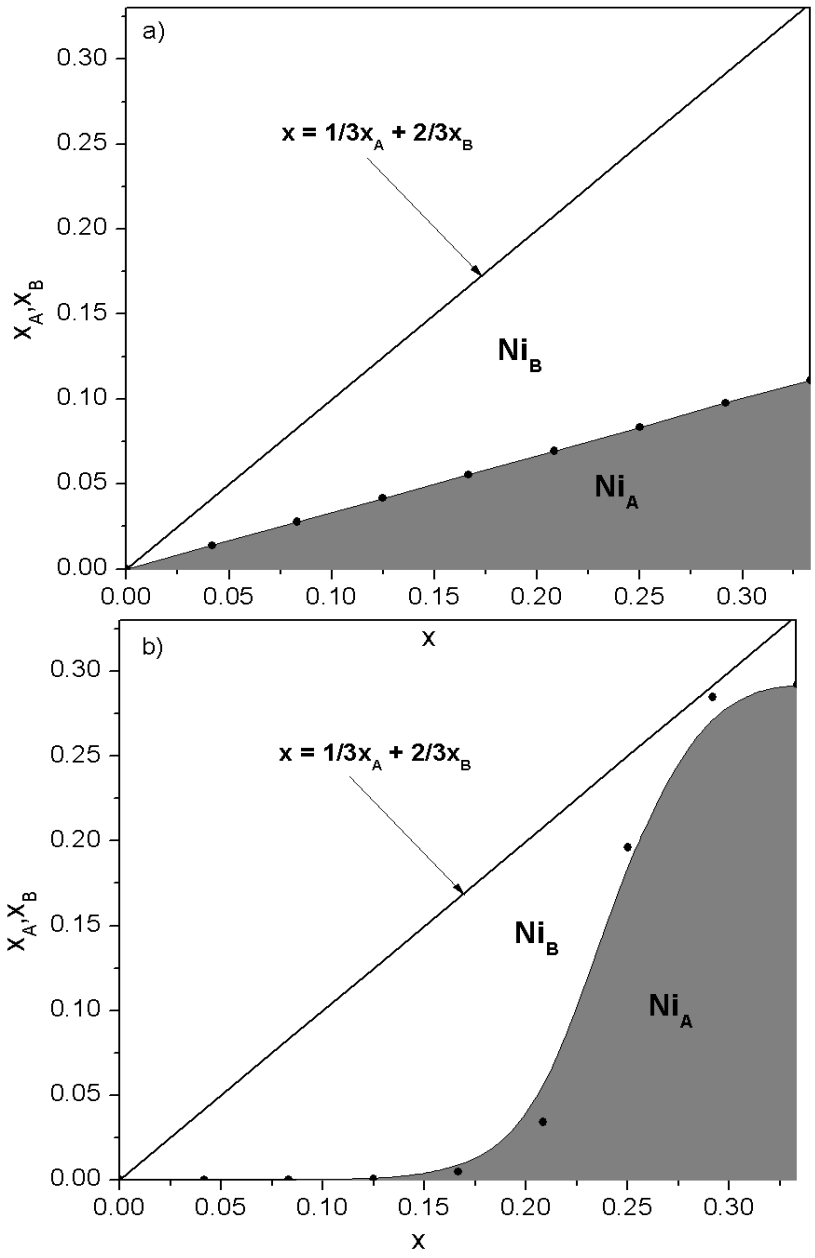

Figure 3.6: Distribution of Ni ions over tetrahedral and octahedral sites as a function of the total Ni concentration (x), at a) $T \to \infty$ K, and b) T = 600 K.

3.5 Mixing Thermodynamics in (Fe,Ni) Thiospinels

The enthalpy of mixing between greigite and polydymite (Ni_3S_4) was calculated in accordance with equation 3.24:

$$\Delta H_{mix} = E[(Fe_{1-x}Ni_x)_3S_4] - (1-x)E[Fe_3S_4] - x[Ni_3S_4] \tag{3.24}$$

where we have ignored zero-point energy and pressure-volume contributions to the mixing enthalpy, which are typically small. The result is shown in Figure 3.7(a), including data obtained from both DFT and the NN interaction models. The energies of violarite, polydymite and Fe-doped polydymite were obtained directly from DFT calculations. In the case of violarite, the energy is a Boltzmann-weighted average of 97 configurations.

It is clear that violarite (x = 0.666) is the most energetically stable member of the (Fe,Ni)S solid solution series, with a very negative enthalpy of mixing of -15 kJ mol^{-1}, whilst Ni-doped greigite has a positive enthalpy of mixing. In order to obtain the maximum concentration of Ni dopants that is stable in greigite with respect to separation into violarite, we re-write the formula for Ni-doped greigite as $Fe(Fe_{1-y}Ni_y)_2S_4$, where $y = \frac{3x}{2}$. Now y = 0 corresponds to greigite and y = 1 to violarite. The mixing enthalpy between greigite and violarite is shown in the inset in Figure 3.7(a). ΔH_{mix}(y) is positive, at least for all values of y studied here ($0 < y < 0.5$). At low concentrations, the dependence with y is linear with slope W = 38.9 kJ mol^{-1}. This large value (compared to RT) indicates that it is energetically unfavourable to move Ni from violarite to greigite. We can estimate the maximum concentration of Ni that is stable in greigite from the minimum of the mixing free energy:

$$\Delta G_{mix}(y) = Wy - T\Delta S_{mix}(y) \tag{3.25}$$

where we use the linear expression for the mixing enthalpy because the minimum

can be expected to occur at low concentration due to the large W value. The mixing entropy can then be obtained from the configurational entropies of Ni-doped greigite and violarite (there is no configurational entropy in pure greigite), ignoring the small vibrational contributions, as:

$$\Delta S_{mix}(y) = S[\mathrm{Fe(Fe_{1-y}Ni_y)_2S_4}] - yS[\mathrm{FeNi_2S_4}] \tag{3.26}$$

where

$$S[\mathrm{Fe(Fe_{1-y}Ni_y)_2S_4}] = -2k_B[y\ln y + (1-y)\ln(1-y)] \tag{3.27}$$

is the entropy associated with the disorder of Ni dopants in greigite, assuming they are all in octahedral sites (which is accurate at very low concentrations as discussed previously), and

$$S[\mathrm{FeNi_2S_4}] = 2k_B \ln 2 \tag{3.28}$$

is the entropy of disorder in the octahedral sites of violarite, which are occupied by Ni and Fe in a 50:50 proportion. The factor of 2 in equations 3.27 and 3.28 accounts for the presence of two octahedral sites in each formula unit. The mixing free energy at T = 600 K has a minimum at approximately y = 0.01 ($\mathrm{Fe(Fe_{0.99}Ni_{0.01})_2S_4}$ or Ni:Fe = 1:150), where Ni is mainly octahedral. This corresponds to the maximum equilibrium concentration (solubility) of Ni in greigite. Since most Ni is in octahedral sites at any reasonably low temperature and the Ni-Ni interaction is negligible at low concentrations, W does not vary appreciably with temperature and we can estimate the solubilities over a small range of temperatures, as shown in Figure 3.7.(b). Although the solubility increases with temperature, even at 700 K the maximum Ni:Fe ratio in thermodynamic equilibrium is around 1:87. The consideration of higher temperatures is not relevant, as we have already discussed that the (Fe,Ni)S solid solution series will not be stable at such high temperatures [Vaughan and Craig, 1985].

The analysis enabled us to see that Ni doping of greigite is thermodynamically very unfavourable with respect to the competitive formation of violarite $FeNi_2S_4$. Metastable incorporation beyond these limits is possible, as occurs in many minerals due to kinetic control of mineral growth. However, our results indicate that low Ni/Fe thiospinels would not be very abundant, and there is a notable lack of reports of any such minerals being found in nature.

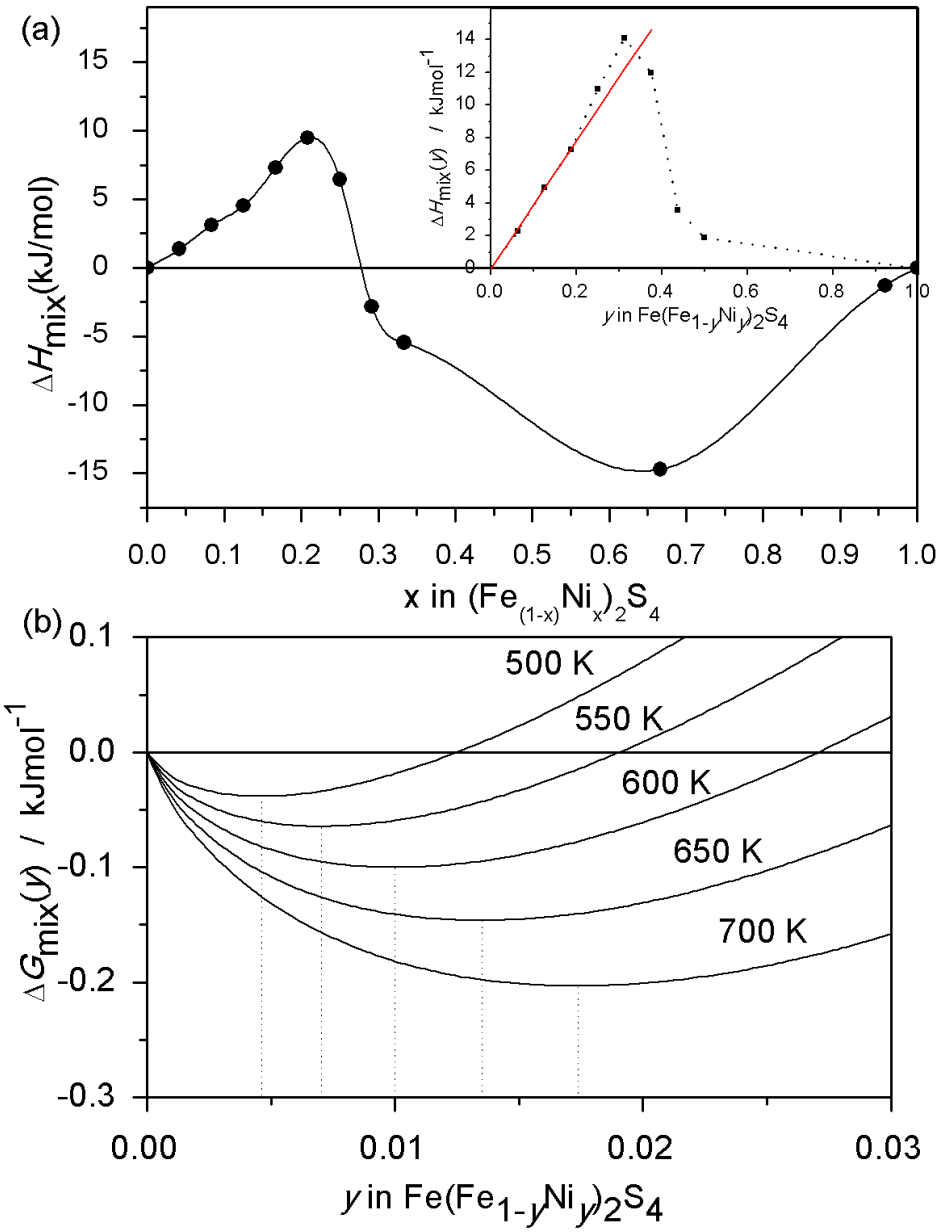

Figure 3.7: (a) The energy of mixing $\Delta H_{mix}(x)$ calculated per formula unit with respect to greigite ($x = 0$) and polydymite ($x = 1$) ($x = 0.666$ corresponds to violarite). Inset: $\Delta H_{mix}(y)$ calculated per formula unit with respect to greigite ($y = 0$) and violarite ($y = 1$). (b) The free energy of mixing $\Delta G_{mix}(y)$ calculated with respect to greigite ($y = 0$) and violarite ($y = 1$) at a range of different temperatures.

3.6 Variation of Bond Lengths and Cell Parameter with Composition

Table 3.3 shows the bond lengths of Fe-S/Ni-S obtained from our DFT optimisations of pure greigite, polydymite, and greigite with one nickel substituted in place of a tetrahedral or octahedral iron. Inclusion of one Ni in either of the lattice sites in greigite leads to a decrease in the equivalent cation-sulphur bond length in pure greigite, although the bond distance is still greater than those Ni-S bonds found in polydymite. Yet the effect of Ni substitution on the adjacent Fe-S bonds varies depending on which lattice site is occupied by the dopant. When Ni is substituted in the tetrahedral site, the distance between the Fe coordinated to the same S as Ni also decreases. However, when Ni occupies an octahedral site, then the surrounding Fe-S bonds will be slightly longer than those found in pure greigite, effectively counteracting the decrease in bond length caused by Ni substitution. This effect explains why at this low concentration, substitution of Ni into a tetrahedral site in greigite will lead to a greater reduction in cell parameter than for the equivalent octahedral site substitution.

Table 3.3: Relaxation geometries from DFT calculations.

Structure	Cell parameter a (Å,to 3 s.f.)	Bond type	Length (Å)
$Fe_{24}S_{32}$	9.83	Fe_A-S	2.199
		Fe_B-S	2.413
$Ni_{24}S_{32}$	9.47	Ni_A-S	2.190
		Ni_B-S	2.289
$Ni_AFe_{23}S_{32}$	9.77	Ni_A-S	2.175
		Fe_B-S(-Ni_A)	2.387
$Ni_BFe_{23}S_{32}$	9.80	Ni_B-S	2.399
		Fe_B-S(-Ni_B)	2.433
		Fe_A-S(-Ni_B)	2.213

These geometrical effects link in with the results displayed in Figure 3.8, which shows that substitution of the first eight Ni into the greigite unit cell leads to a sharp

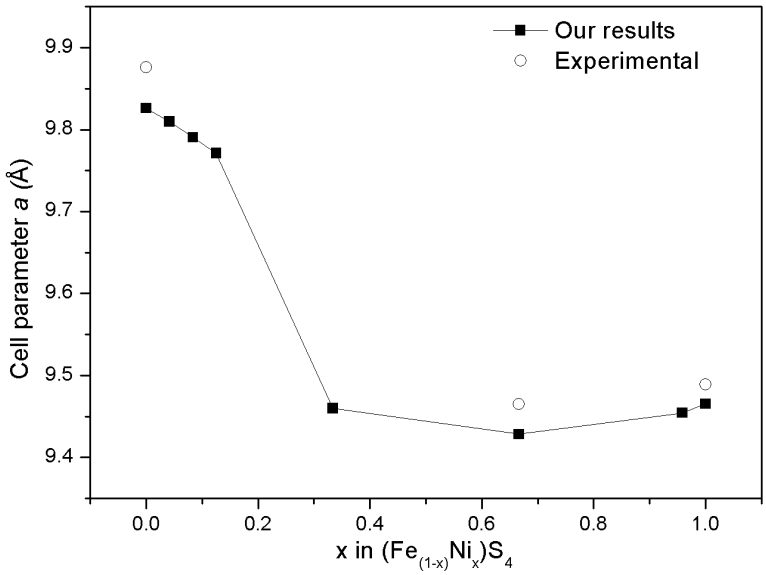

Figure 3.8: Variation in cell parameter as calculated via DFT methods and the Nearest Neighbour Energy Model, shown alongside experimental results [Craig, 1971].

decrease in the cell parameter, by a value of approximately 0.366 Å. Yet substitution of a further eight Ni (to form violarite) is accompanied by a further reduction of only 0.032 Å. The implication is again that, as suggested from our DFT calculations, the biggest distortion of the unit cell occurs from occupation of the tetrahedral sites by Ni (we know from our NN Model that the first 8 Ni will occupy all of the A sites). It should also be noted that the trend exhibited by cell parameter *a* shows a deviation from Vegard's law, but is supported by experimental measurements [Craig, 1971]. Vaughan and Craig [1978] explain this phenomenon in the context of the number of electrons in the anti-bonding σ^* orbitals. As noted before, the numbers (per formula unit) for greigite, violarite and polydymite are 7, 4 and 6, respectively. The greater the number of electrons occupying these orbitals, the greater the repulsive effect on the proximal sulphur ligands, and thus the larger the cell parameter.

3.7 Conclusions

We have used a combination of techniques to show that the partitioning of Ni between tetrahedral and octahedral sites in (Fe,Ni) thiospinels, $(Fe_{1-x}Ni_x)_3S_4$, is strongly dependent on the composition. At low concentrations ($x < 0.2$) there is a strong preference for octahedral (B) site occupation by Ni. This result is significant as it breaks the analogy between Ni-doped greigite and biological enzymes with (Fe,Ni)S clusters, where Ni is usually tetra-coordinated [Dobbek et al., 2001, Gencic et al., Ragsdale, 2009, Svetlitchnyi et al., 2004, Volbeda and Fontecilla-Camps, 2003, 2005, Volbeda et al., 1995]. The analogy in coordination environment is better for the thiospinels with higher Ni concentrations ($x > 0.25$), where Ni ions locate preferentially in the tetrahedral (A) sites.

It should also be noted that in enzymes such as CODH, there are four Fe ions and only one Ni ion in the active C-cluster [Dobbek et al., 2001, Ragsdale, 2009, Thauer, 2001], which partly explains why the Iron-Sulphur Membrane Theory papers refer to Ni-doped greigite rather than violarite, which has a higher Ni/Fe ratio. Yet $(Fe_{1-x}Ni_x)_3S_4$ minerals with a low concentration of nickel are not very abundant or are not well documented, which coincides with our own results, showing that Ni doping of greigite is highly unstable with respect to separation into a violarite phase.

Chapter 4

VIOLARITE: SURFACE CHARACTERISATION AND THE ADSORPTION OF WATER

In this chapter, DFT simulations of the bulk and surfaces of violarite are presented, and the subsequent adsorption and dissociation of water. We first discuss the characterisation of the low-Miller index surfaces ((001), (011) and (111)), to ascertain which is the most stable thermodynamically. Reaction energy pathways are then calculated to highlight whether or not the adsorption and catalytic dissociation of water is possible, but also which surface would be the most reactive with respect to water, focusing on the different possible cationic sites for adsorption.

4.1 Introduction

Violarite was first identified by Lindgren and Davy [1924], who noticed that a violet-coloured nickel sulphide mineral was replacing pentlandite in deposits, forming as a secondary mineral, possibly as a result of supergene[1] alteration. The initial com-

[1] Supergene processes refer to those that occur near of at the earth's surface.

position was determined to be approximately $(Ni,Fe)_3S_4$ [Short and Shannon, 1930], and later studies confirmed the more exact formula of $FeNi_2S_4$ [Craig, 1971]. Natural and synthetic violarites can be found with a higher Fe:Ni ratio, but only with a compromise in stability [Misra and Fleet, 1974, Nickel et al., 1974, Townsend et al., 1977, Warner et al., 1996, Xia et al., 2008]. The mineral is thus said to belong to the same solid solution series as greigite and polydymite [Vaughan and Craig, 1985].

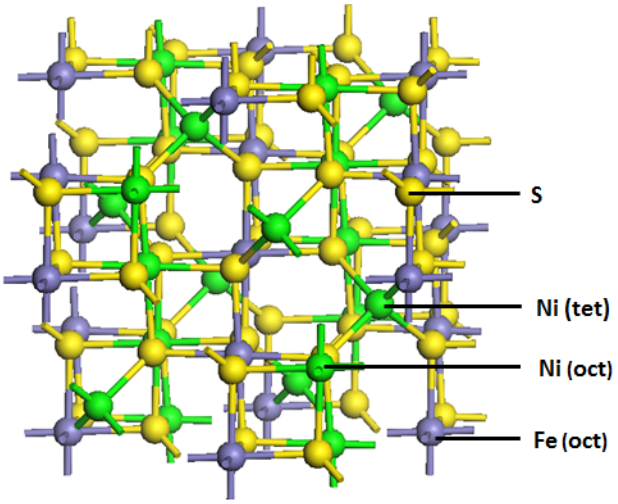

Figure 4.1: Violarite as seen along the c-axis; S in yellow, Fe in purple, Ni in green.

Violarite has important economic uses, namely as a nickel-ore mineral [Hui et al., 2004, Jørgensen et al., 2012]. It forms an important component of the nickel sulphide concentrate used as a feedstock in the production of nickel matte, via flash-smelting. It is ubiquitous in several nickel sulphide deposits in Western Australia, where in some instances it is the predominant nickel mineral [Dunn and Howes, 1996].

The importance of violarite in the context of Origin of Life theories has already been discussed in Chapter 1, and so the need for further study into this mineral is obvious. More specifically, there exists no information in the literature regarding characterisation of violarite's surfaces, nor its potential catalytic activity. We have already extensively discussed how the reactions believed to be responsible for the origin of life were catalysed on the ocean floor. This, in addition to violarite occuring

in sediments as a result of supergene alteration, which may involve chemical alteration via circulating water, led us to simulate the adsorption of H_2O on these mineral surfaces. In light of the potential catalytic activity, we wished to study the dissociation of H_2O on the surfaces to form H and OH groups, as this could lead as a gateway to other possible chemical reactions on the surface.

Before discussing the results from our simulations of the mineral's surfaces, we precede with a review of the violarite literature.

4.1.1 Violarite: Structure and Properties

Belonging to the same solid solution series as greigite and polydymite [Hui et al., 2004, Vaughan and Craig, 1985], violarite's Ni and Fe atoms occupy tetrahedral (A) and octahedral (B) sites within a ccp array of S atoms. A member of the $Fd3m$ space group, it has a cell parameter of a = 9.465 Å [Craig, 1971]. As with greigite, the unit cell is composed of eight AB_2S_4 units [Vaughan and Craig, 1978]. Neutron powder diffraction studies [Tenailleau et al., 2006] confirmed that the structure was based on an inverse spinel structure, by showing the charge and distribution of the cations to be $Ni^{3+}_{A}(Fe^{2+}, Ni^{3+})_{B}S_4$. The octahedral cations cations have also been shown to exist in a low-spin state [Vaughan and Craig, 1985, Vaughan and Ridout, 1971], unlike those in greigite. The mineral was found to be metallic and Pauli-paramagnetic [Townsend et al., 1977], with a maximum thermal stability at around 461 °C in the Fe-Ni-S system [Craig, 1971]. The colour of violarite has been shown to range from violet-grey-pink to greyish-yellow, yet there appears to be no connection between its composition and colour [Misra and Fleet, 1974].

4.1.2 Violarite: Formation and Synthesis

Violarite is commonly found in (Fe,Ni) sulphide assemblages that contain pentlandite [Misra and Fleet, 1974, Short and Shannon, 1930, Townsend et al., 1977], and the

replacement of pentlandite by this mineral was noted by Lindgren and Davy [1924] , who suggested that its formation was supergene, as supported by later studies [Dunn and Howes, 1996].

The main mechanisms for its formation include the following [Chamberlain and Dunn, 1999, Hui et al., 2004, Tenailleau et al., 2006]:

- The alteration of pentlandite $(Fe,Ni)_9S_8$ and pyrrhotite (FeS), which also results in the formation of pyrite.
- The alteration of millerite-pentlandite (NiS-$(Fe,Ni)_9S_8$) assemblages, which results in the production of violarites more Ni-rich than those formed via the above process.
- Formation during the later stages of millerite formation, which sees the formation of even more Ni-rich violarites that have compositions approaching that of polydymite (Ni_3S_4).
- As a hypogene[2] product via the exsolution of pentlandite.

The occurrence of violarite in these assemblages is often associated with other sulphides and oxidation products [Dunn and Howes, 1996], and this is mirrored by a difficulty in the synthesis of pure violarite from its host matrix/precursors.

Craig [1971] reported one of the first, albeit lengthy, procedures for the preparation of violarite, consisting of two main steps conducted over a three month period. Step one consisted of the preparation and heating of a monosulphide solid solution (Mss) with Fe and Ni in a 1:2 ratio at $500-700\,^{\circ}C$, followed by grinding and reheating/reannealing for 2-3 days to achieve homogenisation, resulting in the formation of a Mss with formula $FeNi_2S_{3.25}$. The second stage consisted of finely grinding the Mss, and reacting it with the necessary amount of sulphur to achieve the desired $FeNi_2S_4$ composition, at temperatures of $200-300\,^{\circ}C$. Despite contamination of

[2]Hypogene processes are those which occur deep below the earth's surface.

the final product with (Fe,Ni)S_2 and (Ni,Fe)$_{1-x}$S, modified versions of this lengthy two-step process have been employed in many successful investigations of violarite [Chamberlain and Dunn, 1999, Dunn and Howes, 1996, Hui et al., 2004, Townsend et al., 1977].

Xia et al. [2008] developed a hydrothermal route for the synthesis of violarite using pentlandite as a precursor, which would only take between 10-20 days, compared to the three-month procedure described above. This hydrothermal replacement reaction also consists of two steps primarily: the first involves the preparation of ((Fe,Ni)$_9S_8$) as a precursor via dry synthesis, which is then followed by ion replacement via a coupled dissolution-reprecipitation replacement reaction under mild hydrothermal conditions. This latter stage is conducted at temperatures between $125-165\,^{\circ}$C using a stainless-steel flow-through closed-loop hydrothermal cell, with the fluid flow improving mass transfer and flushing away Fe_2O_3 byproduct. The reaction begins at the outer surface of the precursor and then proceeds inward towards the core, with the hydrothermal fluid transporting metals to and from the reaction front. It was found that by varying the temperature and pH and precursor stoichiometry, they could control the Ni/Fe ratio in the (Fe,Ni)$_2S_4$ that was formed. Not only is this method quicker, but the products obtained are of a higher purity than those produced from the dry synthesis.

Even more recently, another method for the hydrothermal precipitation of artificial violarite has been reported [Jørgensen et al., 2012]. Here, iron (II) acetate, nickel (II) acetate and DL-penicillamine [$(CH_3)_2C(SH)CH(NH_2)$] are dissolved in distilled water to prepare an aqueous solution, before being inserted into a stainless steel autoclave, and heated in an electric furnace at $130\,^{\circ}$C for 45 hours. The solution is then filtered and washed with water and ethanol in order to isolate the precipitates, which are then placed in a drying-oven. This is the first procedure whereby violarite ($Fe_{0.34}Ni_{2.36}S_4$) is directly prepared from an aqueous solution of Fe, Ni and S, and paves the way for the synthesis of other (Fe,Ni)S compounds to be formed via

precipitation methods.

4.1.3 Experimental Studies

As with greigite, Mössbauer spectra have proven extremely useful in the elucidation of the crystal structure of violarite. Townsend et al. [1977] originally showed that the Fe in violarite would exist in only one of the two possible lattice sites, most likely the octahedral. Vaughan and Craig [1985] later recorded Mössbauer spectra for synthetic violarite and observed a quadrupole doublet with a small isomer shift and splitting, which is associated with low-spin Fe^{2+} in the octahedral sites, as this result was comparable to that obtained for low-spin Fe^{2+} in pyrite. Extended X-ray absorption fine spectroscopy (EXAFs) also lent further support to the theory that Fe would be located in the octahedral sites of violarite [Charnock et al., 1990], and that along the Ni_3S_4-$FeNi_2S_4$ series, substitution of Ni for Fe would thus occur in these sites. More recently, Tenailleau et al. [2006] performed a neutron powder diffraction study of the Fe and Ni distribution in synthetic violarite using ^{60}Ni isotope. Their results also confirmed this finding, showing that the tetrahedral sites were occupied solely by Ni, whilst the octahedral sites were occupied by Fe and Ni in equal proportions, giving a fully-ordered, inverse spinel structure.

Townsend et al. [1977] also examined the thermoelectric power and magnetic susceptibility of synthetic and natural violarite and showed that it was metallic and Pauli-paramagnetic. The metallic character was inferred from the fact that the cell parameter (a = 9.45 Å) is comparable in value to other metallic spinels (a = 9.399 Å for Co_3S_4 and a = 9.48 Å for Ni_3S_4), whilst higher values are expected for semi-conducting high-spin spinels (e.g. for greigite a = 9.87 $\AA$). Mössbauer spectra were recorded between 5-300 K, and the absence of magnetic ordering down to 5 K, together with the temperature-independent susceptibility (above 120 K) and the low thermoelectric power, confirmed it is a Pauli-paramagnetic metal.

Various investigations have also been conducted to show the ease of transforma-

tion from pentlandite. Single crystal X-ray diffraction studies [Misra and Fleet, 1974] of a partially violaritised pentlandite grain showed that violarite has the same crystallographic orientation as pentlandite, and that alteration occurs via removal of excess metal atoms from pentlandite and redistribution of the remainder. Richardson and Vaughan [1989] also studied the surface oxidation of pentlandite with the possibility of secondary violarite formation. They saw that primary oxidation resulted in the surface production of iron compounds rather than nickel compounds. Once this had occurred, an iron-rich oxidised layer formed. Further oxidation would then occur through the oxidised layer, leading to further depletion of iron. It is the ion-deficient sub-surface sulphide that then transforms into violarite. The structural transformation involves a 17% reduction in the overall volume, which is accompanied by a decrease in the cell parameter *a* from 10.06 Å to 9.46 Å. Hui et al. [2004] examined the transformation of pentlandite to violarite via exosolution, and their preliminary calculations also revealed that oxidising conditions were key for the exosolution of violarite from pentlandite.

Further research into the thermal stability of violarite has also been conducted, with Craig [1971] reporting the maximum stability of violarite to be at around 461 °C, at which it decomposes to (Fe,Ni)S_2, (Ni,Fe)S_2 and Mss containing Fe, Ni and S in a 1:2:4 ratio. Below this, the solid soluion expands to reach the upper stability limit of polydymite at 356 °C.

Electron microprobe analysis [Misra and Fleet, 1974] performed on natural Fe-Ni-S assemblages showed that the solid solution extends from the Ni-rich end member polydymite to at least 17% Ni in (Fe,Ni)$_3S_4$, whilst newer results show that the complete compositional range from Ni_3S_4 to Fe_3S_4 exists in nature, though it it limited in synthetic samples [Vaughan and Craig, 1985].

4.1.4 Theoretical Studies

Very little theoretical work exists on violarite, but those that do support those findings from experimental investigations.

Warner et al. [1996] re-evaluated the thermodynamic stability of pentlandite and violarite and used these to calculate the Nernst functions for the Fe-Ni-S system and construct E_H-pH diagrams. They calculated that the standard free energy of formation of violarite at 298 K was consistent with the idea of supergene formation in nature, whereby violarite would occur via a cation-exchange nickel-enrichment process:

$$FeNi_2S_4(c) + xNi^{2+}(aq) \rightarrow Fe_{1-x}Ni_{2+x}S_4(c) + xFe^{2+}(aq) \tag{4.1}$$

and the diagrams also reflected the co-existence of pentlandite and violarite in an aqueous system, as observed in nature.

Waldner [2009] also performed thermodynamic modelling calculations via evaluation of experimental data on violarite, developing a model for the Gibbs free energy which also allowed for phase equilibria calculations. Their results reaffirmed the preferential iron substitution of Ni in the octahedral sites.

4.2 Computational Techniques

4.2.1 Surface Calculations

The (001), (011) and (111) surfaces have been created using the METADISE code [Watson et al., 1996]. This code not only considers periodicity in the plane direction, but also provides the different atomic layer stacking resulting in a zero dipole moment perpendicular to the surface plane, which is required for reliable and realistic surface calculations, in accordance with the Tasker approach [Tasker, 1979]. In this formulism, the crystal is considered as a stack of planes, from which there arises three possible surface types:

- Type 1 surfaces: Each plane remains uncharged with no dipole present, due to the stoichiometric ratio of anions and cations within.
- Type 2 surfaces: This consists of three charged, symmetrical planes stacked together, which cancels out any dipole moment perpendicular to the surface.
- Type 3 surfaces: This stacking sequence is composed of alternatively charged planes, producing a dipole moment perpendicular to the surface.

The Coulombic interactions are calculated using the Parry method [Parry, 1975], which is a variant of the Ewald summation [Ewald, 1921], and in this the crystal is considered as a series of charged planes of infinite size, which terminate at the surface in question. This means the Parry sum will yield to infinity if a net dipole moment exists perpendicular to the surface in question. Therefore, Type 3 surfaces need to be reconstructed, and this usually involves moving half of the ions with the same charge from the top to the bottom surface layer of the slab.

The crystal is then considered to consist of a series of charged planes parallel to the surface and periodic in two dimensions. The crystal is divided into two blocks, each of which are further separated into two regions: Region I and Region II [de Leeuw, 2006] (see Figure 4.2). Region I is often though of as the "surface" region, and consists of the surface plane and an additional few layers of ions underneath; these are allowed to relax explicitly to their surface equilibrium positions. Region II refers to the "bulk" region below the surface, and these ions are held fixed in their bulk equilibrium positions. The inclusion of Region II is necessary to ensure that an ion at the bottom of Region I is modelled correctly. The number of layers in each region is varied until the surface energy no longer changes, signifying convergence.

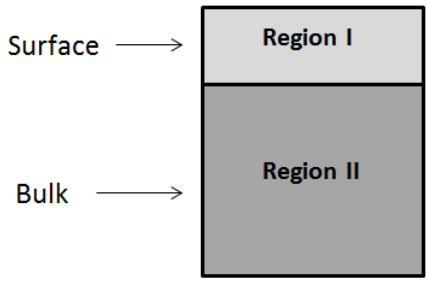

Figure 4.2: The two-region approach, showing half a crystal with the surface exposed.

4.2.2 Surface Relaxation and Characterisation (DFT)

Density functional theory calculations with long-range (Grimme) dispersion corrections [Grimme, 2006] (DFT-D2), were employed to simulate the bulk and surfaces of violarite (once created via METADISE). The Vienna *ab initio* simulation package (VASP) [Kresse and Furthmuller, 1996, Kresse and Hafner, 1993, 1994] was, once again, used here. All calculations were performed within the generalised gradient approximation (GGA), with the exchange-correlation functional developed by Perdew et al. [1992], and the spin interpolation formula of Vosko et al. [1980], and the application of a Hubbard correction with U_{eff} = 1 eV to the Fe d orbitals, to help improve the description of the electron localization [Devey et al., 2009, Haider et al., 2012]. The valence orbitals are calculated as before in Chapter 3, with the size of the basis set determined by a cutoff energy of 600 eV. This means the core electrons are again kept "frozen" during the calculations (so orbitals up to, and including, 3p for Fe and Ni, 2p for S and 2s for O), and the interaction between the valence electrons and core orbitals described using the PAW method [Blöchl, 1994] in the implementation of Kresse and Joubert [1999]. All calculations were spin-polarized, and the magnetic moments of the octahedral and tetrahedral sublattice were always given ferrimagnetic orientations, in agreement with experimental evidence [Devey et al., 2009, Haider et al., 2012].

Calculations were carried out using Monkhorst-Pack grids of 4x4x4 K-points for the bulk, 4x4x1 for the (001) and (011) surfaces, and 3x3x1 for the (111) plane,

which ensures electronic and ionic convergence [Monkhorst and Pack, 1976]. The geometries of all stationary points were found with the conjugate-gradient algorithm and considered converged when the force on each ion dropped below 0.03 eVÅ^{-1} and the energy threshold defining self-consistency of the electron density was set to 10^{-5} eV. In order to improve the convergence of the Brillouin-zone integrations, the partial occupancies were determined using the tetrahedron method with Blöchl corrections [Blöchl, 1994], with a set smearing width for all calculations of 0.02 eV. These smearing techniques can be considered as a form of finite-temperature DFT, where the varied quantity is the electronic free energy.

Bulk calculations of violarite were modelled in a cubic unit cell with a spinel structure containing 56 atoms, of which 16 were Ni (equally distributed over octahedral and tetrahedral sites), 8 were Fe in octahedral sites, and 32 sulphur atoms. All atoms were fully relaxed until the required accuracy was reached. Each block or slab contained 56 atoms, with a vacuum width of 12 Å between vertically repeated slabs to avoid interactions between them. The choice of vacuum width comes from tests with increasing distances until convergence of the surface energy has been achieved. From our convergence of the number of atomic layers to represent the bulk, we identified that two atomic layers were deemed sufficient to model the surfaces of violarite reliably, i.e. 28 atoms were relaxed without any symmetry or direction restrictions.

4.2.3 Geometry Optimisation and Characterisation of Adsorbants (DFT)

For the adsorption and subsequent geometry optimisation of H_2O on violarite's surfaces, VASP was employed in the same manner outlined in Section 4.2.2, where we used DFT-D2 calculations, with long-range dispersion corrections [Grimme, 2006].

Transition states (TS) were obtained by means of the Dimer method [Henkelman and Jonsson, 1999], and their nature was verified by a diagonalisation of the

corresponding Hessian matrix obtained by numerical difference of analytical gradients, neglecting coupling with the cluster-surface phonons and making sure the TS structures show a single normal mode associated with an imaginary frequency.

The Dimer method allows us to start from any initial configuration and search for a nearby saddle point. The Dimer is an image consisting of two points in $3n$ dimensional space, which are displaced by a certain distance. Whenever the Dimer is moved to a new location, the force and energy will be calculated from the force and energy acting on the two points, via interpolation. Consequently, this cancels out the need to separately evaluate the energy and force at the midpoint between them, and this helps to minimise the total number of force evaluations required to find the saddle point. Each time the dimer is displaced, it is also rotated with a single iteration towards the minimum energy configuration.

4.3 Characterisation of the (001), (011) and (111) Surfaces

To model the different terminations of the $FeNi_2S_4$ low-Miller index surfaces, advantage was taken of the crystal symmetry to reduce the number of surfaces to $\{001\}$ (which includes the equivalent (001), (010) and (100) faces), the $\{011\}$ (consisting of the equivalent (011), (101) and (110) faces), and the (111). Owing to the spinel structure of violarite, a total of six different terminations were obtained for the (001), whereas the (011) and (111) surfaces led to two terminations each, due to the cation distribution along the cutting direction [Haider et al., 2012]. The surface energy (γ) is a useful measure of the stability of the crystal surface, and is used to measure the excess energy of the surface with respect to the bulk, calculated via equation 4.2.

$$\gamma = \frac{E_{slab} - nE_{bulk}}{A} - \frac{E_{slab}^{unrelaxed} - nE_{bulk}}{2A} \tag{4.2}$$

$$\%relaxation = \frac{\gamma_{unrelaxed} - \gamma_{relaxed}}{\gamma_{unrelaxed}} x100 \quad (4.3)$$

The unrelaxed surface energy (γ-unrelaxed) corresponds to the surface energy prior to surface geometry optimisation, and accounts for the loss in coordination of the atoms in the top surface layer as a result of the creation of the surface, γ-relaxed corresponds to the surface energy after optimisation, and should be lower in value as the ionic coordinates will have now optimised their positions, E_{slab} is the absolute energy of the cell (relaxed on one side), $E_{slab}^{unrelaxed}$ is the absolute energy of the unrelaxed cell, n is the number of stoichiometric units in the surface cell, E_{bulk} is the energy of a bulk $FeNi_2S_4$ formula unit and A is the surface area of one side of the slab. This stabilisation of the surface energy can also be expressed as a percentage via equation 4.3, which indicates the extent of surface energy change, and is a measure of how much the geometry may have been altered after relaxation. Surface energies and relaxation percentages for the different surface terminations are shown in Table 4.1.

For the (001), prior to relaxation, the sixth termination is the lowest in energy, where the Fe_B cations are located just below the uppermost sulphur layer. However, upon relaxation, we find that the second termination (with Ni_B located just beneath the surface) becomes the most stable plane, having undergone the greatest percentage change in surface energy. For the (011) surfaces, the second termination is energetically the most stable both before and after relaxation, and we can see that it undergoes the smallest change through the relaxation process (12%). In this termination of the (011) surface, both Fe_B and Ni_A cations are located just below the uppermost surface layer. For the (111) surface, both terminations possess Fe_B and Ni_B cations at the top, but relaxation of the second termination is accompanied by noticeable migration of the cations, leading to a bigger reduction in energy. Prior to relaxation, the (111) surfaces are lower in energy than the (001), and as we can see in Table 4.1, these are accompanied by the smallest overall percentage change in energy. Overall, it is the second termination of the (001) surface that is the most energetically stable out of all

the surfaces. For the remainder of this paper, we will focus on the most energetically stable termination of each surface, which are shown in Figure 4.3, as seen from the top and side.

Table 4.1: Surface energies calculated before and after optimisation, for each of the terminations of the (001), (011) and (111) $FeNi_2S_4$ surfaces.

	Termination	γ-unrelaxed (J m^{-2})	γ-relaxed (J m^{-2})	Relaxation (%)
(001)	1	2.88	0.35	88.0
	2	2.55	0.24	88.9
	3	3.33	0.53	84.0
	4	2.88	0.48	83.3
	5	3.34	0.96	71.2
	6	2.41	2.10	13.1
(011)	1	2.57	1.50	41.8
	2	1.61	1.42	12.0
(111)	1	1.57	1.36	13.5
	2	2.07	1.26	39.1

No appreciable changes are observed in the average charges of the respective ions (see Table 4.2), or in the average bond distances upon relaxation (see Table 4.3) when compared to the bulk (Δ_{bulk}). In the (001), if we look at the changes in bond distance before and after relaxation (Δ_{relax}), we see that the biggest change occurs for the Ni_B-S distance, which decreases by almost -0.1 Å. These nickel ions form the topmost layer of cations for this termination of the surface, and we thus see that relaxation causes these ions to migrate further into the bulk. Conversely, analysis of the bond distances for the sixth termination of this surface (which was the most stable prior to relaxation), revealed that although a decrease in the Ni_B-S distance is also observed, it is to a much lesser extent (-0.006 Å). Instead we observe a greater increase in the length of the Ni_A-S and Fe_B-S bonds, implying that these cations move away from their bulk positions. In the (011) and (111) surfaces, we can see that the relaxation process is associated with a decrease in the length of the Ni_A-S bonds only, which is more pronounced in the (011) surface.

We then moved on to study each of the surfaces with water, to see what effect

hydration might have on the surface energies. Were water to have a stabilising effect, similar to that of capping agents, then the probability might increase of one of the surfaces other than the (001) appearing in the morphology under aqueous conditions.

Table 4.2: Average charge (q) and variance with respect to the bulk (Δq) for the different atoms in the bulk, and the (001), (011) and (111) $FeNi_2S_4$ surface cells.

	Fe_B		Ni_B		Ni_A		S	
	q /e	Δq /e	q /e	Δq /e	q /e	Δq /e	q /e	Δq /e
Bulk	1.2		0.6		0.7		-0.6	
(001)	1.1	0.1	0.7	-0.1	0.7	0.0	-0.6	0.0
(011)	1.0	0.2	0.7	-0.1	0.6	0.1	-0.6	0.0
(111)	1.0	0.2	0.7	-0.1	0.6	0.1	-0.5	-0.1

Table 4.3: Average bond distances (d, in Å) after the slab optimisation of the (001), (011) and (111) surfaces, and the relative bond distances compared to the bulk (Δ_{bulk}), and before and after relaxation (Δ_{relax}) of each surface.

	(001)			(011)			(111)		
	d	Δ_{bulk}	Δ_{relax}	d	Δ_{bulk}	Δ_{relax}	d	Δ_{bulk}	Δ_{relax}
Fe_B-S	2.31	0.03	0.02	2.26	0.01	0.05	2.28	0.00	0.00
Ni_B-S	2.20	0.08	-0.1	2.15	0.05	0.04	2.27	0.08	0.07
Ni_A-S	2.14	0.04	0.03	2.09	0.09	-1.00	2.15	-0.01	-0.02

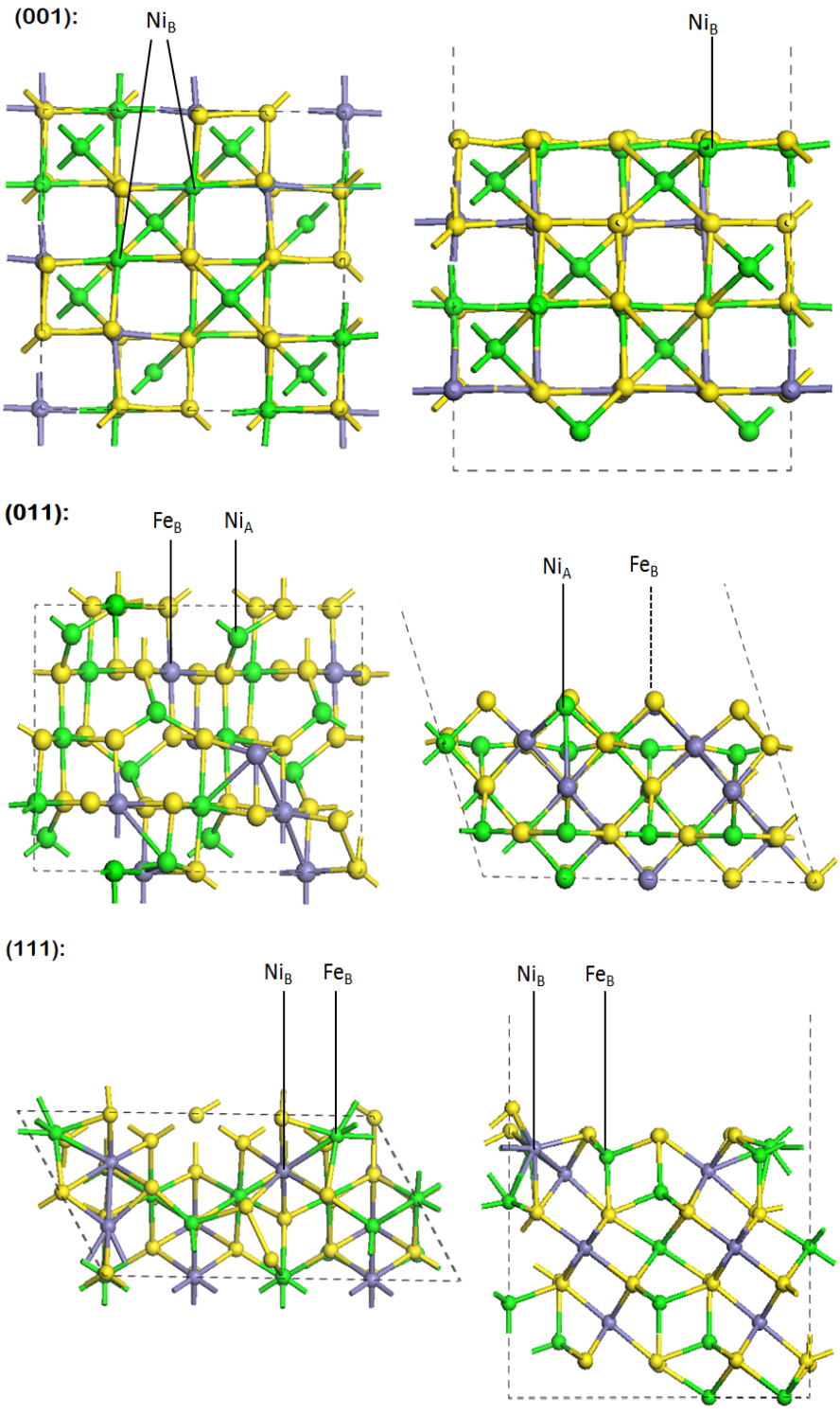

Figure 4.3: Top and side views of the most stable terminations of the (001), (011) and (111) surfaces, from left to right respectively.The yellow atoms correspond to S, the green to Ni, and the purple to Fe.

4.4 H_2O Adsorption and Dissociation on Violarite Surfaces

Two main pathways to the adsorption and dissociation of water on violarite's surfaces were considered, as depicted in Figure 4.4. With regards to the figure, each number relates to a different configuration in the pathway; E_{ads} is the adsorption energy, E_a is the activation energy, and E_R is the reaction energy corresponding to a particular process in the pathway.

To determine the preferred site of adsorption, we considered a number of different configurations, with the water molecule approaching the surface at different angles and locations, followed by the adsorption of a second water molecule in the vicinity of the first. To determine whether or not successful adsorption had occurred, we calculated the energy of adsorption (E_{ads}) using equation 4.4. Any configuration with a small E_{ads}, no significant distortion of the molecule and no charge transfer, was considered to be physisorbed rather than chemisorbed. Table 4.4 contains a summary of the intramolecular distances and angles in the H_2O molecules adsorbed on the different surfaces.

$$E_{ads} = E_{slab+\mathrm{H_2O}} - (E_{slab} + E_{\mathrm{H_2O}}) \tag{4.4}$$

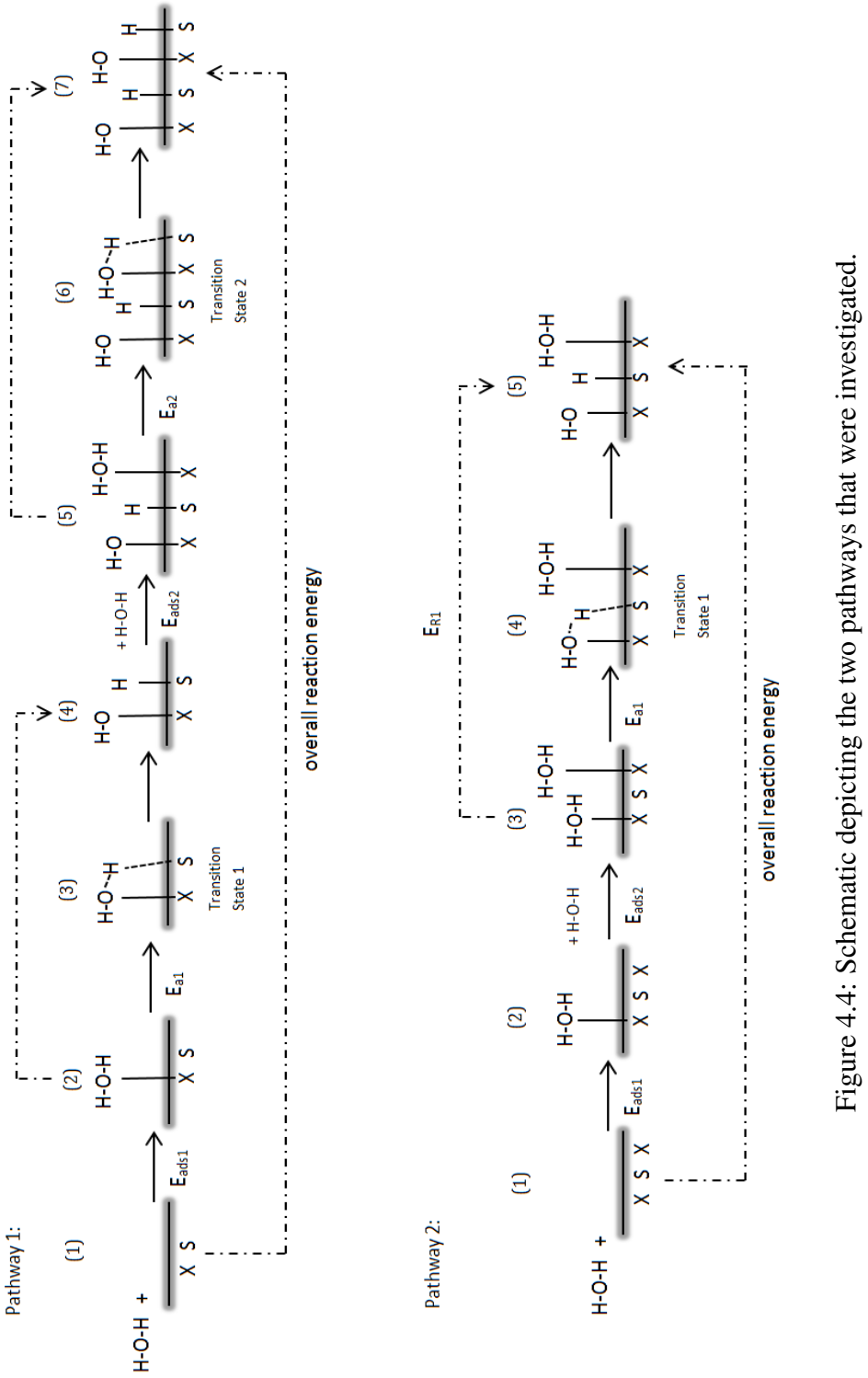

Figure 4.4: Schematic depicting the two pathways that were investigated.

Table 4.4: Calculated average bond distances and angles for the dissociated H_2O through Pathway 1 on the (001) and (011) $NiFe_2S_4$ surfaces.

(001)		Species	M	d(O–M) / d(H–S^{2-}) /Å	d(H_1–O) /Å	d(H_2–O) /Å	H–$\hat{O}$–H (/°)
1st H_2O	associated	H_2O–M^+	Ni_B	2.32	0.98	0.98	105.2
	dissociated	HO–M^+	Ni_B	1.90		0.98	
		H–S^{2-}		1.36			
2nd H_2O	associated	H_2O–M^+	Ni_B	2.14	0.97	1.05	107.2
	dissociated	HO–M^+	Ni_B	1.88		0.99	
		H–S^{2-}		1.36			
(011)		Species	M	d(O–M) / d(H–S^{2-}) Å	d(H_1–O) Å	d(H_2–O) Å	H–$\hat{O}$–H (°)
1st H_2O	associated	H_2O–M^+	Fe_B	2.14	0.98	0.98	105.2
	dissociated	HO–M^+	Fe_B	1.82		0.97	
		H–S^{2-}		1.37			
2nd H_2O	associated	H_2O–M^+	Ni_A	2.27	0.98	1.05	104.7
	dissociated	HO–M^+	Ni_A	1.89		0.97	
		H–S^{2-}		1.36			

4.4.1 $FeNi_2S_4$(001) Surface

Adsorption of H_2O on the $FeNi_2S_4$(001) surface is only likely to occur at one of the Ni_B sites, as these are the sole species in the uppermost cationic layer. We found that water would adsorb onto this site with an energy of -0.33 eV, i.e. sufficiently exothermic to suggest that adsorption on this surface is likely to occur. The molecule is absorbed in such a manner that the O–Ni bond is parallel to the *c*-axis, at a distance of 2.32 Å from the surface, and the two hydrogens orientate themselves such that they are now aligned with two of the sulphurs bound to the Ni (see Figure 4.5). A Bader analysis of the charges reveals a small electron density transfer (i.e. a loss) of 0.1 *e* from the water molecules to Ni_B, an effect that is also noticeable by an increase in H–$\hat{O}$–H bond angle.

4.4.1.0.1 Pathway 1 Figure 4.5 shows the reaction profile for H_2O adsorption and dissociation on the $FeNi_2S_4$(001) surface, and each configuration has been numbered in accordance with the relevant stage depicted in Figure 4.4. If we split one of the molecule's O–H bonds such that the H now adsorbs to one of the sulphurs adjacent to the metallic site of adsorption, we see that the process is endothermic, with a value of 1.16 eV for E_{R1}, as well as a significant activation energy, E_{a1} = 1.28 eV. If we look at the diagram depicting the first dissociated state, we can see that the H is now almost perfectly aligned with the S along the *c*-axis (vertical), bound to the sulphur at a distance of 1.36 Å, and 2.41 Å from the original O.

At this point we also attempted to remove the second H from the OH, and see if this would bind to the same S generating -SH_2 as a starting point of surface oxidation, but, as was perhaps to be expected, this process is highly energetically unfavourable and the end configuration unstable, as the -OH group is far more stable than the lone O group.

We then proceeded to adsorb a second molecule of water to the surface, within close proximity of the first one, where there were two possible Ni_B adsorption sites.

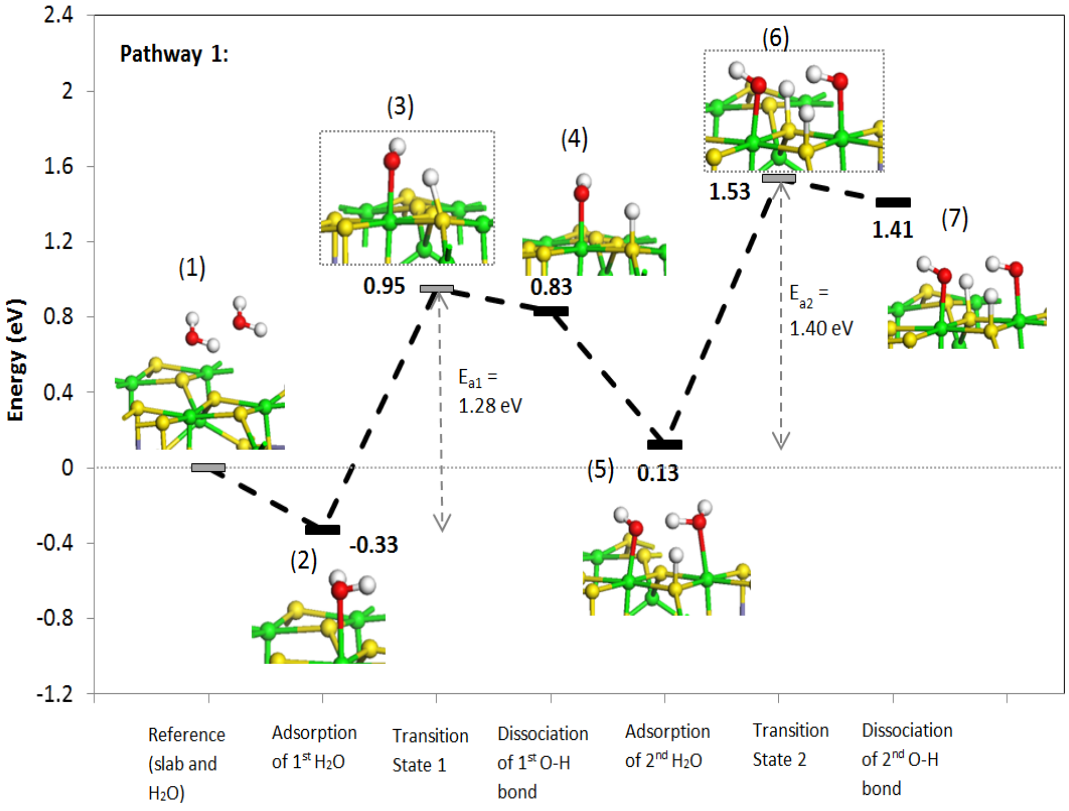

Figure 4.5: (001) Pathway 1 - reaction profile for water dissociation on the $FeNi_2S_4$(001) surface. Inset, schematic representation of the steady states, yellow atoms represent S and green for Ni. Note the transition states are framed.

After performing adsorption calculations on both sites, we took the configuration with the lowest overall energy to be the most stable and thus most likely to occur. The second H_2O then binds at a distance of 2.14 Å, shorter that the first H_2O interaction, but longer than the HO–Ni bond of 1.97 Å.

It is interesting to note that E_{ads2} is 0.46 eV higher than E_{ads1} and positive, with respect to the original reference system, which implies that adsorption of a second water molecule is not as favourable as that of the first, thereby destabilising the system. However, if we look at the adsorption energy with respect to the previous reaction step, i.e. that of the surface with the dissociatively adsorbed water, we obtain a negative value of -0.70 eV. This would imply that once the first water molecule has dissociated, adsorption of the second molecule stabilises the entire system and

reduces the overall energy, which could be explained via analysis of the bond distances. In respect of the second water molecule, if we look at the two O–H bonds, whilst one has a value of 0.97 Å, typical for a water molecule, the other O–H bond is longer at 1.05 Å. Visualisation of the system shows that this H is perfectly aligned between the two oxygen centres, with the HO–H - - - OH distance at 1.53 Å. This not only shows the existence of a strong hydrogen-bond between the two, but the small bond distance suggests that it may be significantly covalent in character and thus could explain the stabilising effect of the second water, through electron-density donation to the OH group.

Insight into local charge rearrangement within the H_2O/surface system can be gained further from the electron density difference obtained by subtracting from the charge density of the total adsorbate system, the sum of the charge densities of the molecule and the clean surface, calculated using the same geometry as the adsorbate system. We then noted a gain in density between the two oxygen centres and nickel ions on the surface, as well as between the dissociated proton and sulphur. We also see a small amount of electron density between the hydrogen on the second water, with the oxygen of the OH group, indicative of the hydrogen-bonded interaction between the two.

The covalent nature of this HO–H - - - OH bond implies that when it comes to breaking one of the O–H bonds in the second water molecule, the more favourable bond to break would be the one not involved in this hydrogen-bond, and this is in fact what was discovered, as a lower energy was obtained for the dissociation of the bond not participating in the hydrogen-bond. Dissociation of the O–H bond in the second water molecule sees the H now bind to a different sulphur (leading to two OH and two SH groups), but one that coordinates both of the nickel ions to which the OH groups are bound. The activation energy required for this second dissociation is higher by 0.12 eV than that of the first, as is E_{R2} (1.28 eV) when compared to E_{R1} (1.16 eV), which tells us that this process is even less likely to occur kinetically

and thermodynamically. The H-bond still exists between the two O centres, but the H-bond length has now increased to 2.05 Å, implying that loss of its proton means the second O is less willing to share its only remaining H. This second OH group is bound to the surface at a distance of 1.88 Å, similar to the first group (which position does not change).

Bader charge analysis reveals that the difference in charge density for the sulphur ions before and after dissociation is Δq = -0.2 e, while for both protons it is Δq = 0.9 e, suggesting that there has been a transfer of electron density from the sulphur ions to the protons. Thus dissociation of both adsorbed waters is accompanied by an increase in the nucleophilicity of both S sites, as e charge is transferred to the protons, which now gain electrons and see a decrease in their charge, which is interpreted as a S–H covalent bond formation.

4.4.1.0.2 Pathway 2 We next investigated the adsorption and dissociation of water in accordance with Pathway 2, as shown in Figure 4.6. The adsorption of a second molecule of water directly after the first results in a decrease in energy of -0.57 eV with respect to the previous system, suggesting that co-adsorption of the second water molecule is energetically more favourable. However, visualisation of the system reveals that the second water does not adsorb closely to the surface but instead interacts weakly from above, with an O - - - Ni distance of 3.35 Å and H - - - S distance of 2.56 Å, suggesting an important stabilising effect of the surrounding water environment. The second water molecule is orientated in such a manner that its oxygen forms a H-bond with one of the hydrogens from the first adsorbed molecule, with a distance between the two of only 1.72 Å, indicating a strong interaction. Dissociation of the O–H bond now causes the second water to migrate closer to the surface so that it becomes chemisorbed to the second Ni centre. Although the dissociation of this bond gives a relatively small endothermic value of 0.13 eV for the overall reaction energy,

E_{R1} (with respect to configuration (3)) is 1.03 eV, and the activation energy (E_{a1}) is a significantly large value of 1.51 eV, comparable to the value for E_{a2} calculated in Pathway 1.

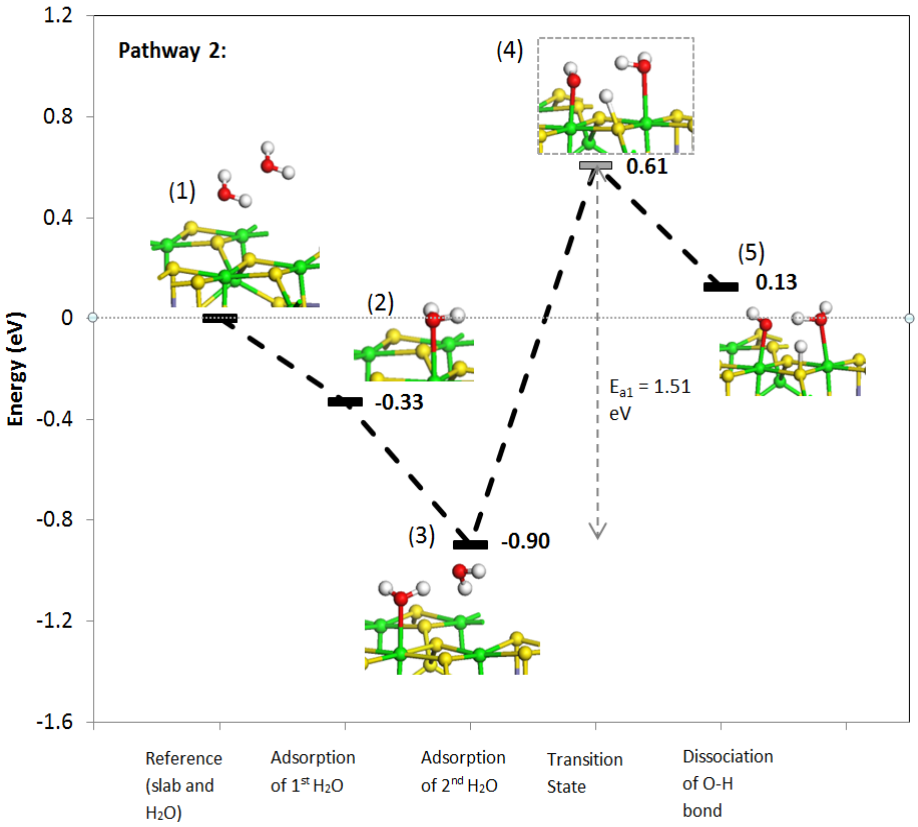

Figure 4.6: (001) Pathway 2 - reaction profile for water dissociation on the $FeNi_2S_4$(001) surface. Inset, schematic representation of the steady states, yellow atoms represent S and green for Ni. Note the transition states are framed.

If we compare the two pathways, we can see that Pathway 2 is energetically the more viable option. If we consider the step following the adsorption of the first water molecule, then progression along Pathway 2 will be accompanied by a decrease in energy, whilst progression along Pathway 1 requires an initial and substantial input of energy. Whilst dissociation is unlikely to occur via either pathway (due to the large values of E_a associated with the dissociation), Pathway 2 would again still be the more probable outcome, due to the less endothermic value of E_R, where our results suggest that if more water molecules are in contact with the surface from the solvent, then

these may further stabilise the intermediates.

As mentioned with regards to Pathway 1, dissociation of the first water and subsequent binding to a S seems to activate the second Ni centre, causing it to bind the second water. Thus, the reaction coordinate in this instance appears to be the H–S distance. As this gets smaller (Δd = -1.73 Å), so does the second O–Ni distance (Δd = -1.21 Å). This effect is explained in terms of electron donation, whereby binding of the H to the S sees the S donate electron density to the second Ni, making it more reactive. Calculation of the respective charges shows that adsorption of the second water sees the charge on the adjacent S become slightly more nucleophilic, a trend which continues as the first water dissociates and the S now binds the free proton, transferring 0.3 e^- to it. The formation of the OH group also sees a further loss in electron density from both of the Ni sites (a combined Δq total of 0.3 e^-), as this newly-formed OH group is even more electronegative.

4.4.2 $FeNi_2S_4$(011) Surface

4.4.2.0.3 Pathway 1 Figure 4.7 shows the reaction profile for H_2O adsorption and dissociation on the (011) surface. On this surface, two different adsorption sites are possible: at a Fe_B or Ni_A site. Tests revealed that adsorption at one of the Fe_B sites was preferable, yielding an adsorption energy of -0.97 eV, significantly lower than the value obtained when the water was bound at one of the Ni_A sites (by around -0.37 eV). In addition, the molecule-metal (H_2O–M) bond distance is shorter when the water is bound to Fe. The adsorption of water stabilises the (011) surface by reducing its surface energy, thereby increasing the probability of this surface occurring in an aqueous environment. The value of E_{ads} is more negative than the ones obtained for the (001) surface, i.e. adsorption is preferable on the (011) surface as this surface has exposed low-coordinated Fe sites. It is also interesting to note that across the two surfaces, the H_2O–M bond lengths are shorter for M = iron rather than M = nickel, being related to the relative stability of the different oxidation states of the metals. At

the Fe_B site, the water aligns itself such that its hydrogens are positioned as close as possible to the adjacent sulphurs, and the oxygen is bound at an angle of 94° and not in line with the *c*-axis, though almost perfectly aligned with the iron along its *c*-axis. Bader charge analysis reveals a charge transfer of 0.2 *e* from the Fe to the water.

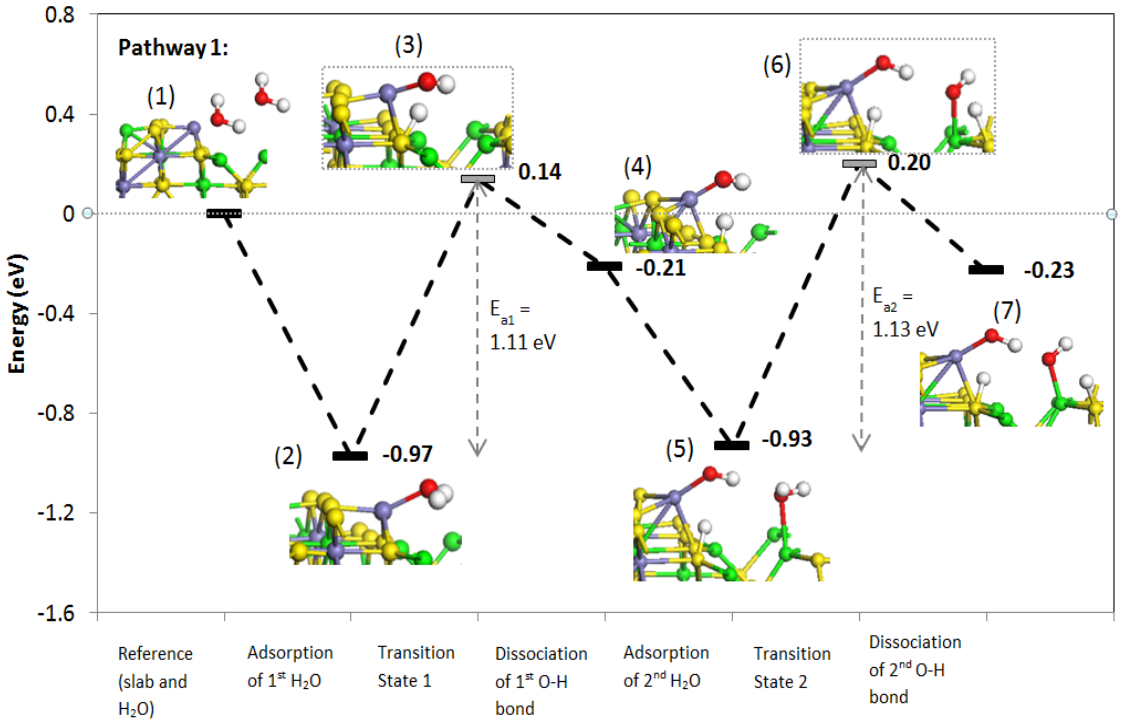

Figure 4.7: (011) Pathway 1 - reaction profile for water dissociation on the $FeNi_2S_4$(011) surface. Inset, schematic representation of the steady states, yellow atoms represent S, green for Ni and purple for Fe. Note the transition states are framed.

We can see that the energy of the transition state for the initial splitting of the first O–H bond (with respect to the initial state) is relatively small at 0.14 eV. However, the value for E_{a1} is much greater at 1.11 eV and we also obtain a value of 0.76 eV for E_{R1}, which is to be expected as the system with the adsorbed water molecule is significantly more stable than that of the pure slab. Nevertheless, the energy of configuration (4) is -0.21 eV, meaning that the process is exothermic with respect to the pure reference system and thus thermodynamically more likely to occur than on

the (001) surface. The H lays aligned with the sulphur along the *c*-axis, and bound at a distance of 1.37 Å (very similar to the value of 1.35 Å for H–S bonds in pure H_2S).

We then proceeded to adsorb a second molecule of water onto this surface, within the vicinity of the first adsorption, where the main adsorption sites this time were tetrahedral Ni_A sites. Adsorption on one of these sites releases -0.72 eV, suggesting that adsorption of a second water is almost as energetically favourable as that of the first. What is more interesting to note is that when the first water molecule is adsorbed onto this same kind of Ni_A site, we obtained a value of -0.61 eV, meaning that adsorption on this site becomes more energetically favourable since the adsorption and subsequent dissociation of the first H_2O on the Fe_B site. This cooperative adsorption is due to the existence of a hydrogen bond between the OH and the H_2O, where the remaining proton on the original O has now aligned itself with the oxygen of the second water, i.e. the OH group is the H-bond donor, and the H_2O is the hydrogen-bond acceptor (with a distance of 2.10 Å). The O-Ni distance is also 2.27 Å, which although longer than the O–Fe distance, is similar to the Ni–O bond distances obtained for the (001) surface.

Dissociation of the OH bond in this second water molecule sees the H migrate and bind to a separate S site. E_{a2} is slightly higher in value than E_{a1}, again an indication that the process will not occur spontaneously. However, it is interesting to note that E_{R2} is slightly lower in value (0.70 eV) than E_{R1} (0.76 eV), meaning that the dissociation of the second water becomes slightly more thermodynamically favourable once a water has already been adsorbed and dissociated. The Fe–OH bond distance has decreased by Δd = 0.07 Å, and the H-bond between the oxygen centres has also decreased to 1.52 Å, suggesting that dissociation of the second water has led to an increase in bond strengths and a more stable structure overall.

Bader charge analysis shows that there is an even greater amount of charge transfer accompanying dissociation on this surface than on the (001). The difference in charge density for the sulphur ions before and after dissociation is as much as Δq =

1.3 e, indicating that these ions have become more positive, whilst for both hydrogens it is Δq = -0.9 e, signifying an increase in negativity, thus revealing a substantial change in the electron density of the respective ions when compared to their pure states.

4.4.2.0.4 Pathway 2 For the (011) surface, adsorption of a second H_2O directly after the first releases a further -0.86 eV in energy, and the molecule again hovers above the surface (see Figure 4.8). The water molecule is orientated with one of its H's aligned with the surface S underneath at a distance of 2.98 Å, and the O with a surface Ni at a distance of 3.07 Å. It is also positioned in such a way that its O interacts with one of the hydrogen atoms of the first H_2O, at a distance of 1.6 Å, suggesting a strong H-bond between the two molecules.

In contrast to the (001) surface, the energies of the transition state and final dissociated state are both negative with respect to the original reference state, suggesting that the process is more feasible on this surface than on the (001), and thus more likely to occur. The overall reaction energy is -0.93 eV, considerably exothermic, and this, in addition to the negative values obtained for E_{ads2} and configuration (4), is again suggestive of the important effect of surrounding water molecules to stabilise the intermediate and product dipole. Yet, if we look at the activation energy, we again obtain a relatively high value of 1.27 eV, as well as 0.90 eV for E_{R1}, indicating that as with the (001), the dissociation of water is unlikely to occur spontaneously. As with the (001), progression along Pathway 2 is accompanied by a greater decrease in energy than for Pathway 1, highlighting that this would be the preferred and most likely route.

The H–S distance again appears to be the reaction coordinate. The dissociation of the O–H bond in the first water and adsorption of the proton by a sulphur is what appears to "activate" the Ni centre so that it now strongly adsorbs the second H_2O. The initial H–S distance is 2.96 Å, but after dissociation of the first H_2O, this has

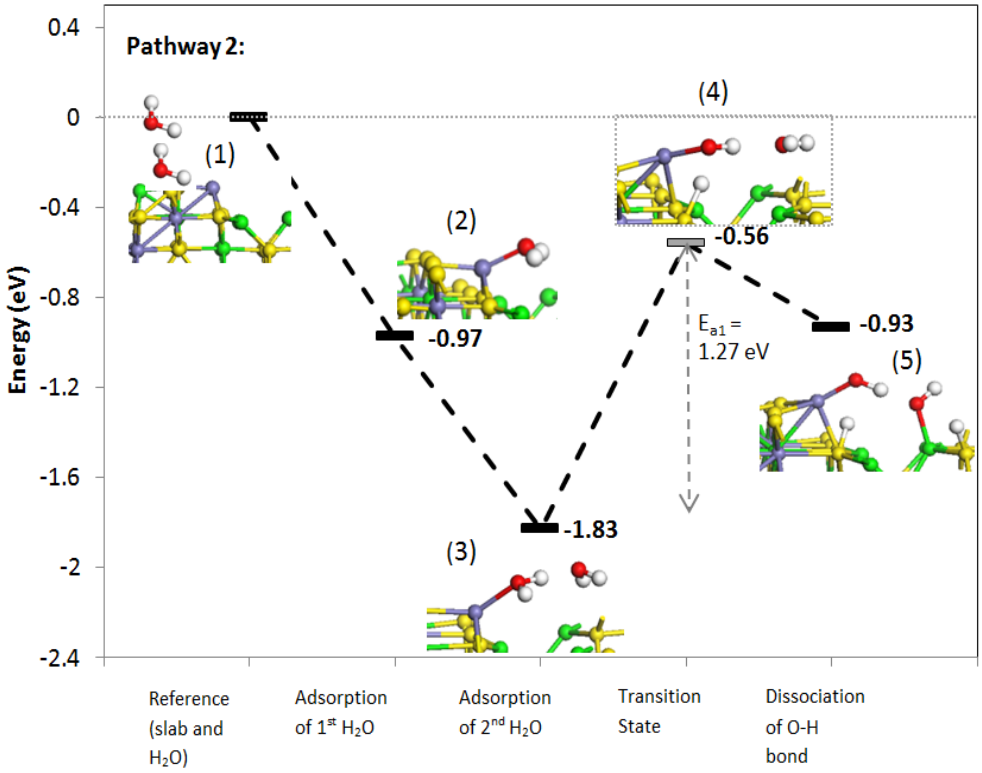

Figure 4.8: (011) Pathway 2 - reaction profile for water dissociation on the $FeNi_2S_4$(011) surface. Inset, schematic representation of the steady states, yellow atoms represent S, green for Ni and purple for Fe. Note the transition states are framed.

decreased to 1.36 Å as the S binds the H. Simultaneously, the O–Ni distance shrinks from 3.07 Å to 2.27 Å, reflecting adsorption of this water molecule on the surface. Calculation of the respective charges show that adsorption of the second water is again accompanied by an decrease in the nucleophilicity of the H-binding sulphur, with an increase in charge of Δq = 0.4 e^-, meaning it has become more positive and lost electron density, which has instead been transferred to the proton. A similar transfer occurs on the Fe sites, as electron density (0.1 e) is now transferred to the more electronegative OH group.

4.4.3 $FeNi_2S_4$(111) Surface

As to the (111) surface, no chemisorption of water occurred at any of the Fe_B, Ni_B or S sites on the surface. Instead, what we found was that the water would interact with the surface with a calculated adsorption energy in the most favourable configuration of only -0.18 eV, and the O coordinated at a distance of 3.59 Å from the nearest Ni centre, and distances of 2.7 Å between the hydrogens and surface sulphurs, indicative of very weak interaction only.

4.5 Morphology

The morphology of a $FeNi_2S_4$ particle in vacuum and in the presence of two waters was constructed using Wulff's method [Wulff, 1901], which is based on the calculated surface energies. Figure 4.9 shows the morphology obtained under thermodynamic equilibrium conditions in vacuum; however, the same result was also obtained in the presence of two water molecules, where due to the relative surface energies between the lowest energy surface (001) and the other two surfaces, this surface would be expressed exclusively under both conditions (not taking into account effects from pressure, temperature or capping agents), as shown in Figure 4.9. We then calculated the linear relationship between the surface energy and the number of water molecules interacting with each surface. The (001) surface energy remains practically constant and appears to be independent from the effect of the interacting molecules; the (011) follows a similar trend with a slope of only 0.06. However, the (111) surface experiences a decrease in its energy with the number of adsorbed H_2O molecules, and we approximate this behaviour as a linear trend with equation y = -0.13x + 1.24. This shows that the (111) surface energy would decrease with the amount of water present (at partial pressures) and at a greater rate with increasing water concentration, compared to the other two surfaces. If the surface energy has a linear relationship with respect to the number of water molecules adsorbed, then with approximately eight ad-

sorbed water molecules, the (111) would surpass the (001) as energetically the most stable surface, and could therefore be present on the crystal morphology under such conditions, as reflected by Figure 4.10, which shows the new morphology under these conditions.

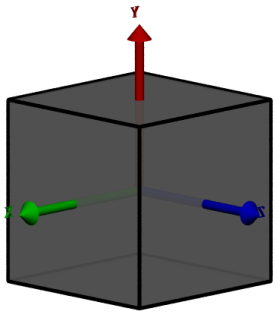

Figure 4.9: Wulff's construction for the equilibrium morphology of a $FeNi_2S_4$ particle, derived from surface energies of pristine slabs, expressing the $\{001\}$ surfaces.

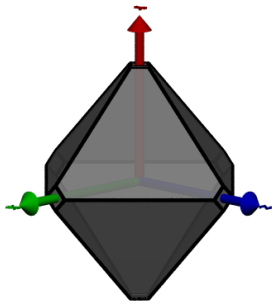

Figure 4.10: Wulff's construction for the morphology of a $FeNi_2S_4$ particle in the presence of eight water molecules, expressing the $\{111\}$ surface predominantly.

4.6 Conclusions

From the geometry optimisation of the low-Miller index surfaces of violarite, we have shown the (001) surface to be the most energetically stable, followed by the (011) and the (111) surfaces respectively. Although the (111) surface is higher in energy, it is the least reactive towards H_2O molecules, as strong interactions will not occur at any of the surface sites. The (011) is the most reactive surface with respect to water adsorption, as perhaps to be expected due to the presence of low-coordinated metal cations, and adsorbed water coordinates to these surface atoms and so stabilises the surface, increasing the likelihood of occurrence under aqueous conditions. Water adsorption is also preferable at a ferrous site on this surface over a Ni_A site, as reflected by the adsorption energy and the shorter O–M distance. Subsequent dissociation of the water molecule to form M–OH and S–H groups on the surface is also most likely to occur on the (011) as the system stabilises, as expressed by a negative value for the overall reaction energy. The adsorption and dissociation of one water molecule seems to have a conducive effect on the adsorption and dissociation of the next; adjacent sites become more reactive and susceptible to adsorption. This synergistic adsorption of water has also been observed on transition metal surfaces (including Ni) by Michel et al. [Michel et al., 2012]. A consecutive adsorption and dissociation of H_2O about the low-coordinated M would lead to surface oxidation. Thus, increasing the number of H_2O on the (011) would stabilise the intermediates and should finally hydroxylate the surface and stabilise the metallic centres, an important feature, as these groups bound on the surface could then be used to facilitate other catalysed reaction pathways.

Chapter 5

SIMULATIONS OF THE STRUCTURE, STABILITY AND DYNAMICS OF Fe^{2+}, Fe^{3+}, S^{2-} AND Fe_xS_y (x,$y \leq 4$) CLUSTERS IN WATER

In this chapter, we present CPMD simulations of the hydrated ions, Fe^{2+}, Fe^{3+}, S^{2-}, as well as that of the following hydrated systems: FeS, FeS_2 Fe_2S_2, Fe_2S_3, Fe_3S_3 and Fe_4S_4. The aim was to investigate the structural and dynamic properties of the hydrated structures, and changes therein with varying composition. Based on these results, additional calculations were performed in order to establish the thermodynamic probability of FeS cluster condensation in an aqueous environment.

5.1 Introduction

A cluster may be defined as a "polynuclear complex...that is small enough to behave as a dissolved species" [Luther and Rickard, 2005]. Clusters in the environment are important as they act as possible building blocks in mineral formation [Luther and

Rickard, 2005, Wolthers et al., 2005]. However, the transformation of these simple dissolved species to solid products is not yet fully understood.

As discussed earlier, the interest in iron sulphide clusters stems not only from the function they play in the active sites of proteins, but also because of the aforementioned interest in Origin of Life theories. This is certainly the case with FeS clusters, with the transformation of solvated species to FeS minerals only partially documented. Berner [1967, 1970] showed that at millimolar concentrations, amorphous FeS (FeS_{amph}) is the first precipitate to form, and that formation of other FeS minerals occurs via this phase e.g. pyrite, greigite and mackinawite. Thus the transformation to other minerals will require a change in spin-state and/or coordination [Theberge and Luther III, 1997].

Simulations of solvated ions and molecules are therefore key to understanding their role in various mechanisms. Some ions will act in solution to modify or maintain electric/osmotic equilibrium, whilst others play pivotal roles in biological processes, constituting important parts of the active sites in enzymes [Rode et al., 2005]. Understanding the properties are vital, as small changes can have a significant effect on the role they play in biological processes. Hence, understanding the dynamics of cluster formation and dissociation, as well as the hydration structure, can bestow useful insights into the chemical reactivity of the compound. It can also help provide information about the reaction rates, as well as the process of nucleation and growth of crystals in solution [Di Tommaso and de Leeuw, 2010, Fulton et al., 2012, Gebauer et al., 2008]. It is often difficult to define the solid FeS phase in the environment, as particulate iron sulphide must be handled in oxygen-free conditions to prevent oxidation, rendering electron microscopic techniques almost redundant [Davison, 1991]. Molecular dynamic simulations are thus particularly useful, as they enable us to investigate the microscopic behaviour of solutions that would otherwise be difficult to observe experimentally [Guardia and Padro, 1990].

We shall discuss further on the results from our CPMD simulations and calcula-

tion of the Gibbs free energies, but lead with an overview of the simulations of these species as reported in the literature.

5.1.1 Investigations of Fe and FeS in Water

MD simulations involving solvated Fe^{2+} and Fe^{3+} ions have been conducted since the early eighties, and are ubiquitous in the literature, providing both structural and dynamical information relating to these ions. They reveal that the coordination number of the first hydration shell for both ferrous and ferric ions is six, and that these are held in an octahedral conformation [Brunschwig et al., 1982, Floris et al., 1992, Guardia and Padro, 1990, Moin et al., 2010, Rode et al., 2004, 2005]. The mean value for the Ow-Fe bond length lies within the range 2.075-2.15 Å for Fe^{2+} (where Ow refers to the oxygen in the water molecule) [Floris et al., 1992, Guardia and Padro, 1990, Moin et al., 2010, Ohtaki and Radnai, 1993, Rode et al., 2004], and 1.95-2.07 Å for Fe^{3+}, [Amira et al., 2005, Floris et al., 1992, Guardia and Padro, 1990, Moin et al., 2010, Ohtaki and Radnai, 1993, Rode et al., 2004]. The values for Fe^{3+}-Ow are expected to be shorter than those for the ferrous ion, as cations with a greater positive charge will exert a greater force of attraction on the surrounding waters, and thus bind them more closely. Characterisation of the second hydration shells have also been conducted. Results have shown that for Fe^{2+}, the number of bound water molecules range between 9-18, though 12/13 are the most commonly reported numbers in the literature [Moin et al., 2010, Rode et al., 2004, 2005], and these are usually coordinated at a distance of 3.75-5.25 Å. Similarly, for Fe^{3+}, the coordination number for the second hydration shell is 11-17, though 13-14 waters are more commonly reported, and these are again held at a slightly shorter distance of 3.5-5 Å. Possible ligand exchange reactions are not found to occur between the first and second hydration shells of these cations, implying that any ligand exchange that does occur between the first and second hydration shells will be so quick that they can be regarded merely as short-lived fluctuations. With regards to the second hydration

shell of Fe^{2+}, the number of exchange processes were found to be (to 1 significant figure) 6 per picosecond (ps^{-1}) from Quantum Mechanical Charge Field Molecular dynamics (QMCF-MD), and 4 ps^{-1} from Quantum Mechanics/Molecular Mechanics Molecular Dynamics (QM/MM MD) with a mean residance time (MRT) of 2.4 or 5.4 ps respectively. Similarly, for Fe^{3+} the respective results from these different theoretical approaches are 4 ps^{-1} and 1 ps^{-1} for the number of exchange events, and 3.1 or 19.8 ps for the MRT [Hofer et al., 2004, Moin et al., 2010]. In both contrasting cases, there are fewer exchange processes for Fe^{3+} than Fe^{2+}, indicating a more stable second hydration shell, as is to be expected from the higher cationic charge. Moin et al. [2010] showed through comparison with experimental results, such as EXAFS, that the QMCF-MD approach yields better results, through treatment of successive hydration shells quantum mechanically, rather than just the ion and one hydration shell, as with QM/MM. This means that all the binding in the first and second shells are now included in the quantum mechanical force calculations, as well as more realistic fluctuating atomic charges of all the species in the QM region.

Whilst there have been several computational studies of Fe_xS_y clusters [Hübner and Sauer, 2002, Nair et al., 2008, Shoji et al., 2005, Torres et al., 2003], these have primarily been concerned with quantum chemistry calculations of the bond nature, electronic structure and magnetic interactions of these clusters in the gas-phase or in a simulated solvation environment. For instance, Torres et al. [2003] performed density functional theory and reduction potential calculations for the various oxidation states of those Fe_4S_4 clusters found in the active sites of Fe-S proteins. However, as their interest was from a purely biological point of view, the modelled structures were $[Fe_4S_4(SCH_3)_4]$ in accordance with those protein-based clusters, rather than the pure iron sulphide cluster.

Hübner and Sauer [2002] investigated the structure and energies of different isomers and electronic states of compounds including $Fe_2S_2^{-/0/+/2+}$ and $FeS_2^{-/0/+/2+}$, employing DFT calculations with the B3LYP functional. For Fe_2S_2, they found that

the lowest energy isomer had a rhombic structure with a respective Fe-Fe distance of 256 pm. They also showed that the orbital occupancies were most likely to be Fe^{2+} (d^6) and S^{2-}. For FeS_2, there were three possible configurations, cyclic, linear and bent. The bent conformation was found to have the lowest energy, followed by the linear and cyclic. (See Figure 5.1).

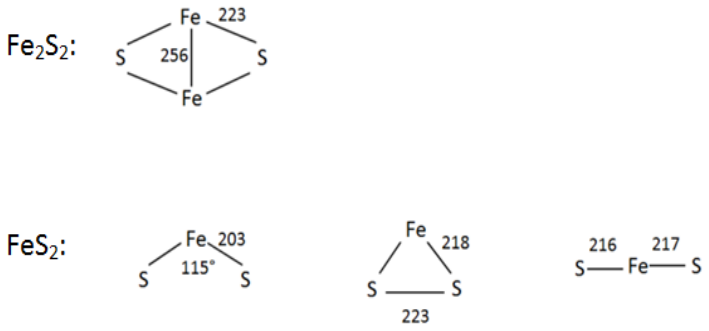

Figure 5.1: Results from Hübner and Sauer's investigation [2002]. Distances are given in pm.

Although there have been some investigations of the solubility of FeS complexes and clusters, these are far from abundant. Davison [1991] provided an in-depth evaluation of literature values for the solubility products of various iron sulphide phases in both fresh water and seawater. He stated that when waters become devoid of oxygen (such as in the Hadean ocean), then ferrous and sulphide ions will become more abundant and approach the solubility product of FeS. Although FeS readily precipitates, it is one of the more soluble metal sulphides, and thus Fe^{2+} and S^{2-} are maintained at measurable levels in the presence of the solid phase.

In seawater, it was found that either greigite or mackinawite would be the controlling phase, but that only 73% of Fe^{2+} ions would exist as this, the rest being complexed by chloride and sulphide ions. In freshwater sediments, it is the aging of the solid phase with depth in the sediment that brings about the conversion of

amorphous FeS to greigite and mackinawite.

Rickard [1995] investigated the competing mechanisms by which FeS may precipitate, from aqueous iron (II) and dissolved sulphide at 25 °C. There were two possible reaction pathways:

1. $Fe^{2+} + H_2S \rightarrow FeS(s) + 2H^+$

2. $Fe^{2+} + 2HS^- \rightarrow Fe(HS)_2(s)$

   $Fe(HS)_2(s) \rightarrow FeS(s) + H_2S$

In both instances, the rates were found to be proportional to $[Fe^{2+}]$. In natural systems, he showed there was a strong dependence on the pH and total dissolved sulphide concentration. In neutral/alkaline environments and those with high concentrations of sulphur, the bisulphide pathway dominates, because in relatively sulphide-rich environments, there is a standing concentration of $Fe(SH)_2$ (a useful intermediate in the formation of compounds such as pyrite). In sulphide-poor and acidic environments, ($pH < 8$), the H_2S pathway involving direct formation of FeS prevails.

Theberge and Luther III [1997] showed the existence of a soluble FeS species in both laboratory and marine systems, but only when the ion activity product (IAP) exceeds the solubility product (K_{sp}) of amorphous FeS. Again, FeS_{amph} is important in understanding the presence of other FeS aqueous species, as it puts an upper boundary on FeS solubility, and the formation of all other iron sulphides must first pass through this phase. On aging, FeS_{amph} transforms to other minerals such as pyrite, greigite and mackinawite (accompanied by changes in geometry and spin). Using voltammetric techniques, Theberge and Luther III [1997] showed that the formation of FeS from Fe^{2+}(aq) is accompanied by a change in geometry, from octahedral to tetrahedral. The geometry change coincides with the formation of amorphous FeS, which itself converts to mackinawite with tetrahedral FeS. The process is thought to be entropy-driven, and loss of water occurs:

$$3Fe(H_2O)_6^{2+} + 3HS^- \rightarrow 3Fe(H_2O)_5(HS)^+ + 3H_2O \quad (5.1)$$

$$3Fe(H_2O)_5(HS)^+ + 3HS^- \rightarrow Fe_3S_3(H_2O)_6 + 3H_2S + 9H_2O$$

Luther and Rickard [2005] have also shown more recently that the first condensed phase to form would be nanoparticulate mackinawite.

5.2 Methodology

5.2.1 CPMD Computational Details

The CPMD simulations were conducted using the Car-Parinello code included in Quantum Espresso package, version 4.2.1 [Giannozzi et al., 2009]. Spin-polarised calculations were performed to describe the electronic structure, using the Perdew-Burke-Ernzerhof (PBE) gradient-corrected functional [Perdew et al., 1996], as this functional gives an accurate description of intermolecular hydrogen-bonding [Rao et al., 2009, Zhao and Truhlar, 2005]. Vanderbilt ultrasoft pseudopotentials (USPP) were utilised to represent core-valence electron interactions [Vanderbilt, 1990]. The USPP for Fe, S, O and H were taken from the standard Quantum Espresso distribution; semicore 3s and 3p functionals were explicitly included in the active space of pseudopotential representations of the Fe^{2+} and Fe^{3+} ions, as it has been shown that this leads to an improvement in the description of the hydration structure of transition metal ions [Fulton et al., 2012]. It was found that by including these functionals, polarisation was better described, leading to an improvement (of around 0.1 Å) in the predicted first-shell bond lengths in the hydration structure, and smaller discrepancies between the experimental XAFS and simulated results. The electronic wavefunctions were expanded in a plane wave (PW) basis set with a kinetic energy cutoff of 30 Ry and 200 Ry for the electron density (as this ensures that convergence of the calculation occurs, as tested in previous investigations [Di Tommaso and de Leeuw, 2008]).

The time-step was set to 0.2 fs and the electronic mass to 600 au. All simulations were carried out in the *NVT* ensemble using the Nosé-Hoover chain thermostat to maintain the average temperature at 400 K, which is necessary to maintain the liquid properties of water [Sit and Marzari, 2005]. The *NVT* ensemble is generally preferred over the *NPT* ensemble, as the convergence of pressure for DFT plane wave MD simulations in the *NPT* ensemble requires a significantly higher basis set cutoff, resulting in a substantial increase in computational time. In addition, the use of the *NVT* ensemble in the simulation of metals gives good agreement with experimental results. For the simulation of charged systems (e.g. Fe^{2+}, Fe^{3+} and S^{2-}), calculations were conducted by including a homogenous neutralising charge density implicitly included in the computational box. In these CPMD simulations, the hydrogen nuclei were treated as classical particles, with the mass of the deuterium isotope, in order to allow for a larger time-step to be used. These parameters were chosen in accordance with the ratio $\mu \leq \frac{1}{3}$ (where μ is the fictitious electronic mass), as suggested by Grossman when investigating the structural properties of aqueous solution [Grossman et al., 2004].

5.2.2 Simulation Protocol

To obtain the initial configurations of each of the solvated species, we would first take the last configuration from a CPMD simulation of 54 or 84 heavy waters molecules in a cubic supercell of side length 11.94 Å and 13.84 Å respectively. We would then substitute the necessary number of D_2O molecules by our FeS structures, by calculation and comparison of the particle radius with that of the solvent radius. Thus, CPMD simulations of Fe^{2+}, Fe^{3+} and S^{2-} were conducted with a single ion embedded in a box of 53 heavy water molecules (with charges and spins fixed in the input file). Simulations were also conducted with a single FeS in a box of 83 waters, FeS_2/Fe_2S_2 species in a box of 82 waters, a Fe_2S_3 in a box of 81 waters, and Fe_3S_3/Fe_4S_4 in a box of 80 waters. We first optimised each of the structures in vacuum using Dmol^3 version 4.2 [Delley, 1990, 2000], which is an all-electron DFT code.

5.2.3 Analysis of MD Simulations

Information to be gleaned from MD simulations include the radial distribution function, the angular distribution function, the coordination numbers, and the mean residence time/number of exchange events between different hydration shells.

- Radial Distribution Function (RDF) $g_{\alpha\beta}(r)$: This gives the probability of finding an atom of type β at a distance r from an atom of type α (relative to the probability expected from a completely random distribution). When plotted, the first peak of the RDF between, say, Fe^{2+} and oxygen, will correspond to the first hydration shell, the second peak to the second hydration shell, and so on; whilst the maxima of the peaks corresponds to the average distance between atoms α and β within that hydration shell.

- Coordination Number (CN): This refers to the coordination number of each hydration shell i.e. how many waters are coordinated by the species of interest in that particular shell. This is obtained by integrating the minimum after the peak in the RDF.

- Angular Distribution Function (ADF): similar to the RDF, but instead tells us the probability of finding an atom of type β coordinated at a certain angle from atom α. So by plotting the ADF, we obtain from the maximum at the first peak the average coordination angle for the waters in the first hydration shell, as for the RDF.

- Mean Residence Time (MRT): The process of exchange can be calculated between the first and second hydration shells using the "direct" method as proposed by Hofer et al. [2004]. In this method, the whole of the simulated MD trajectory is scanned for movements of water molecules, which are either entering or leaving the hydration shell. When a water molecule crosses the boundaries of the shell, its path is followed and if the new position inside/outside the

shell lasts for longer than the time parameter t^*, the event is counted as being "real". The MRT of a water molecule in a hydration shell is then computed by:

$$MRT = \frac{t_{sim} CN_{av}}{N_{ex}} \tag{5.2}$$

where t_{sim} is the simulation time, CN_{av} is the average coordination number, and N_{ex} is the number of exchange events. t^* is set to 0.5 ps as this has previously been shown to be a good measure of ligand exchange processes [Hofer et al., 2004].

5.2.4 Calculation of the Free Energies of Reaction in Solution

The free energy change for the formation of FeS and Fe_2S_2 clusters in water were computed using CPCM as implemented in Gaussian 03 [Frisch et al.], in accordance with the following equation:

$$\Delta G_{aq} = \Delta E_e + \Delta G_{VRT} + \Delta\Delta G_{solv} + \Delta\Delta E_{Q' \to Q} \tag{5.3}$$

where ΔE_e is the gas-phase total electronic energy at 0 K, $\Delta G_{VRT} = \Delta H_{VRT} - T\Delta S_{VRT}$ and is the gas-phase vibrational, rotational and translational contribution to the free energy at a fixed temperature and pressure, $\Delta\Delta G_{solv}$ is the sum of the solvation free energies of the products (P) minus that of the reactants (R):

$$\Delta\Delta G_{solv} = \sum_P \Delta G_{solv}(P) - \sum_R \Delta G_{solv}(R) \tag{5.4}$$

and $\Delta\Delta E_{Q' \to Q}$ represents the energy term due to changes in internal geometry when passing from the gas-phase to solution.

For instance, in order to calculate the electronic contribution (ΔE_e), we would first have to perform single-point calculations on each of the optimised structures, reactants and products, and then subtract the total energy of the reactants from that

of the products. This would be repeated for ΔG_{VRT}, though this time performing frequency calculations on each of the structures, and for $\Delta\Delta G_{solv}$, where we would reoptimise each of the structures, but this time in an aqueous environment to obtain the new energies. (For a more detailed explanation, see Appendix.)

The method used to compute each of these contributions to ΔG_{aq} is based on previous work on the condensation reactions of $CaCO_3$ in solutions which verified its accuracy [Di Tommaso and de Leeuw, 2009], whereas similar methods have been used to estimate the stability of several copper chloride complexes [Sherman, 2007], and to model the aqueous reaction thermochemistry of ferric ions in water [Martin et al., 1998].

The gas-phase calculations were carried out using the mPW1B95 hybrid-meta-DFT method, as this functional has been specifically developed for thermochemistry calculations using the semi-empirical fitting approach, and has proven to be one of the most accurate methods for the calculation of thermodynamic properties [Zhao and Truhlar, 2005, Zhao et al., 2004]. This functional is based on the modified Perdew and Wang exchange functional (mPW) [Perdew et al., 1992] and Becke's correlation functional (B95) [Becke, 1996], and also uses meta-GGA (whereby the GGA functional is also dependent on the kinetic energy density) [Zhao et al., 2004]. The optimisations, frequencies and single-point calculations were then calculated using the 6-31G(d,p) basis set. The temperature was fixed at 298 K and the pressure at 1354 atm, which corresponds to the pressure parameter $p = WRT$ corresponding to the experimental density of liquid water, W= 997.02 kg m^{-3} [Martin et al., 1998]. The solvation free energies, ($\Delta\Delta G_{solv}$), were calculated using the HF/6-31G(d) level of theory, which is recommended for predicting the free energies with the PCM model [Di Tommaso and de Leeuw, 2009] by the Gaussian 03 manual.

To calculate the changes in energy due to the changes in internal geometry when passing from the gas-phase to solution $\Delta\Delta E_{(Q'\rightarrow Q)}$, we first calculated the sum of the deformation energy $\Delta E_{(Q'\rightarrow Q)}$ of the products minus that of the reactants. The de-

formation energy $\Delta E_{(Q' \to Q)}$ is defined as $\Delta E_{(Q' \to Q)} = E_e(\overrightarrow{Q}) - E_e(\overrightarrow{Q'})$, where $E_e(\overrightarrow{Q})$ is the electronic energy of the solute optimised in solution, and $E_e(\overrightarrow{Q'})$ is the electronic energy of the structure of the solute optimised in the gas phase, both at the HF/6-31G(d) level of theory.

5.3 CPMD Simulations of Fe^{2+}, Fe^{3+}, S^{2-} and FeS

In this section we investigate the hydrated structures of the Fe^{2+} and Fe^{3+} cations, and compare these to FeS to see what effect the presence of sulphur has on the hydration structure of iron.

Before beginning our analysis, the Fe-O distances were plotted for both the ferrous and ferric ions with respect to time (total length of the simulation was just over 38 ps). From Figures 5.2 we can see that for Fe^{2+} an exchange process occurs at around 20 ps, where a loosely coordinated water molecule moves into much closer proximity to the cation, and the same is observed for Fe^{3+}, at around 18 ps. We therefore decided to perform all further analysis using only the data from the last 18 ps of the trajectory, as this would have given the system time to equilibrate and stabilise.

Figures 5.3 and 5.4 show the radial distribution functions (RDFs) g(r), and running coordination numbers n(r), for the Fe-O and S-H pairs respectively. The value of $n_{FeO}(r)$ at the first minimum of $g_{FeO}(r)$ will give the coordination number of the first hydration shell i.e. the number of oxygens that are part of the first hydration shell for that particular cation. The relevant data for the first and second hydration shells are summarised in Table 5.1.

Figures 5.3 (a) and (b) shows that there are many similarities between the hydration structures of Fe^{2+} and Fe^{3+}. The clear minimum shown in the Fe-O RDFs between the first and second peaks suggests that the first hydration shell in each is both well-characterised and rigid. The Fe-O coordination distance decreases with increasing charge on the iron (in good agreement with experimental results from X-

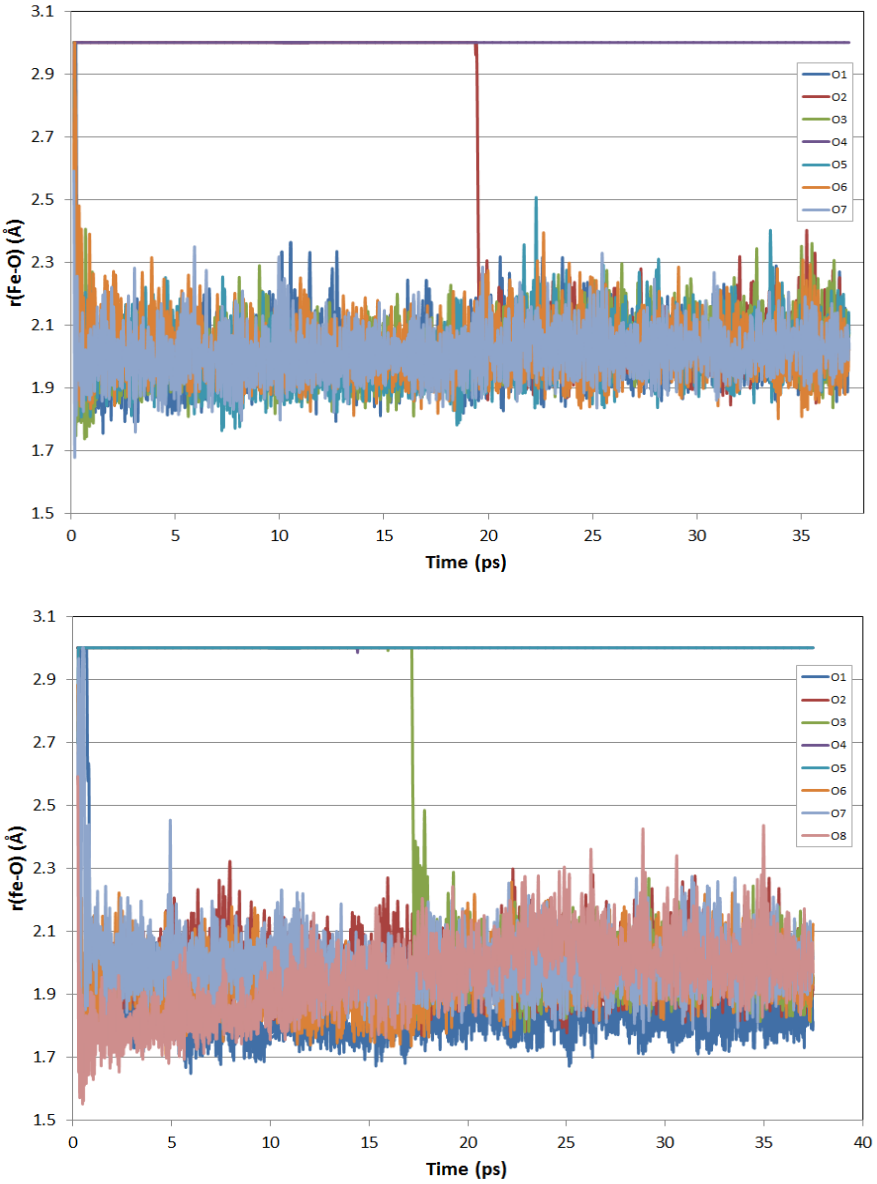

Figure 5.2: Evolving Fe-O distances plotted against time for the Fe^{2+} cation (top) and the Fe^{3+} cation (bottom).

ray and neutron diffraction [Brunschwig et al., 1982, D'Angelo and Benfatto, 2004, Ohtaki and Radnai, 1993]), which is to be expected as Fe^{3+} will exhibit a stronger force of attraction on the water molecules, and thus bind them at a shorter distance. Integration of the minimum after the first peak gives a running coordination number of 5.9 and 6 for Fe^{2+} and Fe^{3+} respectively; showing that in each case, the first hydration shell for a single Fe cation will be composed of six oxygen atoms, as shown

Table 5.1: Positions r_{max}^{FeO} (Å) and amplitudes g_{max}^{FeO} of the maxima of the first and second peaks of the Fe-O radial distribution functions, and average coordination number CN_{av} of the respective shells of the iron ion obtained from the CPMD simulations of Fe^{2+}, Fe^{3+} and FeS in water (* this Fe-O bond is cis to the Fe-S bond).

	r_{max1}^{FeO}	g_{max1}^{FeO}	r_{max2}^{FeO}	g_{max2}^{FeO}	$CN_{av,1}$	$CN_{av,2}$
Fe^{2+}	2.02	19.25	4.275	1.96	5.9	11.9
Fe^{3+}	1.96	16.72	4.0675	2.02	6	12
FeS	1.84*	9.17	3.35	0.60	3	12
	1.93	13.7				
	r_{max1}^{SH}	g_{max1}^{SH}	r_{max2}^{SH}	g_{max2}^{SH}	$CN_{av,1}$	$CN_{av,2}$
S^{2-}	1.36	12.01	3.705	1.46	2	53
FeS	1.36	21.64	2.23	1.22	1	3.33

in Figure 5.5 (a), a representative snapshot of the CPMD simulation, which is also in good agreement with previous theoretical and experimental work [Brunschwig et al., 1982, Floris et al., 1992, Guardia and Padro, 1990, Moin et al., 2010, Rode et al., 2004, 2005].

As far as the g(r) for Fe^{3+} is concerned, the value of 1.96 *Å* (from the maximum of the first peak of the Fe-O RDF) fits within the range of 1.98-2.05 Å obtained from experimental data, as summarised by Amira et al. [2005], yet it is definitely at the short end of the scale. Our value is also very close, though again smaller, to the value (1.99 Å) obtained in a recent study comparing XAFS experimental data and *ab initio* MD data [Fulton et al., 2012] to good agreement. While the n(r) correctly predicts a value of six oxygens to constitute the first hydration shell, visualisation of the hydrated cation reveals that out of these six assumed water molecules, one of the oxygens in fact belongs to a hydroxyl group, having been deprotonated (see Figure 5.5 (b)). This would explain why we obtain a slightly shorter value for the average g(r), as Fe-OH bonds are typically shorter [Ensing, 2003]. This behaviour does not occur in our simulation of Fe(II), which we have observed to coordinate a total of six waters in the first hydration shell (Figure 5.5 (a)). The loss of this proton sees the formation of a H_3O^+ species, which, as observed from our simulation, lies

well beyond the second hydration shell of the iron. In order to ascertain whether the deprotonation of the water molecule occurred as a result of the temperature at which we ran our simulation (400 K), the experiment was repeated at temperatures of 300 K and 350 K, but the deprotonation of one H_2O coordinated to Fe^{3+} still occurred.

For the FeS cluster in water, the RDF in Figure 5.3 (c) shows that while the first shell is still well-defined, integration of the first minimum gives a value of three oxygens for the first hydration shell, suggesting that once bound to sulphur, iron is only capable of binding half the number of oxygens compared to those bound by the single cation. The other noticeable difference is the splitting of the first peak. If we take the shorter of the two r(Fe-O) values for the FeS species given in Table 5.1, which refer to the two different maxima of the split peak, then the value of 1.84 Å is comparable to the value reported for Fe-O hydroxo bonds (around 1.86 Å) by Ensing [2003], and from Figure 5.5 (c) we can see that one of the oxygens coordinated to the Fe indeed belongs to a hydroxyl group, while the other two oxygen atoms are those of the water molecules, explaining the differences in intensity of the split peak. Moreover, analysis of the S-H RDF of FeS in water in Figure 5.4 (b) reveals the presence of an intense peak at 1.36 Å, which corresponds to an intra-molecular S-H bond (see Table 5.1). Therefore, our CPMD simulations indicate that the FeS pair in solution exists as $Fe(SH)(OH)(H_2O)_2$. Verification of the charges via Natural Population Analysis revealed that the constituent ions in $Fe(SH)(OH)(H_2O)_2$ exist as Fe^{2+} and S^{2-}.

The O-Fe-O angular distribution functions (ADFs) of the water molecules that are part of the first hydration shell of the metal in Figure 5.6 show that irrespective of sulphur, the oxygens bound to the iron ions will be coordinated at angles of 90° and 180°. The coordination environment of $Fe^{2+}(H_2O)_6$ and $Fe^{3+}(H_2O)_5)(OH)$ is therefore octahedral, and that of $OH(H_2O)_2Fe(SH)$ is planar tetragonal (see Fig. 5.5), which confirms what was suggested in an earlier voltammetric study of FeS species in natural environments and laboratory solutions [Theberge and Luther III, 1997]. The

effect of the S ligand is therefore to significantly reduce the coordination size of Fe.

For the second hydration shell of Fe^{2+} and Fe^{3+}, we refer to the second peak in their RDFs, which is noticeably broader in both instances, albeit slightly better defined for Fe^{3+} (see Figures 5.3.(a) and (b)). The running coordination number at the second minimum of g_{FeO}(r) indicates that the second solvation shell around the Fe cations contains 12 water molecules. In each case, this second minimum does not reach zero, which implies that ligand migration is occurring between the second hydration shell and the bulk water.

For FeS, the second peak of the Fe-O RDF is not well-defined, presumably due to the presence of sulphur and the effect this has on the ordering of the surrounding waters (see Fig. 5.3 (c)). However, the average coordination number for this second hydration shell is also 12, identical to that of the single Fe cations, suggesting that the effect of sulphur on the hydrated structure of iron becomes less pronounced on the second and further hydration shells.

Figure 5.4 reports the S-H radial distribution, $g_{SH}(r)$, and running coordination number, $n_{SH}(r)$, obtained from the simulation of S^{2-} and FeS in water. For S^{2-}, the intense peak at around 1.4 Å corresponds to an intra-molecular S-H bond, and the value of $n_{SH}(r)$ after the first minimum, $n_{SH}(r)$ = 2, clearly indicates that S^{2-} has been completely protonated, and therefore is present as H_2S. In FeS, S is therefore simply hydrogenated (n_{SH} = 1 at the first minimum).

Figure 5.7 reports the H-S-H ADF between the inter-molecular S-H bonds (i.e., the hydrogen-bonding that occurs between the sulphur and the hydrogens on neighbouring water molecules). For the single H_2S species, the distribution of S-H bonds is much more concentrated at around 90°, suggesting that there is some uniformity in the geometry, and that the hydrogens coordinated to sulphur will be at angles of around 90°. However, when bound to Fe, the rigidity of this geometry is lost, as illustrated by the broader peak.

The MRT and N_{ex} were calculated for each of the species, Fe^{2+}, Fe^{3+}, S^{2-} and

FeS. For Fe^{2+} and Fe^{3+}, in accordance with previous experimental work [Rode et al., 2004, 2005], N_{ex} was equal to 0, implying that no ligand exchange reactions occur between the first hydration shell and the bulk. This was also obtained for FeS. For S^{2-}, N_{ex} = 0.3 ps^{-1}, with a MRT of 66.8 ps. These values, in addition to the lack of any exchange events for the other solvated species, is representative of each of their stabilities in solution.

We have also analysed how the single species affect the number of the hydrogen bonds for the water molecules that are directly coordinated to them (those that make up the first hydration shell), with our values for the average number of hydrogen bonds formed for each species shown in Table 5.2. To extract from our MD simulations the number of hydrogen bonds between two water molecules we have used the following geometrical criteria [Chandra, 2000]: (i) The donor-acceptor Ow-Ow distance is less than 3.5 Å; (ii) the donor-acceptor Hw-Ow distance is less than 2.45 Å; (iii) the hydrogen-donor-acceptor angle is less than 30°.

Table 5.2: Distribution of the number of hydrogen bonds. The values given are percentages of oxygen atoms with the given number of hydrogen bonds. (*Car-Parrinello molecular dynamics simulation of bulk water using PBE functional.)

species	number of hydrogen bonds 0 (%)	1 (%)	2(%)	3(%)	4 (%)	5 (%)	average
Fe^{2+}	0.9	17.0	61.8	20.3	0.0	0.0	2.0
Fe^{3+}	1.4	28.1	54.6	15.8	0.0	0.0	1.8
S^{2-}	4.1	36.4	58.7	0.7	0.0	0.0	1.6
S-Fe-Ow	0.1	12.4	80.0	7.4	0.1	0.0	2.0
Fe-S-Ow	1.8	22.2	71.8	4.1	0.0	0.0	1.8
bulk water (AIMD)*	0	6	24	66	6	0	3.8
Expt. [Soper et al., 1997]							3.6

It should be noted first that each water can take part in a maximum of four hydrogen bonds, although at standard liquid conditions, it has been shown that half of the water molecules will only be involved in three hydrogen bonds [Luzar and Chandler,

1996]. For the Fe ion, from Table 5.2 we can see that when water is coordinated to Fe^{2+}, it can participate in a total of two hydrogen bonds, a higher average than if bound to an Fe^{3+} ion (1.8). For the iron in FeS, the optimum number of hydrogen bonds formed with neighbouring water molecules is also two, which is to be expected as the Fe in this species shares the same charge as the Fe^{2+} cation. As for sulphur, here the average number of hydrogen bonds occurring is smaller for the single anion than when bound to Fe, as was implied from the S-H RDFs in Figure 5.4.

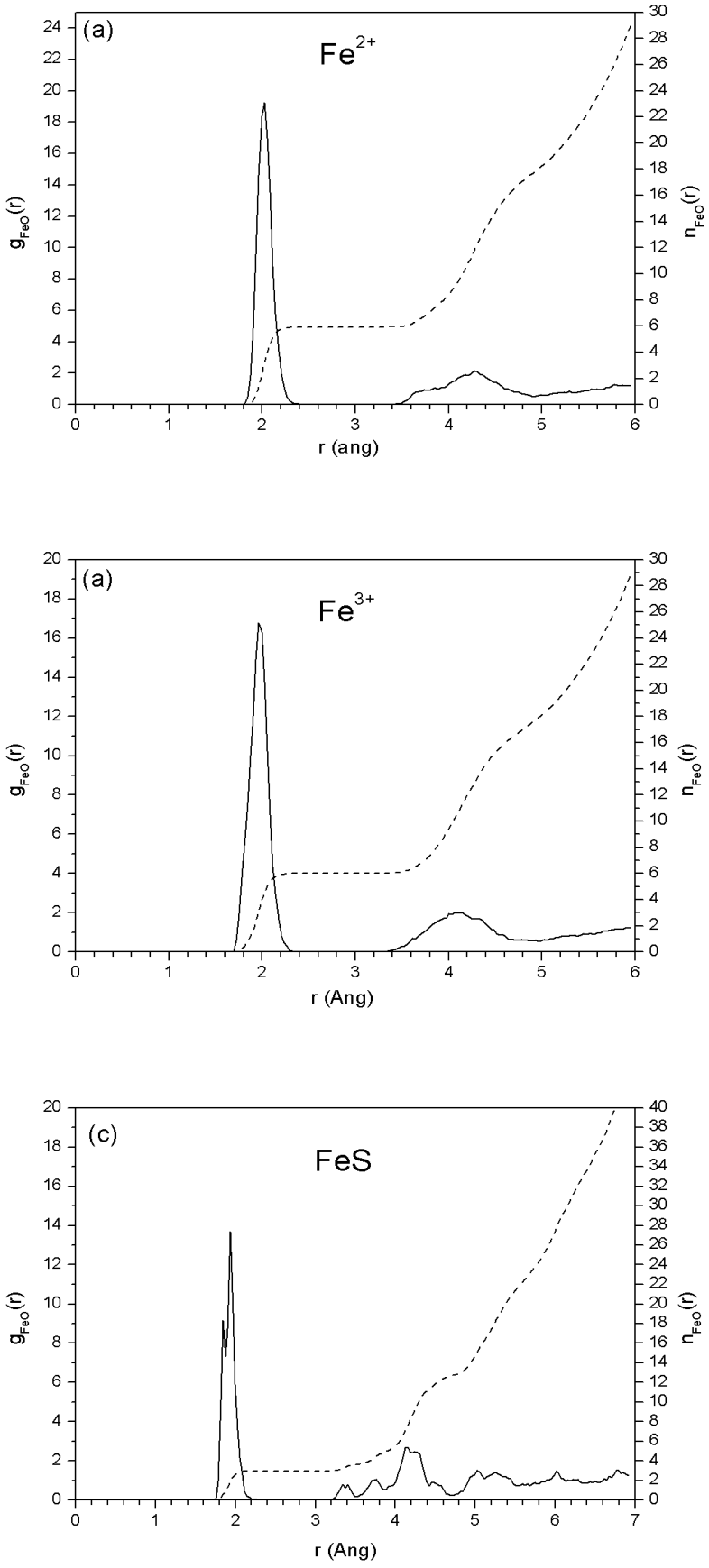

Figure 5.3: (a)-(c) Fe-O radial distribution functions $g(r)$ and running coordination number $n(r)$ for Fe^{2+}, Fe^{3+} and FeS, respectively.

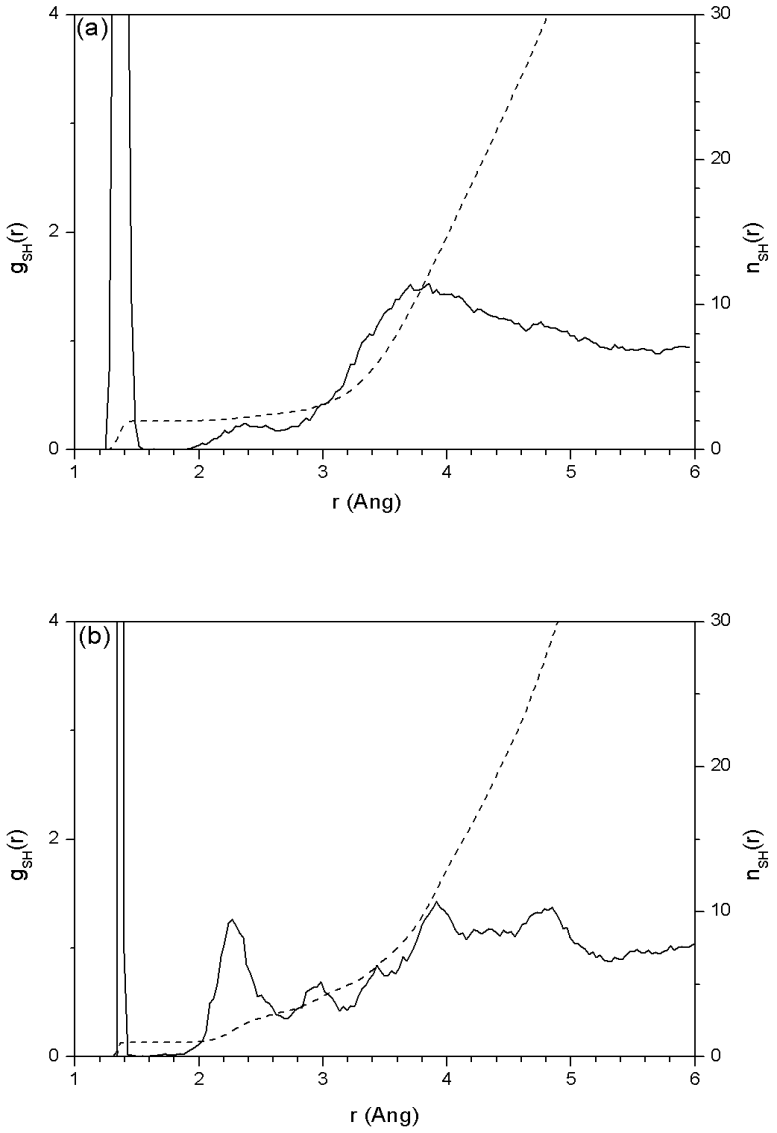

Figure 5.4: (a)-(b) S-H radial distribution functions $g(r)$ and running coordination number $n(r)$ for S^{2-} and FeS, respectively.

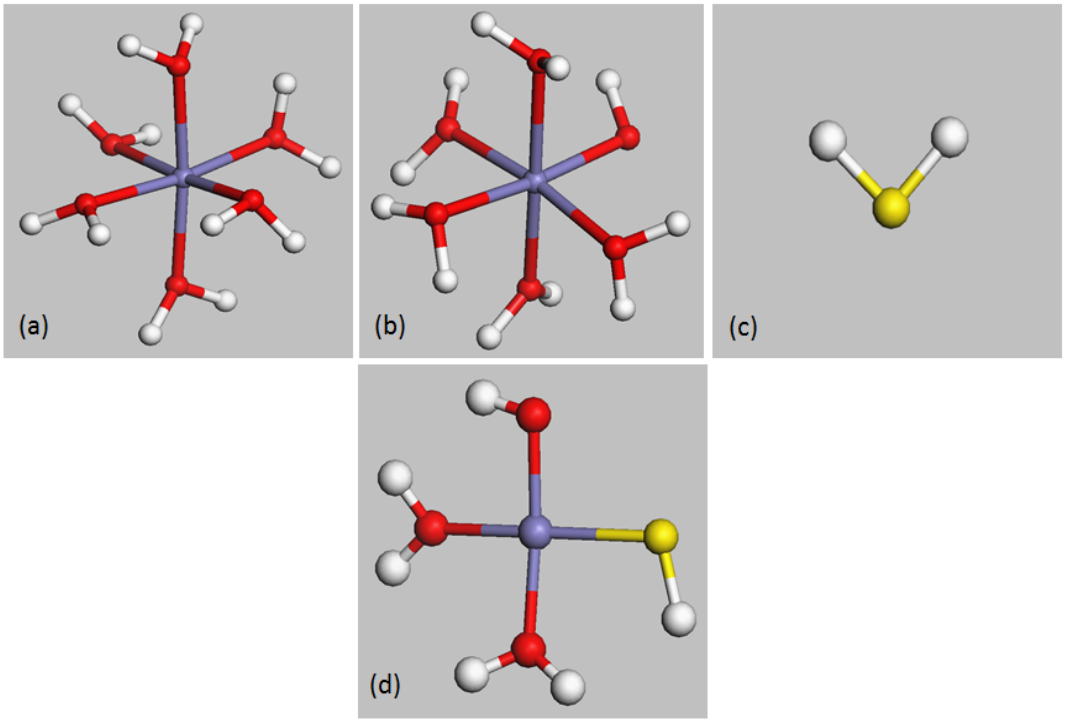

Figure 5.5: The final hydrated structures from our CPMD simulations of (a) Fe^{2+}, (b) Fe^{3+}, (c) S^{2-} and (d) FeS.

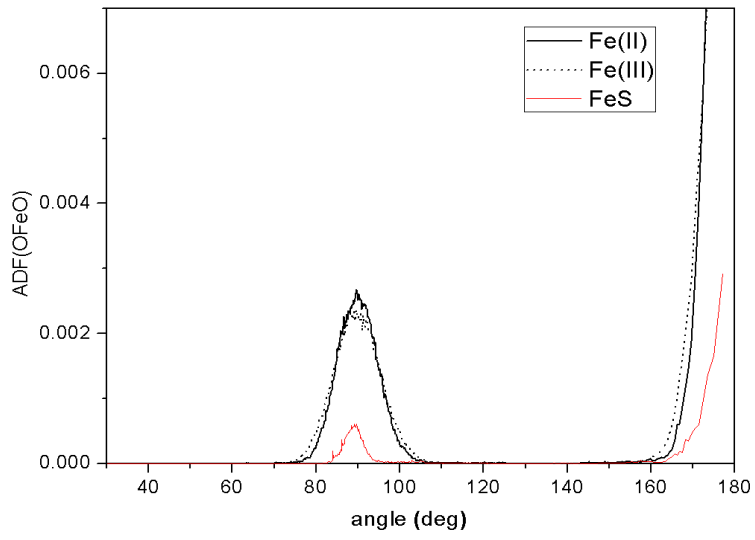

Figure 5.6: The O-Fe-O angular distribution for Fe^{2+}, Fe^{3+} and FeS.

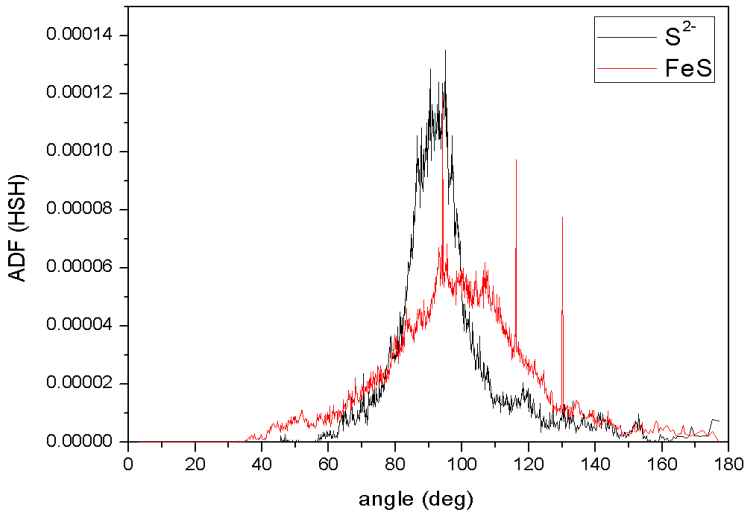

Figure 5.7: The H-S-H angular distribution for S^{2-} and FeS.

5.4 Stability of FeS_2, Fe_2S_2, Fe_2S_3, Fe_3S_3, Fe_4S_4 Clusters

For those systems with a stoichiometric ratio of Fe:S = 1, the simulations were run for a total of 20 ps, but the others for a total of only 5 ps, as by this point it was noted that irreversible dissociation of the clusters were occurring. Figure 5.8 shows the starting structure of each cluster, as optimised using DMol^3. In each instance there was complete dissociation of the cluster, normally after no longer than 2 ps. (For more pictures of these systems during the simulation, refer to the Appendix.)

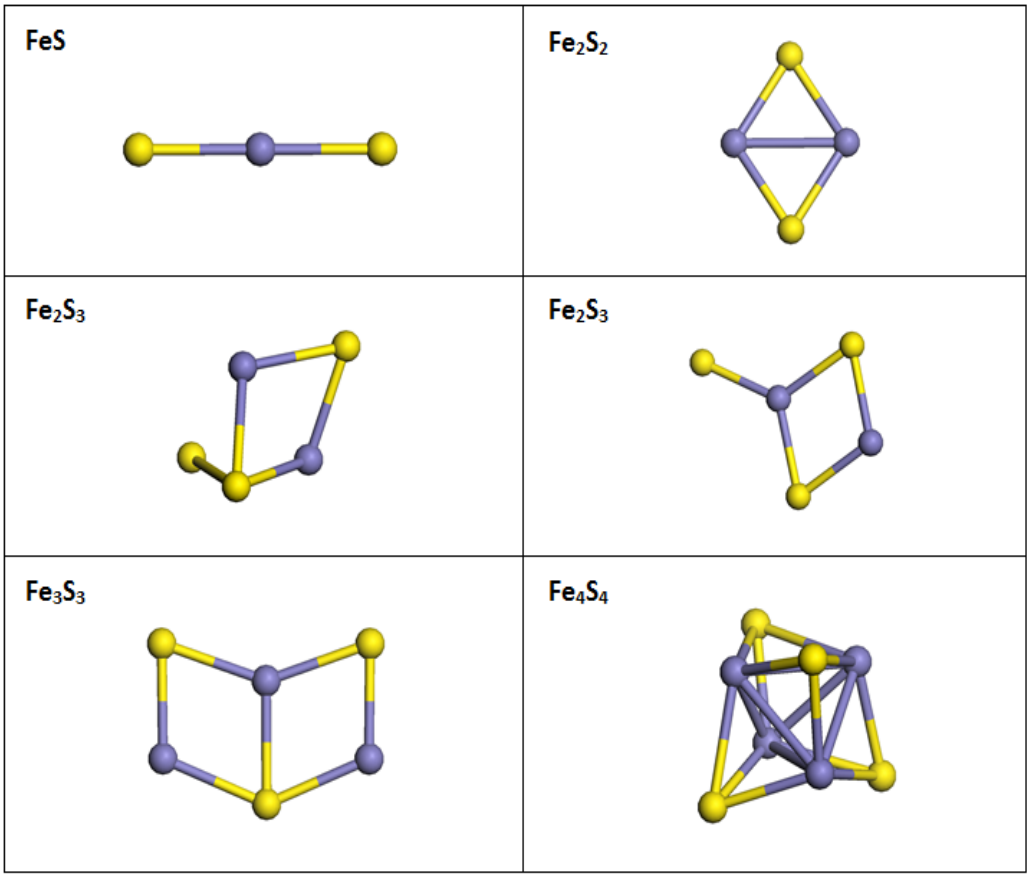

Figure 5.8: Initial starting structures for each of the following systems.

Figure 5.9 includes representative snapshots from the trajectory of Fe_2S_2. In particular, Figure 5.9 (d) shows that Fe_2S_2 dissociates into the protonated forms of the

sulphur ion, H_2S and HS^-, and into the hydrated iron species, $[Fe(H_2O)_4(OH)]^+$ and $Fe(H_2O)_2(OH)_2$.

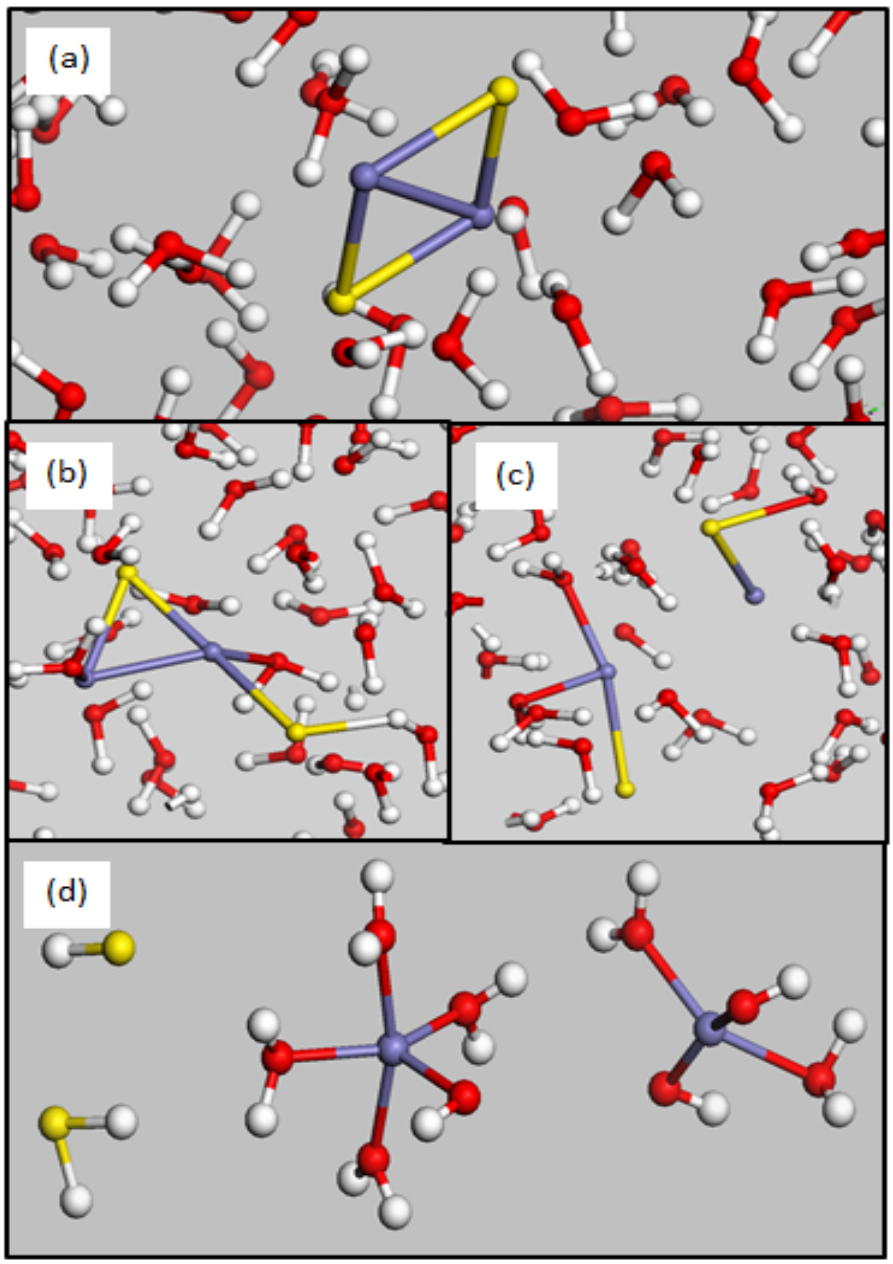

Figure 5.9: Representative snapshots of the CPMD trajectory of Fe_2S_2 in water, showing (a) the initial configuration at 0 ps, (b)-(c) intermediate configurations during the simulation, and (d) the final hydrated ions of the dissociated cluster at 20 ps.

It should be noted that Figure 5.9 (d) merely depicts the final conformation from our simulation, and not necessarily the final equilibrium state of the dissociated cluster. Similar results emerge with the Fe_3S_3 and Fe_4S_4 systems, with the formation of a $Fe(H_2O)_2(OH)_2$ and $Fe(OH)_3$ species respectively, amongst others (see Figure 5.10).

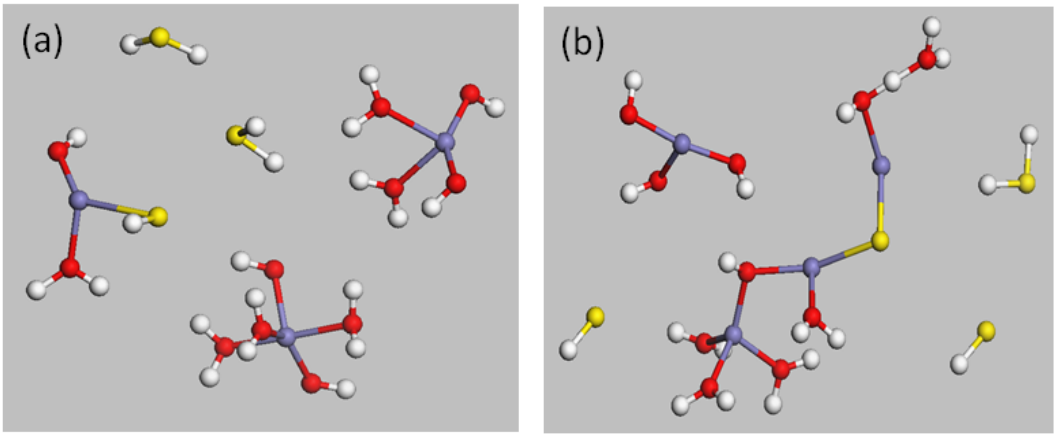

Figure 5.10: Resultant fragments from our CPMD simulations of (a) Fe_3S_3 and (b) Fe_4S_4.

In order to ensure that temperature was not playing a role in the dissociation of the clusters, we repeated our CPMD simulation of Fe_2S_2 at lower temperatures of 300 K and 350 K, but the results remained the same. We also conducted a further test by "freezing" the coordinates of the iron and sulphur in the Fe_2S_2 geometry, thus preventing dissociation and allowing the system to further equilibrate for the first 5 ps of the simulation, before removing the constraints. However, this alternative protocol also had no lasting effect on the overall result, with the cluster again dissociating almost immediately. Fe_xS_y (x,$y \geq 2$) clusters in solution are said to be routinely observed experimentally by electrochemical techniques [Rickard and Luther, 2007], but Theberge and Luther III [1997] were unsure about the validity of such results, as further analysis of the compounds suggested that they could in fact belong to any FeS solid phase with a 1:1 stoichiometry.

In order to rationalise the observed instability of Fe_xS_y (x,$y \geq 2$) clusters, we

computed the Gibbs free energy change (ΔG_{aq}) for some of the reactions that could be involved in the formation and dissociation of the Fe_2S_2 cluster. The reactions considered henceforth are reported in Table 5.3: reaction (1) represents the formation of hydrated FeS from the hydrated Fe^{2+} and S^{2-} ions ($Fe(H_2O)_6$ and HS^-), where part (a) considers the formation of hydrated $Fe(H_2O)_3SH$, and part (b) considers the alternative formation of $[Fe(H_2O)_2(OH)(SH)]^{2+}$, which is the species formed from the CPMD simulation of FeS in water; reaction (2) represents the formation of a hydrated Fe_2S_2 cluster, ($Fe_2S_2(H_2O)_4$), from hydrated FeS; reaction (3) models the dissociation of Fe_2S_2 into the fragments reported in Figure 5.9 (d).

Table 5.3: Condensation reactions for which ΔG_{aq} was calculated.

1.(a)	$Fe(H_2O)_6^{2+} + HS^- \rightarrow Fe(H_2O)_3(SH) + 3H_2O$
1.(b)	$Fe(H_2O)_6^{2+} + HS^- \rightarrow Fe(H_2O)_2(OH)(SH) + 2H_2O + H_3O^+$
2.	$2[Fe(H_2O)_2(OH)(SH)] \rightarrow Fe_2S_2(H_2O)_4 + 2H_2O$
3.	$Fe_2S_2(H_2O)_4 + 5H_2O \rightarrow H_2S + HS^- + Fe(H_2O)_4OH^+ + Fe(H_2O)_2(OH)_2$

However, following the cluster-continuum approach suggested by Pliego and Riveros [2001], we first computed the free energy of hydration of $HS(H_2O)_x$ x = 1-4, in order to check the number of water molecules which would give the optimum value of ΔG_{solv} for this species.

$$\Delta G_{solv}(HS^-) = \Delta G_{cluster}[HS^-(H_2O)_x] + \Delta G_{solv}[HS^-(H_2O)_x] + x\Delta G_{vap}(H_2O) \tag{5.5}$$

where we obtain values for $\Delta G_{cluster}$ by calculating the respective reaction:

$$HS^-(g) + xH_2O \quad \overrightarrow{\Delta G_{cluster}} \quad HS^-(H_2O)_x(g) \tag{5.6}$$

and

$$\Delta G_{vap} = x[-\Delta G_{solv}(H_2O) - RT\ln[RT] - RT\ln[H_2O]] \tag{5.7}$$

with ΔG_{solv} calculated as before.

The results obtained for ΔG_{solv} are listed in Table 5.4, and as we can see, HS^- alone without any coordinated waters gives the lowest value, meaning this was the most stable form of the solvated species.

Table 5.4: Calculated values of ΔG_{solv} (kcal mol^{-1}) for $HS(H_2O_x)$, x=1-4.

x	ΔG_{solv}
0	-74.3
1	-72.2
2	-69.4
3	-63.6
4	-43.2

The formation constant $\log\beta_1$ was then computed, which is an equilibrium constant for the formation of a complex in solution that acts as a measure of the strength of the interaction between the reagents that come together to form the complex, and can be calculated via $\log\beta_1 = -\Delta G_{aq}/(2.303^*RT)$, where 2.303 is the conversion factor between natural logarithms and logarithms. If we compare the formation constant of FeS in solution in accordance with our CPMD simulations (reaction 1.(a)), then the value of 2.41 falls within the range of 1.4-3.0 as determined from experiments [Dyrssen, 1988, Luther et al., 1996]. This gives confidence that the method employed in this study for the calculation of the free energies of reaction is reasonably accurate.

Table 5.5 shows the calculated ΔG_{aq} for each of the reactions 1-3 in Table 5.3, as well as the different energy contributions to the Gibbs free energy. The results show that while the formation of FeS in aqueous solution is thermodynamically favourable and leads to a stable FeS product (as observed in our CPMD simulation), the formation of an Fe_2S_2 cluster is endergonic ($\Delta G > 0$) and will not occur spontaneously, and thermodynamically the more preferable option is to dissociate, for example, in accordance with equation (3) in Table 5.3. These findings would explain why the clusters Fe_xS_y ($x,y \geq 2$) dissociate almost immediately in water after only a few picoseconds of molecular dynamics simulation, and also tells us why, rather than dissociate into

the hydrated FeS species, it will instead dissociate into its constituent ions and form iron hydroxide species. However, if we now focus on the gas-phase energy contributions, $\Delta G_{VRT} = \Delta H_{VRT} - T\Delta S_{VRT}$, for reactions (2) and (3), which correspond to the dimerisation and dissociation processes respectively, it is clear that with increasing temperature, the entropic contribution $-T\Delta S_{VRT}$ for reaction (2) will become more negative, but for reaction (3) will now become positive. The implication is that at higher temperatures, the formation of Fe_2S_2 becomes thermodynamically possible. Our calculations were conducted under natural water conditions, yet the environment where such "life-forming" reactions were supposed to have occurred, such as black smokers, would have been subject to extreme conditions including temperature and pressure [Cairns-Smith et al., 1992, Russell and Arndt, 2005, Wächtershäuser, 2000]. In addition, there is the possibility of stabilisation through the presence of other inorganic compounds and salts that are found in seawater. For example, the value of the formation constant $\log\beta_1$ for the reaction $Fe^{2+} + HS^- \rightleftharpoons FeSH^+$ is affected by the medium in which its measurement is carried out [Rickard and Luther, 2007].

Table 5.5: Calculated ΔG_{aq} values for the condensation reactions reported in Table 5.3. The gas-phase contributions (ΔE, ΔG_{VRT}, ΔH_{VRT} and $T\Delta S_{VRT}$) were computed at the mPW1B95/(aug-)cc-pVTZ//mPW1B95/6-31G(d) levels of theory; the energy term due to changes in internal geometry when passing from the gas-phase to the solution $\Delta\Delta E_{Q'\rightarrow Q}$ was computed at the HF/6-31G(d) level; the solvation free energy $\Delta\Delta G_{solv}$ was evaluated using the UAHF/CPCM solvation model at the HF/6-31G(d) level of theory. All values are in kcal mol^{-1}.

reaction	ΔE_e	ΔG_{VRT}	ΔH_{VRT}	$T\Delta S_{VRT}$	$\Delta\Delta E_{(Q'\rightarrow Q)}$	$\Delta\Delta G_{solv}$	ΔG_{aq}
1.(a)	-157.9	-23.8	-3.7	20.0	5.07	155.0	-21.6
1.(b)	-97.4	-22.5	-3.6	18.8	4.0	112.5	-3.3
2.	53.6	-4.0	2.9	6.9	8.8	1.8	60.3
3.	57.6	17.5	-2.1	-19.5	-44.2	-99.6	-68.7

5.5 Conclusions

Our results indicate that the presence of sulphur affects the hydration structure of iron by reducing the coordination sphere of Fe. While isolated Fe can coordinate a total of six oxygen atoms, Fe bound to S will only coordinate three. This species is shown to exist as $Fe(H_2O)_2(OH)SH$ in an aqueous environment, in a square planar coordination environment. We also learn from our CPMD simulations of Fe_xS_y clusters (x,$y \geq 2$), that these will be unstable in water and dissociate after only a few picoseconds. The calculated Gibbs free energies ΔG_{aq} for the formation of FeS, Fe_2S_2 and its subsequent dissociation, shows that at 300 K the formation of FeS is exergonic, while the formation of Fe_2S_2 is endergonic. The subsequent dissociation of this FeS dimer is also thermodynamically preferable, explaining the results observed from our CPMD simulations for those Fe_xS_y clusters where x,$y \geq 2$. Evaluation of the gas-phase entropic contribution $-T\Delta S_{VRT}$ indicates that with increasing temperature, the contribution to the Gibbs free energy from this term will become more negative, and thus formation of the dimer more plausible; similarly, for the dissociation process, at higher temperatures $-T\Delta S_{VRT}$ will become positive, and thus dissociation less likely. Our results indicate that under ambient conditions, the formation of iron sulphides is in competition with the formation of iron hydroxides, with hydroxide formation preferable under these conditions. We know iron sulphide formation to be possible, but under non-equilibrium conditions such as those found in submarine hydrothermal vents.

Chapter 6

SUMMARY AND CONCLUSIONS

This thesis has used a combination of density functional theory (DFT) and molecular dynamics (MD) to study bio-inspired iron sulphide minerals. In order to further explore the analogy between present-day FeS minerals and those implicated in Origin of Life theories and found in enzymes, our study was split into three main areas: cation distribution within the greigite (Fe_3S_4) bulk, surface simulations of the mineral violarite ($FeNi_2S_4$), and MD simulations of FeS clusters in water.

We began by looking at the mineral greigite, and investigating the subsequent doping and distribution of Ni over its octahedral and tetrahedral sites with varying concentration. At low dopant concentrations ($x \leq 0.125$ in $(Ni_xFe_{1-x})_3S_4$), SOD proved extremely useful in reducing the configurational space to be sampled, and in turn this meant we were able to perform statistical analysis over the entire configurational spectrum. Results demonstrated that at low concentrations it was energetically more favourable to substitute Ni in an octahedral site than a tetrahedral site. However, analysis of the partitioning at each concentration suggested that at higher dopant concentrations, the extra energetic cost of placing a Ni in a tetrahedral site over an octahedral would decrease.

In order to test this hypothesis, it was necessary to adopt a different approach in order to sample the considerably large configurational space at dopant concentrations

of $0.167 \leq x \leq 0.333$. We therefore had to rely on Monte Carlo methods and an energy model based on nearest-neighbour energy interactions. This approach proved to be extremely useful in allowing us access and extract the necessary information we required, namely the average energies and site occupancies at these higher dopant concentrations, and comparison of the results from our model against those from DFT revealed the accuracy and suitability in using it for this task. We were thus able to confirm the trend predicted from our initial results at low concentration, whereby at higher concentrations Ni would now be preferentially located in the tetrahedral sites. Calculation of the enthalpies of mixing with respect to both polydymite (Ni_3S_4) and violarite in order to elucidate what would be the most likely composition along the Fe_3S_4-Ni_3S_4 series, also revealed violarite to be the most energetically stable member. This fits in with the lack of documentation of (Fe,Ni) thiospinels with low concentrations of Ni in nature. These findings are significant in terms of comparisons between (Fe,Ni)S minerals and those enzymes containing (Fe,Ni)S clusters, in which Ni is usually tetra-coordinated and exists in low Ni:Fe ratio [Dobbek et al., 2001, Ragsdale, 2009, Thauer, 2001], as our results show that at low concentrations Ni will be octahedrally coordinated within the lattice.

We then moved on to simulations of violarite's low-Miller index surfaces, using DFT-D2 methods. Analysis and calculation of the respective surface energies of the naked (001), (011) and (111) surfaces revealed a termination of the (001) to be the most energetically stable, and relaxation of this was accompanied by migration of the uppermost octahedral Ni cations further into the bulk. The (111) was found to be the least stable, and also the least reactive with respect to water adsorption. To simulate water adsorption on the surfaces and determine the preferred site of adsorption, it was necessary to adopt an approach of trial and error, whereby adsorption was attempted on each possible site on the surface, and the respective adsorption energy calculated. Again, calculation of the respective energies showed that adsorption was energetically more feasible on the (011) surface, and similarly, that it was preferable on a Fe_B site

over a Ni_B site. We also noted the phenomenon of synergistic adsorption, whereby the adsorption of one water was conducive to the adsorption of the next, and this was explained through the formation of hydrogen bonds between the water molecules, which acted to stabilise the system. Dissociation of the waters also caused adjacent metallic sites to "activate", increasing their reactivity for further adsorption.

The Wulff construction [Wulff, 1901] was a useful method for determining the morphology of a $FeNi_2S_4$ particle in vacuum and in the presence of two waters. In both instances, only the (001) would be expressed; however, calculation of the linear relationship between the (111) surface energy and the number of waters adsorbed suggested that in the presence of a greater number of waters ($\sim$ 8 molecules), the (111) would now become more energetically stable than the other two.

In the final part of our study, we performed CPMD simulations of FeS clusters in water. Calculation of the RDF and ADF proved to be extremely useful tools for investigating the hydrated structures of the Fe^{2+}, Fe^{3+} and S^{2-} ions, and FeS, yielding such information as the number of waters bound in each hydration shell, and at what distances and angles. Our simulations produced slightly different results from those reported in the literature. We found that for Fe^{3+}, the first hydration shell was composed of five waters and one OH group, differing from the six waters usually reported in the literature, and consequently we obtained a slightly shorter average bond length for the first hydration shell. We also observed that S bound to a Fe cation will act to reduce the hydration shell of Fe, when compared to the typical hexa-aqua arrangement of Fe complexes in water. The first hydration shell will now consist of two waters and one OH group, again reflected by a split peak in the RDF, referring to the two different bond types. The number of hydrogen bonds that each hydrated species can participate in was also demonstrated to be reflective of the charge of the cation, with both the Fe in FeS and the single Fe^{2+} cation being able to participate in a total of two.

It was necessary to adopt a different approach to understand our results from

the simulation of clusters with a greater iron and sulphur content (Fe_xS_y $x,y \geq 2$), as the results from our CPMD simulations showed dissociation of each cluster after a few picoseconds. In order to make sense of these results, we calculated the Gibbs free energy change of possible reactions leading to the formation and dissociation of a Fe_2S_2 cluster. This proved to be extremely beneficial when understanding our results from our CPMD simulations, as analysis of the individual energetic contributions were used to show that the formation of these clusters in water is possible, but temperature-dependent. Putting this in context of what is found in the literature, then although it has been said that Fe_xS_y clusters with x,y$\geq$2 are routinely observed experimentally [Rickard and Luther, 2007], it has been argued that these results could belong to any FeS solid phase with a 1:1 stoichiometry [Theberge and Luther III, 1997]. With respect to Origin of Life theories, our simulations have been conducted in different conditions to those that would have been present on the Hadean ocean floor, which would have included subjection to extremes of temperature and pressure.

Continuation of our work could go in various directions. One possible avenue to further our work on violarite would be to adsorb successive molecules of water on each surface, to test whether or not our hypothesis that the (111) may surpass the (001) as the most energetically stable surface is a valid one. We could also then go on to look at the adsorption of carbon dioxide on the surfaces. With respect to greigite, there are various possibilities, one of which would include further doping of Ni up to polydymite (Ni_3S_4). A different approach would be to look at Fe-doping of polydymite, and compare the results. A VASP comparison study of the substitution of divalent cations into pure-iron greigite, in place of the Fe^{2+} ions in the octahedral sites could also prove insightful. Hopefully, via substitution of a rigid divalent cation with a similar radius as that of Fe^{2+} (possible candidates include Mg^{2+}, Cd^{2+}, Zn^{2+}), we would be able to identify with confidence how the Fe^{2+} and Fe^{3+} ions are distributed over the octahedral sites. We could also look at possible addition of Ni

into our FeS clusters, and perform CPMD simulations of these. A shift in focus from greigite and violarite onto other iron sulphides, more specifically, those clusters found within the active sites of the biologically relevant enzymes, could also prove beneficial. Simulations of these clusters in both vacuum and water would be necessary in fully understanding the structure and nature of these clusters. It would be interesting to observe the stability of such clusters in the absence of any cofactors/proteins that would otherwise be present in the enzymes, and the absence of these agents would give a more informed idea about whether CO_2 catalysis by such minerals alone was really possible and would have facilitated the origin of life.

Appendix

Supplementary information for Chapter 3 section 3.2.3.

The basic outline of our NN Model code to calculate the average energies and tetrahedral site occupancies at different concentrations of Ni.

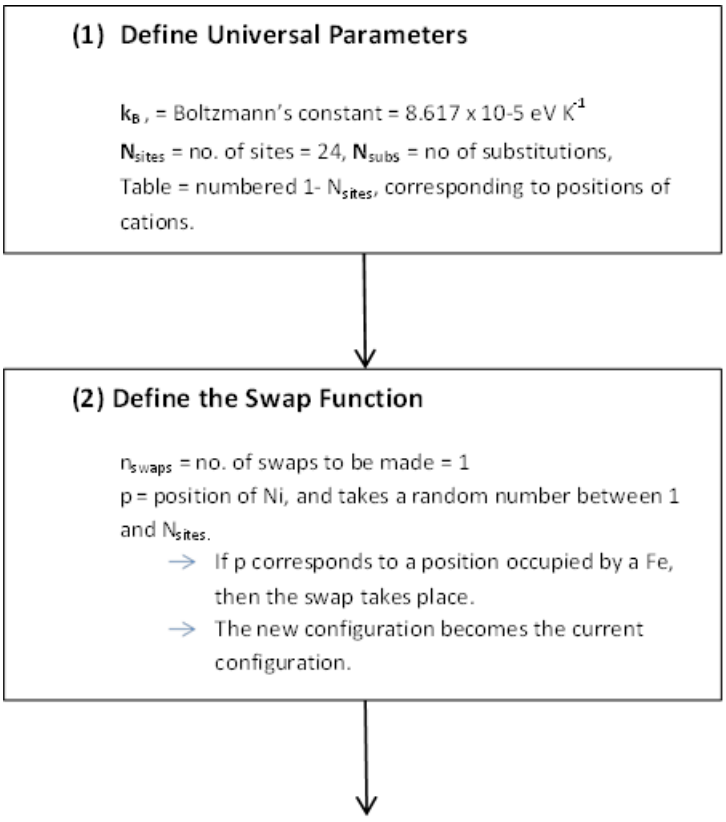

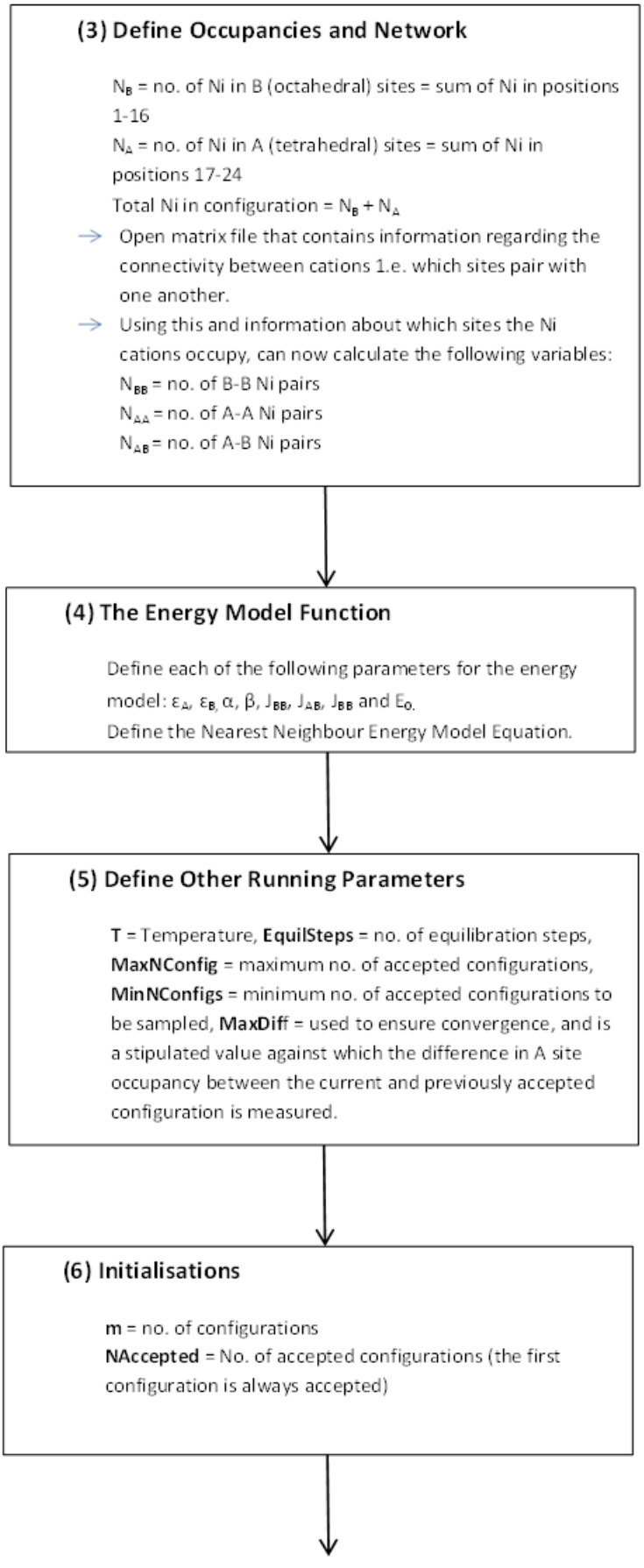
(3) Define Occupancies and Network
N_B = no. of Ni in B (octahedral) sites = sum of Ni in positions 1-16
N_A = no. of Ni in A (tetrahedral) sites = sum of Ni in positions 17-24
Total Ni in configuration = $N_B + N_A$
→ Open matrix file that contains information regarding the connectivity between cations 1.e. which sites pair with one another.
→ Using this and information about which sites the Ni cations occupy, can now calculate the following variables:
N_{BB} = no. of B-B Ni pairs
N_{AA} = no. of A-A Ni pairs
N_{AB} = no. of A-B Ni pairs
(4) The Energy Model Function
Define each of the following parameters for the energy model: ε_A, ε_B, α, β, J_{BB}, J_{AB}, J_{BB} and E_O.
Define the Nearest Neighbour Energy Model Equation.
(5) Define Other Running Parameters
T = Temperature, **EquilSteps** = no. of equilibration steps, **MaxNConfig** = maximum no. of accepted configurations, **MinNConfigs** = minimum no. of accepted configurations to be sampled, **MaxDiff** = used to ensure convergence, and is a stipulated value against which the difference in A site occupancy between the current and previously accepted configuration is measured.
(6) Initialisations
m = no. of configurations
NAccepted = No. of accepted configurations (the first configuration is always accepted)

(7) Main Cycle

While the system has not converged:

- Call step **(2)** to swap a Ni for a Fe to generate a new configuration.
- Call step **(3)** to calculate the energy of the new configuration.
- Generate a random number
- Calculate the probability such that : $P = \exp(-\Delta E/k_bT)$
- Accept the configuration if:
  - Energy < Previous Energy or
  - P > RandomNumber. Otherwise go back to step **(2)**.

If accepted (and the m is > EquilSteps, then:

- The A site occupancy and energy for that configuration is incorporated into the average A site occupancy and energy for that conc. of Ni.
- The current configuration becomes the template for the next configuration, and then calls step **(2).**

Convergence is achieved if:

- m > EquilSteps + MinSteps
- The difference in A site occupancies is < MaxDiff.

Supplementary information for Chapter 5 Section 5.2.4.

Calculation of ΔG_{aq} for the following reaction:

$$\mathrm{Fe(H_2O)_6^{2+} + HS^- \rightarrow Fe(H_2O)_3(SH) + 3H_2O} \tag{6.1}$$

$$\Delta G_{aq} = \Delta E_e + \Delta G_{VRT} + \Delta\Delta G_{solv} + \Delta\Delta E_{Q' \rightarrow Q} \tag{6.2}$$

Then

$$\Delta E_e = (E[\mathrm{Fe(H_2O)_3(SH)}] + 3.E[\mathrm{3H_2O}]) - \left(E[\mathrm{Fe(H_2O)_6^{2+}}] + E[\mathrm{HS^-}]\right) \tag{6.3}$$

$$\Delta G_{VRT} = (G_{VRT}[\mathrm{Fe(H_2O)_3(SH)}] + 3.G_{VRT}[\mathrm{3H_2O}]) - \left(G_{VRT}[\mathrm{Fe(H_2O)_6^{2+}}] + G_{VRT}[\mathrm{HS^-}]\right) \tag{6.4}$$

$$\Delta G_{solv} = (\Delta G_{solv}[\mathrm{Fe(H_2O)_3(SH)}] + 3.\Delta G_{solv}[\mathrm{3H_2O}]) - \left(\Delta G_{solv}[\mathrm{Fe(H_2O)_6^{2+}}] + \Delta G_{solv}[\mathrm{HS^-}]\right) \tag{6.5}$$

$$\Delta\Delta E_{Q' \rightarrow Q} = \left(\Delta E_{Q' \rightarrow Q}[\mathrm{Fe(H_2O)_3(SH)}] + 3.\Delta E_{Q' \rightarrow Q}[\mathrm{3H_2O}]\right) - \left(\Delta E_{Q' \rightarrow Q}[\mathrm{Fe(H_2O)_6^{2+}}] + \Delta E_{Q' \rightarrow Q}[\mathrm{HS^-}]\right) \tag{6.6}$$

Supplementary information for Chapter 5 Section 5.4.

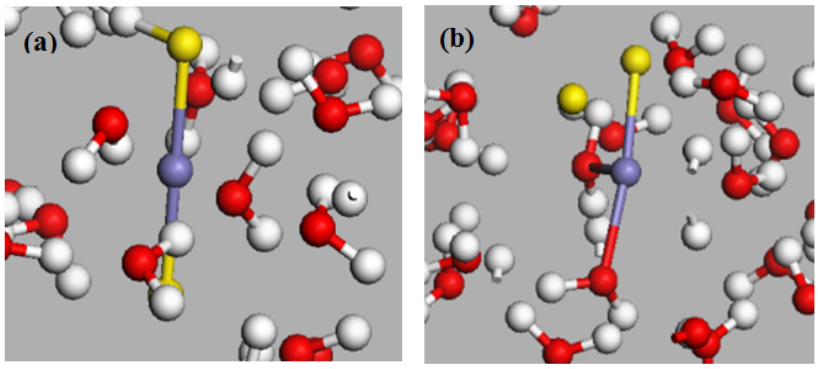

Figure 6.1: Car-Parrinello molecular dynamics (MD) simulations of FeS_2 in water: (a) configuration at t = 0 ps (b) final configuration at t = 2 ps.

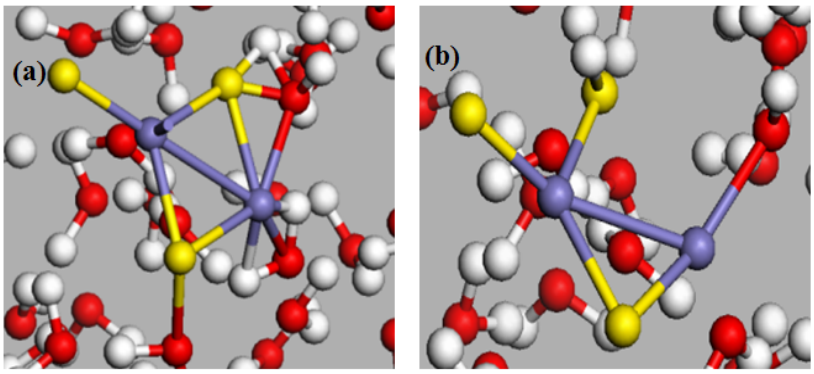

Figure 6.2: Car-Parrinello MD simulations of Fe_2S_3(a) in water: (a) intermediate configuration during simulation and (b) final configuration at t = 2 ps.

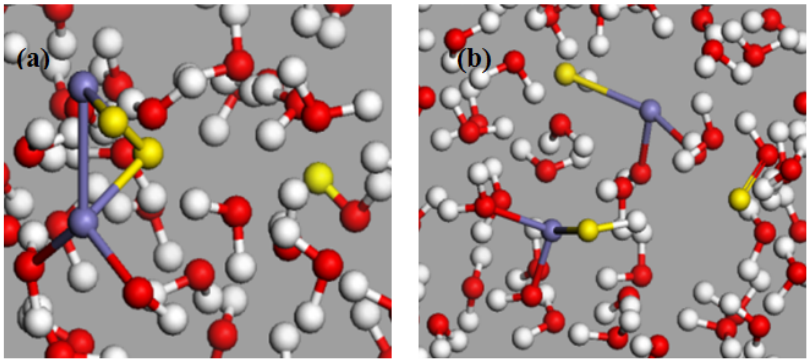

Figure 6.3: Car-Parrinello MD simulations of Fe_2S_3(b) in water: (a) intermediate configuration during simulation and (b) final configuration at t = 2 ps.

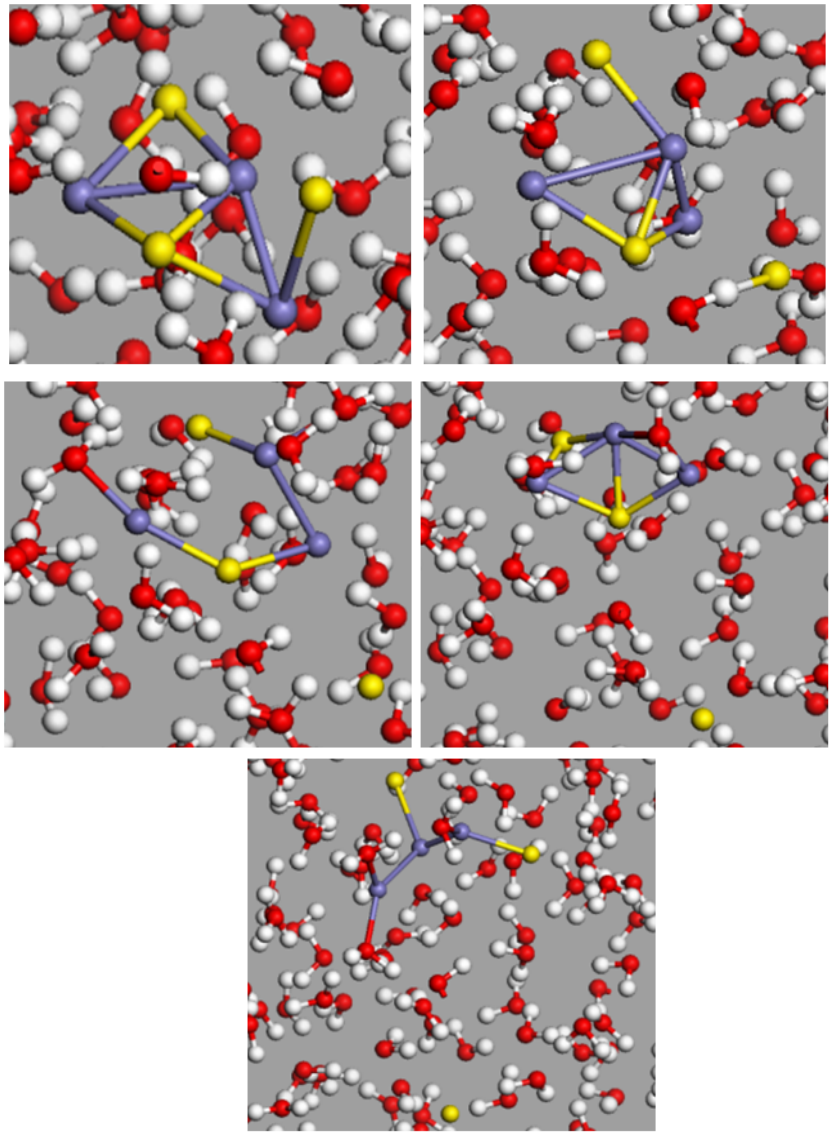

Figure 6.4: Snapshots taken during Car-Parrinello MD simulation of Fe_3S_3 in water.

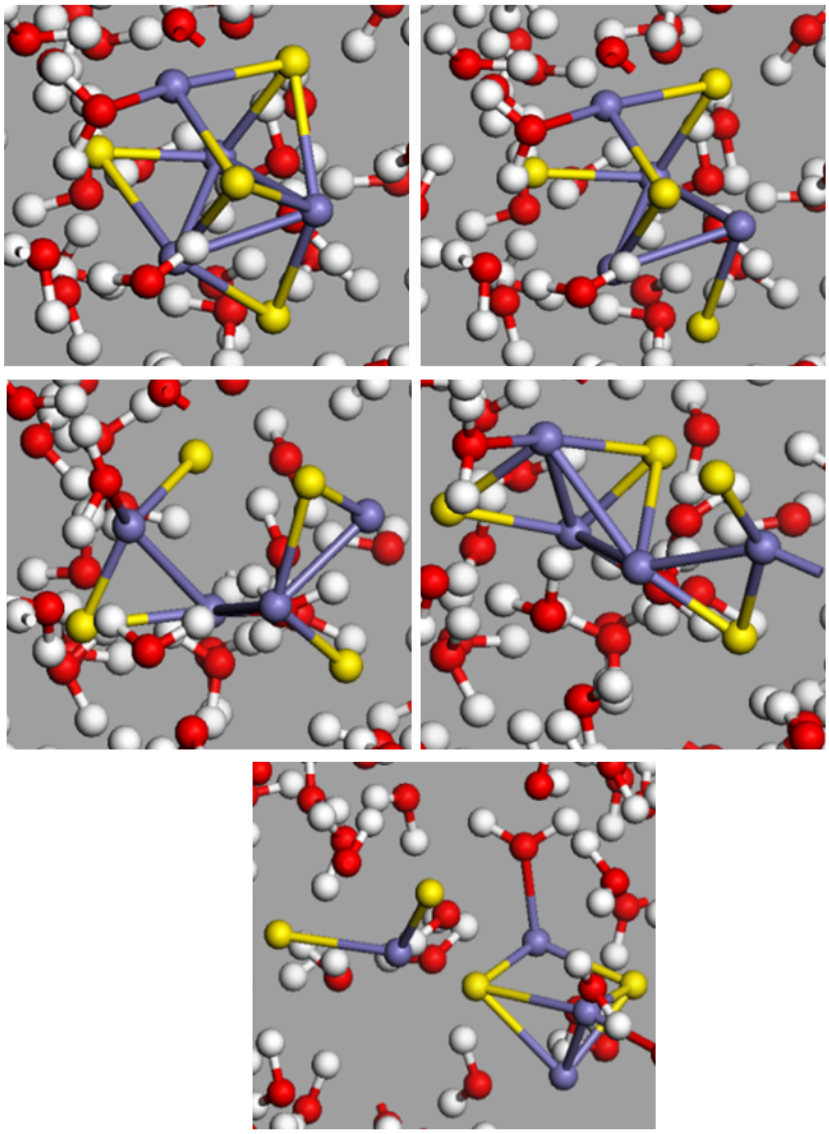

Figure 6.5: Snapshots taken during Car-Parrinello MD simulation of Fe_4S_4 in water.

Bibliography

S. Amira, D. Spangberg, V. Zelin, M. Probst, and K. Hermansson. Car-Parrinello Molecular Dynamics Simulation of Fe^{3+}(aq). *Journal of Physical Chemistry B*, 109(29):14235–14242, 2005.

R. F. W. Bader, M. T. Carroll, J. R. Cheeseman, and C. Chang. Properties of atoms in molecules: Atomic volumes. *Journal of the American Chemical Society*, 109(26): 7968–7979, 1987.

K. Baldridge and A. Klamt. First principles implementation of solvent effects without outlying charge error. *Journal of Chemical Physics*, 106(16):6622–6633, 1997.

V. Barone and M. Cossi. Quantum calculation of molecular energies and energy gradients in solution by a conductor solvent model. *Journal of Physical Chemistry A*, 102(11):1995–2001, 1998.

A. D. Becke. Density-functional exchange-energy approximation with correct asymptotic-behaviour. *Physical Review A*, 38(6):3098–3100, 1988.

A. D. Becke. Density-functional thermochemistry. IV. A new dynamical correlation functional and implications for exact-exchange mixing. *Journal of Chemical Physics*, 104(3):1040–1046, 1996.

A. Ben-Naim. *Water and Aqueous Solutions*. Plenum Press, 1974.

A. Ben-Naim. *J. Phys. Chem*, 82:792, 1978.

A. Ben-Naim. *Solvation Thermodynamics*. Plenum Press, 1987.

R. A. Berner. Tetragonal iron sulfide. *Science*, 137(3531):669, 1962.

R. A. Berner. Thermodynamic stability of sedimentary iron sulfides. *American Journal of Science*, 265(9):773, 1967.

R. A. Berner. Sedimentary pyrite formation. *American Journal of Science*, 268(1):1, 1970.

F. Bloch. Radiation absorpability in quantum mechanics. *Physikalische Zeitschrift*, 29:58–66, 1928.

E. Blöchl, M. Keller, G. Wachtershauser, and K. O. Stetter. Reactions depending on iron sulfide and linking geochemistry with biochemistry. *Proceedings of the National Academy of Sciences of the United States of America*, 89(17):8117–8120, 1992.

P. E. Blöchl. Projector augmented-wave method. *Physical Review B*, 50(24):17953–17979, 1994.

A. Bondi. van der Waals volumes and radii. *Journal of Physical Chemistry*, 68(3): 441, 1964.

S. F. Boys. Electronic wave functions. I. A general method of calculation for the stationary states of any molecular system. *Proceedings of the Royal Society of London Series A - Mathematical and Physical Sciences*, 200(1063):542–554, 1950.

B. S. Brunschwig, C. Creutz, D. H. Macartney, T. K. Sham, and N. Sutin. The role of inner-sphere configuration changes in electron-exchange reactions of metal-complexes. *Faraday Discussions*, 74:113–127, 1982.

A. G. Cairns-Smith, A. J. Hall, and M. J. Russell. Mineral theories of the origin of life and an iron sulfide example. *Origins of Life and Evolution of the Biosphere*, 22(1-4):161–180, 1992.

S. Canaguier, V. Artero, and M. Fontecave. Modelling NiFe hydrogenases: nickel-based electrocatalysts for hydrogen production. *Dalton Transactions*, (3):315–325, 2008.

R. Car and M. Parrinello. Unified Approach for Molecular Dynamics and Density-Functional Theory. *Physical Review Letters*, 55(22):2471–2474, 1985.

A. C. Chamberlain and J. G. Dunn. The relationship between stoichiometry and reactivity for violarite. *Thermochimica Acta*, 341:367–376, 1999.

A. Chandra. Effects of ion atmosphere on hydrogen-bond dynamics in aqueous electrolyte solutions. *Physical Review Letters*, 85(4):768–771, 2000.

L. Chang, A. P. Roberts, Y. Tang, B. D. Rainford, A. R. Muxworthy, and Q. W. Chen. Fundamental magnetic parameters from pure synthetic greigite (Fe_3S_4). *Journal of Geophysical Research-Solid Earth*, 113(B6), 2008.

J. Charnock, C. D. Garner, R. A. D. Pattrick, and D. J. Vaughan. An EXAFS study of thiospinel minerals. *American Mineralogist*, 75(3-4):247–255, 1990.

G. D. Cody. Transition metal sulfides and the origins of metabolism. *Annual Review of Earth and Planetary Sciences*, 32:569–599, 2004.

C. Copret. Catalysis by transition metal sulphides. From molecular theory to industrial applications. *Journal of Catalysis*, 307:121, 2013.

M. Cossi, N. Rega, G. Scalmani, and V. Barone. Energies, structures, and electronic properties of molecules in solution with the C-PCM solvation model. *Journal of Computational Chemistry*, 24(6):669–681, 2003.

J. R. Craig. Violarite stability relations. *American Mineralogist*, 56(7-8):1303, 1971.

C. J. Cramer. *Essentials of Computational Chemistry*, pages 347–383. Second edition, 2004.

P. D'Angelo and M. Benfatto. Effect of multielectronic configurations on the XAFS analysis at the Fe K edge. *Journal of Physical Chemistry A*, 108(20):4505–4514, 2004.

C. Darnault, A. Volbeda, E. J. Kim, P. Legrand, X. Vernede, P. A. Lindahl, and J. C. Fontecilla-Camps. Ni-Zn-[Fe_4S_4] and Ni-Ni-[Fe_4S_4] clusters in closed and open subunits of acetyl-CoA synthase/carbon monoxide dehydrogenase. *Nature Structural Biology*, 10(4):271–279, 2003.

W. Davison. The solubility of iron sulfides in synthetic and natural-waters at ambient-temperature. *Aquatic Sciences*, 53(4):309–329, 1991.

N. H. de Leeuw. *Computer simulations of surfaces and interfaces: a case study of the hydration and dissolution of -quartz SiO_2*, volume 4 of *Seminarios de la Sociedad Española de Mineralogìa*. 2006.

M. J. Dekkers, H. F. Passier, and M. A. A. Schoonen. Magnetic properties of hydrothermally synthesized greigite (Fe_3S_4) - II. High- and low-temperature characteristics. *Geophysical Journal International*, 141(3):809–819, 2000.

B. Delley. An all-electron numerical-method for solving the local density functional for polyatomic-molecules. *Journal of Chemical Physics*, 92(1):508–517, 1990.

B. Delley. From molecules to solids with the $DMol^3$ approach. *Journal of Chemical Physics*, 113(18):7756–7764, 2000.

A. Devey and N. H. de Leeuw. Density functional theory study of the high- and low-temperature phases of cubic iron sulfide. *Physical Review B*, 82(23):235112–235122, 2010.

A. J. Devey, R. Grau-Crespo, and N. H. de Leeuw. Combined density functional theory and interatomic potential study of the bulk and surface structures and prop-

erties of the iron sulfide mackinawite (FeS). *Journal of Physical Chemistry C*, 112 (29):10960–10967, 2008.

A. J. Devey, R. Grau-Crespo, and N. H. de Leeuw. Electronic and magnetic structure of Fe_3S_4: GGA+U investigation. *Physical Review B*, 79(19):195126–195132, 2009.

D. Di Tommaso and N. H. de Leeuw. The onset of calcium carbonate nucleation: A density functional theory molecular dynamics and hybrid microsolvation/continumn study. *Journal of Physical Chemistry B*, 112(23):6965–6975, 2008.

D. Di Tommaso and N. H. de Leeuw. Theoretical study of the dimerization of calcium carbonate in aqueous solution under natural water conditions. *Geochimica et Cosmochimica Acta*, 73(18):5394–5405, 2009.

D. Di Tommaso and N. H. de Leeuw. First principles simulations of the structural and dynamical properties of hydrated metal ions Me^{2+} and solvated metal carbonates (Me = Ca, Mg, and Sr). *Crystal Growth & Design*, 10(10):4292–4302, 2010.

H. Dobbek, V. Svetlitchnyi, L. Gremer, R. Huber, and O. Meyer. Crystal structure of a carbon monoxide dehydrogenase reveals a [Ni-4Fe-5S] cluster. *Science*, 293 (5533):1281–1285, 2001.

E. Drobner, H. Huber, G. Wachtershauser, D. Rose, and K. O. Stetter. Pyrite formation linked with hydrogen evolution under anaerobic conditions. *Nature*, 346 (6286):742–744, 1990.

A. J. Duben and S. Miertus. The effect of solvent on the internal-rotation of formamide: A CNDO/2-solvaton method study. *Theoretica Chimica Acta*, 60(4): 327–337, 1981.

J. G. Dunn and V. L. Howes. The oxidation of violarite. *Thermochimica Acta*, 283: 305–316, 1996.

D. Dyrssen. Sulfide complexation in surface seawater. *Marine Chemistry*, 24(2): 143–153, 1988.

J. W. Elder. Physical processes in geothermal areas. *Terrestrial Heat Flow, Geophysical Monograph Series*, 8:211–239, 1965.

B. Ensing. *Chemistry in water: First Principles Computer Simulations*. PhD thesis, 2003.

P. P. Ewald. The calculation of optical and electrostatic grid potential. *Annalen Der Physik*, 64(3):253–287, 1921.

E. Fermi. A statistical method for determining some properties of the atoms and its application to the theory of the periodic table of elements. *Zeitschrift Fur Physik*, 48(1-2):73–79, 1928.

J. G. Ferry. CO Dehydrogenase. *Annual Review of Microbiology*, 49:305–333, 1995.

R. P. Feynman. Forces in molecules. *Physical Review*, 56(4):340–343, 1939.

F. Floris, M. Persico, A. Tani, and J. Tomasi. Ab initio effective pair potentials for simulations of the liquid-state, based on the polarizable continuum model of the solvent. *Chemical Physics Letters*, 199(6):518–524, 1992.

A. M. Freke and D. Tate. Formation of magnetic iron sulphide by bacterial reduction of iron solutions. *Journal of Biochemical and Microbiological Technology and Engineering*, 3(1):29, 1961.

M. J. Frisch, G. W. Trucks, H. B. Schlegel, G. E. Scuseria, M. A. Robb, J. R. Cheeseman, J. A. Montgomery, Jr., T. Vreven, K. N. Kudin, J. C. Burant, J. M. Millam, S. S. Iyengar, J. Tomasi, V. Barone, B. Mennucci, M. Cossi, G. Scalmani, N. Rega, G. A. Petersson, H. Nakatsuji, M. Hada, M. Ehara, K. Toyota, R. Fukuda, J. Hasegawa, M. Ishida, T. Nakajima, Y. Honda, O. Kitao, H. Nakai, M. Klene,

X. Li, J. E. Knox, H. P. Hratchian, J. B. Cross, V. Bakken, C. Adamo, J. Jaramillo, R. Gomperts, R. E. Stratmann, O. Yazyev, A. J. Austin, R. Cammi, C. Pomelli, J. W. Ochterski, P. Y. Ayala, K. Morokuma, G. A. Voth, P. Salvador, J. J. Dannenberg, V. G. Zakrzewski, S. Dapprich, A. D. Daniels, M. C. Strain, O. Farkas, D. K. Malick, A. D. Rabuck, K. Raghavachari, J. B. Foresman, J. V. Ortiz, Q. Cui, A. G. Baboul, S. Clifford, J. Cioslowski, B. B. Stefanov, G. Liu, A. Liashenko, P. Piskorz, I. Komaromi, R. L. Martin, D. J. Fox, T. Keith, M. A. Al-Laham, C. Y. Peng, A. Nanayakkara, M. Challacombe, P. M. W. Gill, B. Johnson, W. Chen, M. W. Wong, C. Gonzalez, and J. A. Pople. Gaussian 03, Revision C.02. Gaussian, Inc., Wallingford, CT, 2004.

J. L. Fulton, E. J. Bylaska, S. Bogatko, M. Balasubramanian, E. Cauet, G. K. Schenter, and J. H. Weare. Near-quantitative agreement of model-free DFT-MD predictions with XAFS observations of the hydration structure of highly charged transition-metal ions. *Journal of Physical Chemistry Letters*, 3(18):2588–2593, 2012.

D. Gebauer, A. Voelkel, and H. Coelfen. Stable prenucleation calcium carbonate clusters. *Science*, 322(5909):1819–1822, 2008.

S. Gencic, E. C. Duin, and D. A. Grahame. Tight coupling of partial reactions in the acetyl-CoA decarbonylase/synthase (ACDS) multienzyme complex from *Methanosarcina thermophila*: Acetyl C-C bond fragmentation at the A cluster promoted by protein conformational changes. *Journal of Biological Chemistry*, 285 (20):15450–15463.

P. Giannozzi, S. Baroni, N. Bonini, M. Calandra, R. Car, C. Cavazzoni, D. Ceresoli, G. L. Chiarotti, M. Cococcioni, I. Dabo, A. Dal Corso, S. de Gironcoli, S. Fabris, G. Fratesi, R. Gebauer, U. Gerstmann, C. Gougoussis, A. Kokalj, M. Lazzeri, L. Martin-Samos, N. Marzari, F. Mauri, R. Mazzarello, S. Paolini, A. Pasquarello,

L. Paulatto, C. Sbraccia, S. Scandolo, G. Sclauzero, A. P. Seitsonen, A. Smogunov, P. Umari, and R. M. Wentzcovitch. QUANTUM ESPRESSO: a modular and open-source software project for quantum simulations of materials. *Journal of Physics-Condensed Matter*, 21(39), 2009.

G. V. Gibbs, D. F. Cox, K. M. Rosso, N. L. Ross, R. T. Downs, and M. A. Spackman. Theoretical electron density distributions for Fe- and Cu-sulfide earth materials: A connection between bond length, bond critical point properties, local energy densities, and bonded interactions. *Journal of Physical Chemistry B*, 111(8):1923–1931, 2007.

R. Grau-Crespo, N. H. de Leeuw, and C. R. A. Catlow. Cation distribution and magnetic ordering in $FeSbO_4$. *Journal of Materials Chemistry*, 13(12):2848–2850, 2003.

R. Grau-Crespo, N. H. de Leeuw, and C. R. A. Catlow. Distribution of cations in $FeSbO_4$: A computer modeling study. *Chemistry of Materials*, 16(10):1954–1960, 2004.

R. Grau-Crespo, S. Hamad, C. R. A. Catlow, and N. H. de Leeuw. Symmetry-adapted configurational modelling of fractional site occupancy in solids. *Journal of Physics-Condensed Matter*, 19(25):236201–256216, 2007.

R. Grau-Crespo, A. Y. Al-Baitai, I. Saadoune, and N. H. De Leeuw. Vacancy ordering and electronic structure of γ-Fe_2O_3 (maghemite): a theoretical investigation. *Journal of Physics-Condensed Matter*, 22(25):255401–255407, 2010.

S. Grimme. Semiempirical GGA-type density functional constructed with a long-range dispersion correction. *Journal of Computational Chemistry*, 27(15):1787–1799, 2006.

J. C. Grossman, E. Schwegler, E. W. Draeger, F. Gygi, and G. Galli. Towards an

assessment of the accuracy of density functional theory for first principles simulations of water. *Journal of Chemical Physics*, 120(1):300–311, 2004.

E. Guardia and J. A. Padro. Molecular dynamics simulation of ferrous and ferric ions in water. *Chemical Physics*, 144(3):353–362, 1990.

S. Haider, R. Grau-Crespo, A. J. Devey, and N. H. de Leeuw. Cation distribution and mixing thermodynamics in Fe/Ni thiospinels. *Geochimica et Cosmochimica Acta*, 88:275–282, 2012.

W. Han and M. Y. Gao. Investigations on iron sulfide nanosheets prepared via a single-source precursor approach. *Crystal Growth & Design*, 8(3):1023–1030, 2008.

Z. B. He, Y. Shu-Hong, X. Y. Zhou, X. G. Li, and J. F. Qu. Magnetic-field-induced phase-selective synthesis of ferrosulfide microrods by a hydrothermal process: Microstructure control and magnetic properties. *Advanced Functional Materials*, 16 (8):1105–1111, 2006.

H. Hellmann. Einfhrung in die quantenchemie. *Leipzig: Franz Deuticke*, page 285, 1937.

G. Henkelman and H. Jonsson. A dimer method for finding saddle points on high dimensional potential surfaces using only first derivatives. *Journal of Chemical Physics*, 111(15):7010–7022, 1999.

T. S. Hofer, H. T. Tran, C. F. Schwenk, and B. M. Rode. Characterization of dynamics and reactivities of solvated ions by ab initio simulations. *Journal of Computational Chemistry*, 25(2):211–217, 2004.

V. Hoffmann. Greigite (Fe_3S_4) - Magnetic properties and first domain observations. *Physics of the Earth and Planetary Interiors*, 70(3-4):288–301, 1992.

J. T. Hoggins and H. Steinfink. Empirical bonding relationships in metal-iron-sulfide compounds. *Inorganic Chemistry*, 15(7):1682–1685, 1976.

P. Hohenberg and W. Kohn. Inhomogeneous electron gas. *Physical Review B*, 136 (3B):B864, 1964.

C. Huber and G. Wachtershauser. Activated acetic acid by carbon fixation on (Fe,Ni)S under primordial conditions. *Science*, 276(5310):245–247, 1997.

O. Hübner and J. Sauer. Structure and thermochemistry of $Fe_2S_2^{-/0/+}$ gas phase clusters and their fragments. B3LYP calculations. *Physical Chemistry Chemical Physics*, 4(21):5234–5243, 2002.

W. Y. Hui, C. Tenailleau, A. Pring, and J. Brugger. Experimental study of the transformation of pentlandite/pyrrhotite to violarite. *Regolith 2004: proceedings of the CRC LEME Regional Regolith Symposia*, pages 146–150, 2004.

F. Hulliger. Crystal chemistry of the chalcogenides and pnictides of the transition elements. *Structure and Bonding*, 4:83–229, 1968.

H. W. Jannasch and C. O. Wirsen. Chemo-synthetic primary production at east pacific sea-floor spreading centers. *Bioscience*, 29(10):592–598, 1979.

F. Jensen. *Introduction to Computational Chemistry*. Wiley, Second edition, 2006.

W. H. Jørgensen, H. Toftlund, and T. E. Warner. Hydrothermal precipitation of artificial violarite. *Hydrometallurgy*, 115:98–103, 2012.

A. Klamt. Conductor-like screening model for real solvents : A new approach to the quantitative calculation of solvation phenomena. *Journal of Physical Chemistry*, 99(7):2224–2235, 1995.

A. Klamt and G. Schuurmann. COSMO : A new approach to dielectric screening in solvents with explicit expressions for the screening energy and its gradient. *Journal of the Chemical Society-Perkin Transactions 2*, (5):799–805, 1993.

W. Kohn and L. J. Sham. Self-consistent equations including exchange and correlation effects. *Physical Review*, 140(4A):1133, 1965.

G. Kresse and J. Furthmuller. Efficient iterative schemes for *ab initio* total-energy calculations using a plane-wave basis set. *Physical Review B*, 54(16):11169–11186, 1996.

G. Kresse and J. Hafner. *Ab initio* molecular dynamics for liquid metals. *Physical Review B*, 47(1):558–561, 1993.

G. Kresse and J. Hafner. *Ab initio* molecular dynamics simulation of the liquid-metalamorphous-semiconductor transition in germanium. *Physical Review B*, 49 (20):14251–14269, 1994.

G. Kresse and D. Joubert. From ultrasoft pseudopotentials to the projector augmented-wave method. *Physical Review B*, 59(3):1758–1775, 1999.

D. P. Landau and K. Binder. *A Guide to Monte-Carlo Simulations in Statistical Physics*. Cambridge University Press, Third edition, 2009.

M. Y. Lavrentiev, J. A. Purton, and N. L. Allan. Ordering in spinels - a Monte Carlo study. *American Mineralogist*, 88(10):1522–1531, 2003.

A. R. Leach. *Molecular Modelling: Principles and Applications*. Pearson Education, Second edition, 2001.

C. Lee, W. Yang, and R. G. Parr. Development of the colle-salvetti correlation energy formula into a functional of the electron density. *Physical Review B*, 37(2):785–789, 1988.

A. R. Lennie, S. A. T. Redfern, P. F. Schofield, and D. J. Vaughan. Synthesis and Rietveld crystal structure refinement of mackinawite, tetragonal FeS. *Mineralogical Magazine*, 59(397):677–683, 1995.

A. R. Lennie, S. A. T. Redfern, P. E. Champness, C. P. Stoddart, P. F. Schofield, and D. J. Vaughan. Transformation of mackinawite to greigite: An in situ X-ray powder diffraction and transmission electron microscope study. *American Mineralogist*, 82 (3-4):302–309, 1997.

I. Letard, P. Sainctavit, N. Menguy, J. P. Valet, A. Isambert, M. Dekkers, and A. Gloter. Mineralogy of greigite Fe_3S_4. *Physica Scripta*, T115:489–491, 2005.

M. I. Leybourne, U. Schwarz-Schampera, C. E. J. de Ronde, E. T. Baker, K. Faure, S. L. Walker, D. A. Butterfield, J. A. Resing, J. E. Lupton, M. D. Hannington, H. L. Gibson, G. J. Massoth, R. W. Embley, Jr. Chadwick, W. W., M. R. Clark, C. Timm, I. J. Graham, and I. C. Wright. Submarine magmatic-hydrothermal systems at the monowai volcanic center, kermadec arc. *Economic Geology*, 107(8):1669–1694, 2012.

P. A. Lindahl. Acetyl-coenzyme A synthase: the case for a Ni_p^0-based mechanism of catalysis. *Journal of Biological Inorganic Chemistry*, 9(5):516–524, 2004.

W. Lindgren and W. M. Davy. Nickel ores from Key West Mine, Nevada. *Economic Geology*, 19:309–319, 1924.

G. W. Luther and D. T. Rickard. Metal sulfide cluster complexes and their biogeochemical importance in the environment. *Journal of Nanoparticle Research*, 7 (4-5):389–407, 2005.

G. W. Luther, S. M. Theberge, D. T. Rickard, and A. Oldroyd. Determination of metal (bi)sulfide stability constants of Mn^{2+}, Fe^{2+}, Co^{2+}, Ni^{2+}, Cu^{2+}, and Zn^{2+} by voltammetric methods - Response. *Environmental Science & Technology*, 30 (12):3640–3641, 1996.

G. W. Luther, T. F. Rozan, M. Taillefert, D. B. Nuzzio, C. Di Meo, T. M. Shank, R. A. Lutz, and S. C. Cary. Chemical speciation drives hydrothermal vent ecology. *Nature*, 410(6830):813–816, 2001.

A. Luzar and D. Chandler. Effect of environment on hydrogen bond dynamics in liquid water. *Physical Review Letters*, 76(6):928–931, 1996.

G. Macleod, C. McKeown, A. J. Hall, and M. J. Russell. Hydrothermal and oceanic pH conditions of possible relevance to the origin of life. *Origins of Life and Evolution of the Biosphere*, 24(1):19–41, 1994.

R. L. Martin, P. J. Hay, and L. R. Pratt. Hydrolysis of ferric ion in water and conformational equilibrium. *Journal of Physical Chemistry A*, 102(20):3565–3573, 1998.

D. Marx and J. Hutter. *Ab Initio Molecular Dynamics: Theory and Implementation*, volume 1 of *NIC Series*. Modern Methods and Algorithms of Quantum Chemistry, 2000.

C. McCammon, J. M. Zhang, R. M. Hazen, and L. W. Finger. High-pressure crystal-chemistry of cubanite, $CuFe_2S_3$. *American Mineralogist*, 77(9-10):937–944, 1992.

N. Metropolis, A. W. Rosenbluth, M. N. Rosenbluth, A. H. Teller, and E. Teller. Equation of state calculations by fast computing machines. *Journal of Chemical Physics*, 21(6):1087–1092, 1953.

C. Michel, F. Goeltl, and P. Sautet. Early stages of water/hydroxyl phase generation at transition metal surfaces - synergetic adsorption and O-H bond dissociation assistance. *Physical Chemistry Chemical Physics*, 14(44):15286–15290, 2012.

S. Miertus, E. Scrocco, and J. Tomasi. Electrostatic interaction of a solute with a continuum - a direct utilization of ab initio molecular potentials for the prevision of solvent effects. *Chemical Physics*, 55(1):117–129, 1981.

K. V. Mikkeslen and K. O. Sylvester-Hvid. Molecular response method for solvated molecules in nonequilibrium solvation. *J. Chem. Phys.*, 100:9116–9126, 1996.

K. C. Misra and M. E. Fleet. Chemical composition and stability of violarite. *Economic Geology*, 69(3):391–403, 1974.

S. T. Moin, T. S. Hofer, A. B. Pribil, B. R. Randolf, and B. M. Rode. A Quantum Mechanical Charge Field Molecular Dynamics study of Fe^{2+} and Fe^{3+} ions in aqueous solutions. *Inorganic Chemistry*, 49(11):5101–5106, 2010.

H. J. Monkhorst and J. D. Pack. Special points for Brillouin-zone integrations. *Physical Review B*, 13(12):5188–5192, 1976.

R. Mulvaney. Iron-ore sinter in the analytical transmission electron-microscope. *Mineralogical Magazine*, 51(359):61–69, 1987.

N. N. Nair, E. Schreiner, R. Pollet, V. Staemmler, and D. Marx. Magnetostructural dynamics with the extended broken symmetry formalism: Antiferromagnetic [2Fe-2S] complexes. *Journal of Chemical Theory and Computation*, 4(8):1174–1188, 2008.

E. H. Nickel, J. R. Ross, and M. R. Thornber. Supergene alteration of pyrrhotite-pentlandite ore at Kambalda, Western Australia. *Economic Geology*, 69(1):93–107, 1974.

H. Ohtaki and T. Radnai. Structure and dynamics of hydrated ions. *Chemical Reviews*, 93(3):1157–1204, 1993.

L. Onsager. Electric moments of molecules in liquids. *Journal of the American Chemical Society*, 58:1486–1493, 1936.

R. Parr and W. Yang. *Density Functional Theory of Atoms and Molecules*. Oxford, 1989.

D. E. Parry. Electrostatic potential in the surface region of an ionic crystal. *Surface Science*, 49(2):433–440, 1975.

J. P. Perdew, J. A. Chevary, S. H. Vosko, K. A. Jackson, M. R. Pederson, D. J. Singh, and C. Fiolhais. Atoms, molecules, solids, and surfaces: Applications of the generalized gradient approximation for exchange and correlation. *Physical Review B*, 46(11):6671–6687, 1992.

J. P. Perdew, K. Burke, and M. Ernzerhof. Generalized gradient approximation made simple. *Physical Review Letters*, 77(18):3865–3868, 1996.

W. E. Pickett. Pseudopotential methods in condensed matter applications. *Computer Physics Reports*, 9(3):115–197, 1989.

H. P. Pinto and S. D. Elliott. Mechanism of the Verwey transition in magnetite: Jahn-teller distortion and charge ordering patterns. *Journal of Physics-Condensed Matter*, 18(46):10427–10436, 2006.

J. R. Pliego and J. M. Riveros. The cluster-continuum model for the calculation of the solvation free energy of ionic species. *Journal of Physical Chemistry A*, 105 (30):7241–7247, 2001.

J. A. Purton, M. Y. Lavrentiev, and N. L. Allan. Monte Carlo simulation of GaN/InN mixtures. *Journal of Materials Chemistry*, 15(7):785–790, 2005.

S. W. Ragsdale. Nickel-based enzyme systems. *Journal of Biological Chemistry*, 284 (28):18571–18575, 2009.

P. Ramdohr. *The Ore Minerals and Their Intergrowths*. Pergamon Press, Second edition, 1980.

L. Rao, H. Ke, G. Fu, X. Xu, and Y. Yan. Performance of several density functional theory methods on describing hydrogen-bond interactions. *Journal of Chemical Theory and Computation*, 5(1):86–96, 2009.

S. Richardson and D. J. Vaughan. Surface alteration of pentlandite and spectroscopic evidence for secondary violarite formation. *Mineralogical Magazine*, 53(370): 213–222, 1989.

D. Rickard. Kinetics of FeS precipitation: Part 1. Competing reaction-mechanisms. *Geochimica et Cosmochimica Acta*, 59(21):4367–4379, 1995.

D. Rickard and G. W. Luther. Chemistry of iron sulfides. *Chemical Reviews*, 107(2): 514–562, 2007.

B. M. Rode, C. F. Schwenk, and A. Tongraar. Structure and dynamics of hydrated ions - new insights through quantum mechanical simulations. *Journal of Molecular Liquids*, 110(1-3):105–122, 2004.

B. M. Rode, C. F. Schwenk, T. S. Hofer, and B. R. Randolf. Coordination and ligand exchange dynamics of solvated metal ions. *Coordination Chemistry Reviews*, 249 (24):2993–3006, 2005.

A. Rohrbach, J. Hafner, and G. Kresse. Electronic correlation effects in transition-metal sulfides. *Journal of Physics-Condensed Matter*, 15(6):979–996, 2003.

B. Roux and T. Simonson. Implicit solvent models. *Biophysical Chemistry*, 78(1-2): 1–20, 1999.

S. E. Ruiz-Hernandez, R. Grau-Crespo, A. R. Ruiz-Salvador, and N. H. De Leeuw. Thermochemistry of strontium incorporation in aragonite from atomistic simulations. *Geochimica et Cosmochimica Acta*, 74(4):1320–1328, 2010.

M. J. Russell and N. T. Arndt. Geodynamic and metabolic cycles in the Hadean. *Biogeosciences*, 2(1):97–111, 2005.

M. J. Russell and A. J. Hall. The emergence of life from iron monosulphide bubbles at a submarine hydrothermal redox and ph front. *Journal of the Geological Society*, 154:377–402, 1997.

M. J. Russell and W. Martin. The rocky roots of the acetyl-coa pathway. *Trends in Biochemical Sciences*, 29(7):358–363, 2004.

M. A. A. Schoonen, Y. Xu, and J. Bebie. Energetics and kinetics of the prebiotic synthesis of simple organic acids and amino acids with the FeS-H_2S/FeS_2 redox couple as reductant. *Origins of Life and Evolution of the Biosphere*, 29(1):5–32, 1999.

U. Schwertmann. Solubility and dissolution of iron oxides. *Plant and Soil*, 130(1-2): 1–25, 1991.

David M. Sherman. Complexation of Cu^+ in hydrothermal NaCl brines: Ab initio molecular dynamics and energetics. *Geochimica et Cosmochimica Acta*, 71(3): 714–722, 2007.

M. Shoji, K. Koizumi, Y. Kitagawa, S. Yamanaka, T. Kawakami, M. Okumura, and K. Yamaguchi. Theory of chemical bonds in metalloenzymes II: Hybrid-DFT studies in iron-sulfur clusters. *International Journal of Quantum Chemistry*, 105(6): 628–644, 2005.

M. N. Short and E. V. Shannon. Violarite and other rare nickel sulphides. *American Mineralogist*, 15(1):1–22, 1930.

P. H. L. Sit and N. Marzari. Static and dynamical properties of heavy water at ambient conditions from first-principles molecular dynamics. *Journal of Chemical Physics*, 122(20):204510–204518, 2005.

B. J. Skinner, F. S. Grimaldi, and R. C. Erd. Greigite, the thiospinel iron; a new mineral. *American Mineralogist*, 49(5-6):543, 1964.

J. C. Slater. Atomic shielding constants. *Physical Review*, 36(1):0057–0064, 1930.

A. K. Soper, F. Bruni, and M. A. Ricci. Site-site pair correlation functions of water from 25 to 400°C: Revised analysis of new and old diffraction data. *Journal of Chemical Physics*, 106(1):247–254, 1997.

M. R. Spender, J. M. D. Coey, and A. H. Morrish. Magnetic properties and Mössbauer spectra of synthetic samples of Fe_3S_4. *Canadian Journal of Physics*, 50(19):2313, 1972.

E. V. Stefanovich and T. N. Truong. Optimized atomic radii for quantum dielectric continuum solvation models. *Chemical Physics Letters*, 244(1-2):65–74, 1995.

K. O. Stetter and G. Gaag. Reduction of molecular sulfur by methanogenic bacteria. *Nature*, 305(5932):309–311, 1983.

L. Stixrude, E. Wasserman, and R. E. Cohen. Composition and temperature of earth's inner core. *Journal of Geophysical Research-Solid Earth*, 102(B11):24729–24739, 1997.

V. Svetlitchnyi, H. Dobbek, W. Meyer-Klaucke, T. Meins, B. Thiele, P. Romer, R. Huber, and O. Meyer. A functional Ni-Ni-[4Fe-4S] cluster in the monomeric acetyl-CoA synthase from *Carboxydothermus hydrogenoformans*. *Proceedings of the National Academy of Sciences of the United States of America*, 101(2):446–451, 2004.

K. Takai, T. Komatsu, F. Inagaki, and K. Horikoshi. Distribution of archaea in a black smoker chimney structure. *Applied and Environmental Microbiology*, 67(8): 3618–3629, 2001.

P. W. Tasker. Stability of ionic-crystal surfaces. *Journal of Physics C-Solid State Physics*, 12(22):4977–4984, 1979.

L. A. Taylor and K. L. Williams. Smythite, $(Fe,Ni)_9S_{11}$ - A redefinition. *American Mineralogist*, 57(11-1):1571–1577, 1972.

C. Tenailleau, B. Etschmann, R. M. Ibberson, and A. Pring. A neutron powder diffraction study of Fe and Ni distributions in synthetic pentlandite and violarite using Ni-60 isotope. *American Mineralogist*, 91(8-9):1442–1447, 2006.

R. K. Thauer. Nickel to the fore. *Science*, 293(5533):1264–1265, 2001.

S. M. Theberge and G. W. Luther III. Determination of the electrochemical properties of a soluble aqueous FeS species present in sulfidic solution. *Aquatic Geochemistry*, 3:191–211, 1997.

L. H. Thomas. The effect of the orbital velocity of the electrons in heavy atoms on their stopping of α-particles. *Proceedings of the Cambridge Philosophical Society*, 23:713–716, 1927.

J. Tomasi and M. Persico. Molecular interactions in solution: An overview of methods based on continuous distributions of the solvent. *Chemical Reviews*, 94(7): 2027–2094, 1994.

J. Tomasi, B. Mennucci, and R. Cammi. Quantum mechanical continuum solvation models. *Chemical Reviews*, 105(8):2999–3093, 2005.

R. A. Torres, T. Lovell, L. Noodleman, and D. A. Case. Density functional and reduction potential calculations of Fe_4S_4 clusters. *Journal of the American Chemical Society*, 125(7):1923–1936, 2003.

M. G. Townsend, J. R. Gosselin, J. L. Horwood, L. G. Ripley, and R. J. Tremblay. Violarite, a metallic natural spinel. *Physica Status Solidi (A), Applied Research*, 40 (1):K25–K29, 1977.

T. N. Truong and E. V. Stefanovich. A new method for incorporating solvent effect into the classical, ab initio molecular orbital and density functional theory frameworks for arbitrary shape cavity. *Chemical Physics Letters*, 240(4):253–260, 1995.

M. Uda. On synthesis of greigite. *American Mineralogist*, 50(9):1487, 1965.

H. H. Uhlig. The solubilities of gases and surface tension. *Journal of Physical Chemistry*, 41(9):1215–1225, 1937.

R. E. Vandenberghe, E. Degrave, P. M. A. Debakker, M. Krs, and J. J. Hus. Mössbauer effect study of natural greigite. *Hyperfine Interactions*, 68(1-4):319–322, 1991.

D. Vanderbilt. Soft self-consistent pseudopotentials in a generalized eigenvalue formalism. *Physical Review B*, 41(11):7892–7895, 1990.

D. J. Vaughan and J. R. Craig. *Mineral Chemistry of Metal Sulfides*. Cambridge University Press, 1978.

D. J. Vaughan and J. R. Craig. The crystal-chemistry of iron-nickel thiospinels. *American Mineralogist*, 70(9-10):1036–1043, 1985.

D. J. Vaughan and M. S. Ridout. Mössbauer studies of some sulphide minerals. *Journal of Inorganic & Nuclear Chemistry*, 33(3):741, 1971.

D. J. Vaughan and J. A. Tossell. Electronic structure of thiospinel minerals: results from MO calculations. *American Mineralogist*, 66(11-1):1250–1253, 1981.

D. J. Vaughan, R. G. Burns, and V. M. Burns. Geochemistry and bonding of thiospinel minerals. *Geochimica et Cosmochimica Acta*, 35(4):365, 1971.

L. Verlet. Computer "experiments" on classical fluids. I. Thermodynamical properties of Lennard-Jones molecules. *Physical Review*, 159(1):98–103, 1967.

E. J. W. Verwey and P. W. Haayman. Electronic conductivity and transition point of magnetite ("Fe_3O_4"). *Physica*, 8:979–987, 1941.

A. Volbeda and J. C. Fontecilla-Camps. The active site and catalytic mechanism of NiFe hydrogenases. *Dalton Transactions*, (21):4030–4038, 2003.

A. Volbeda and J. C. Fontecilla-Camps. Structure-function relationships of nickel-iron sites in hydrogenase and a comparison with the active sites of other nickel-iron enzymes. *Coordination Chemistry Reviews*, 249(15-16):1609–1619, 2005.

A. Volbeda, M. H. Charon, C. Piras, E. C. Hatchikian, M. Frey, and J. C. Fontecilla-camps. Crystal structure of the nickel-iron hydrogenase from *Desulfovibrio Gigas*. *Nature*, 373(6515):580–587, 1995.

K. L. Vondamm. Seafloor hydrothermal activity: Black smoker chemistry and chimneys. *Annual Review of Earth and Planetary Sciences*, 18:173–204, 1990.

S. H. Vosko, L. Wilk, and M. Nusair. Accurate spin-dependent electron liquid correlation energies for local spin-density calculations: A critical analysis. *Canadian Journal of Physics*, 58(8):1200–1211, 1980.

G. Wächtershäuser. Before enzymes and templates: Theory of surface metabolism. *Microbiological Reviews*, 52(4):452–484, 1988.

G. Wächtershäuser. Evolution of the first metabolic cycles. *Proceedings of the National Academy of Sciences of the United States of America*, 87(1):200–204, 1990.

G. Wächtershäuser. Groundworks for an evolutionary biochemistry: The iron sulfur world. *Progress in Biophysics & Molecular Biology*, 58(2):85–201, 1992.

G. Wächtershäuser. Life as we don't know it. *Science*, 289(5483):1307–1308, 2000.

P. Waldner. Thermodynamic modelling of violarite. *Journal of Chemical Thermodynamics*, 41(2):171–174, 2009.

J. Wang, S.-H. Cao, W. Wu, and G.-m. Zhao. The Curie temperature and exchange energy between two sublattices in half-metallic greigite Fe_3S_4. *Physica Scripta*, 83(4):045702, 2011.

T. E. Warner, N. M. Rice, and N. Taylor. Thermodynamic stability of pentlandite and violarite and new E_H-pH diagrams for the iron-nickel sulphur aqueous system. *Hydrometallurgy*, 41(2-3):107–118, 1996.

G. W. Watson, E. T. Kelsey, N. H. deLeeuw, D. J. Harris, and S. C. Parker. Atomistic simulation of dislocations, surfaces and interfaces in MgO. *Journal of the Chemical Society-Faraday Transactions*, 92(3):433–438, 1996.

D. L. Williams, R. P. Vonherze, J. G. Sclater, and R. N. Anderson. The Galapagos Spreading Center: Lithospheric cooling and hydrothermal circulation. *Geophysical Journal of the Royal Astronomical Society*, 38(3):587, 1974.

M. Wolthers, L. Charlet, P. R. Van der Linde, D. Rickard, and C. H. Van der Weijden. Surface chemistry of disordered mackinawite (FeS). *Geochimica et Cosmochimica Acta*, 69(14):3469–3481, 2005.

G. Wulff. On the question of speed of growth and dissolution of crystal surfaces. *Zeitschrift Fur Krystallographie Und Mineralogie*, 34(5/6):449–530, 1901.

F. Xia, J. Zhou, J. Brugger, Y. Ngothai, B. O'Neill, G. Chen, and A. Pring. Novel route to synthesize complex metal sulfides: Hydrothermal coupled dissolution-reprecipitation replacement reactions. *Chemistry of Materials*, 20(8):2809–2817, 2008.

S. Yamaguchi and T. Katsurai. *Kolloid Z.*, 170:147, 1960.

Y. Zhao and D. G. Truhlar. Design of density functionals that are broadly accurate for thermochemistry, thermochemical kinetics, and nonbonded interactions. *Journal of Physical Chemistry A*, 109(25):5656–5667, 2005.

Y. Zhao, B. J. Lynch, and D. G. Truhlar. Doubly hybrid meta DFT: New multi-coefficient correlation and density functional methods for thermochemistry and

thermochemical kinetics. *Journal of Physical Chemistry A*, 108(21):4786–4791, 2004.